# EFFECTIVE RESERVOIR MANAGEMENT FOR CARBON UTILIZATION AND STORAGE APPLICATIONS

A Dissertation

by

FEYISAYO OMONIYI OLALOTITI-LAWAL

Submitted to the Office of Graduate and Professional Studies of
Texas A&M University
in partial fulfillment of the requirements for the degree of

DOCTOR OF PHILOSOPHY

| | |
|---|---|
| Chair of Committee, | Akhil Datta-Gupta |
| Committee Members, | Michael J. King |
| | Eduardo Gildin |
| | Bani Mallick |
| Head of Department, | Duane McVay |

May 2018

Major Subject: Petroleum Engineering

# ABSTRACT

It is believed that the observed rapid rise in global temperatures is caused by high atmospheric concentration of CO2, due to emissions from fossil fuel combustion. While global efforts are currently in place to mitigate the effect, it is expected that hydrocarbons will remain the main source of energy supply for the planet in the foreseeable future. Harmonizing these seemingly conflicting objectives has given rise to the concept of Carbon Capture Utilization and Storage (CCUS).

A prominent form of CCUS involves the capture and injection of anthropogenic CO2 for Enhanced Oil Recovery (EOR). During CO2 EOR, substantial amount of injected CO2 is retained and permanently stored in the subsurface. However, due to inherent geological and thermodynamic complexities in subsurface environments, most CCUS projects are plagued with poor sweep efficiencies. For successful CCUS implementation, advanced reservoir management strategies which appropriately capture relevant physics are therefore required. In this regard, effective techniques in three fundamental areas of reservoir management including forward modeling, inverse modeling and field development optimization methods are presented herein. In each area, we demonstrate the validity and utility of our methodologies for CCUS applications with field examples.

First, a comprehensive streamline-based simulation of CO2 in saline aquifers is proposed. Here, the unique strength of streamlines at resolving sub-grid resolution which enables a high-resolution representation of CO2 transport during injection is exploited. Relevant physics such as compressibility and formation dry-out effects which were ignored in previously proposed streamline models are accounted for. The methodology is illustrated with a series of synthetic models and applied to the Johansen field in North Sea. All streamline-based models are benchmarked with commercial compositional simulation response with good agreement.

Second, a Multiresolution Grid Connectivity-based Transform (M-GCT) for effective subsurface model calibration is proposed. M-GCT allows the representation and update of grid property fields with improved spatial resolutions. This enables improved characterization of the subsurface, especially for CCUS systems in which CO2 transport is highly sensitive to contrasts in hydraulic conductivity. The approach is illustrated with a synthetic and a field scale problem. To demonstrate its utility, the proposed method is applied to a field actively supporting a post-combustion CCUS project.

Finally, a streamline-based rate optimization of intelligent wells used in CCUS projects is proposed. Based on a previously developed method, a combination of the incremental oil recovery, CO2 storage efficiency and CO2 utilization factor are optimized through an optimal rate schedules of the installed ICVs. The approach is particularly efficient since required objective function gradients and hessians are computed analytically from streamline-derived sensitivities obtained from a single simulation run. This significantly reduces the computational expense required to obtain solutions at level of optimality comparable to existing methods. The approach is illustrated with a synthetic case and applied to the Norne field to demonstrate the robustness of the approach.

# DEDICATION

To my parents and siblings for their unrelenting moral support.

# ACKNOWLEDGEMENTS

I would like to acknowledge and appreciate the support and mentorship of my supervisor, Dr. Akhil Datta-Gupta through the entire period of my graduate studies. I am grateful to Dr. Michael King for his valuable suggestions during many of our discussions. I appreciate the constructive criticisms and advise from Dr. Bani Mallick and Dr. Eduardo Gildin. These have all proven useful for the completion of this work.

All forms of financial support received from the sponsors of the MCERI Joint Industry Project towards the completion of this work are gratefully acknowledged. I appreciate to Schlumberger, Chevron and QRI LLC for offering me ‘summer school’ opportunities. Lastly, special thanks to the Petra Nova Joint Venture who have graciously provided field data that has enabled the proof of validity of the reservoir characterization workflows reported here.

I wish to gratefully acknowledge Jason Demshar and the IT crew for their assistance with the Wildcat high-performance computing cluster which was utilized for many of the field-scale simulations reported in this work. Finally, to my MCERI Aggie colleagues both in school and in the industry, thank you for making this journey a memorable one.

# CONTRIBUTORS AND FUNDING SOURCES

## Contributors

This work was supervised by a dissertation committee consisting of Professor Akhil Datta-Gupta (chair), Michael King and Eduardo Gildin of the Petroleum Engineering Department and Professor Bani Mallick of the Department of Statistics.

All work for the dissertation was completed by the student, under the advisement of Akhil Datta-Gupta of the Department of Petroleum Engineering.

## Funding Sources

This work was made possible by financial support from member companies of the Model Calibration and Efficient Reservoir Imaging (MCERI) consortium.

# TABLE OF CONTENTS

Page

# LIST OF FIGURES

# LIST OF TABLES

Page

# CHAPTER I

# INTRODUCTION

## 1.1 Background

Climate data acquired in the last few decades has clearly revealed a rising trend in global temperatures. It is generally believed that the gradual warming of the planet can be attributed to increasing concentrations of Carbon dioxide (CO2) in the atmosphere caused by human activities (IPCC, 2013). It is also claimed that increase in anthropogenic CO2 emissions from combustion of fossil fuels and industrial activities in recent decades show close correlation with observed temperature increase (IPCC, 2014). A concerted effort to mitigate this effect has brought about one of the United Nations' Sustainable Development Goals (SDGs) of reducing global concentrations of CO2 in the atmosphere (Griggs et al., 2013).

An acclaimed technology for achieving this is the Carbon Capture and Storage (CCS). This involves all activities from the extraction of CO2 from industrial flue gas all the way to permanent sequestration. Deep geologic formations and deep oceans have been identified as possible CO2 storage sites. However, due to the high cost of the current CCS technology, Carbon Capture, Utilization and Storage (CCUS) technologies tend to be more economically attractive. CCUS refers to a combination of techniques that involves the capture of CO2 as in CCS followed by a recycling or an economic utilization of the captured CO2, in the process of which it is ultimately sequestered.

One category of possible locations for permanent storage of CO2 is in deep geologic systems. This will be the focus of this dissertation. Identified geological media include depleted hydrocarbon reservoirs, unmineable coal seams, deep saline formations and active oil reservoirs, in which CO2 is utilized for enhanced oil recovery (USDOE, 2015), as shown in **Fig. 1.1**. The latter is referred to as a form of CCUS, in which it is expected that the economic benefits from CO2 enhanced oil recovery (EOR) process can be utilized for offsetting the high cost of CCS. In the rest of this section we provide more background on both geological CCS and CO2 EOR technologies and how they are reconciled for the purpose of achieving the atmospheric CO2 concentration reduction goal.

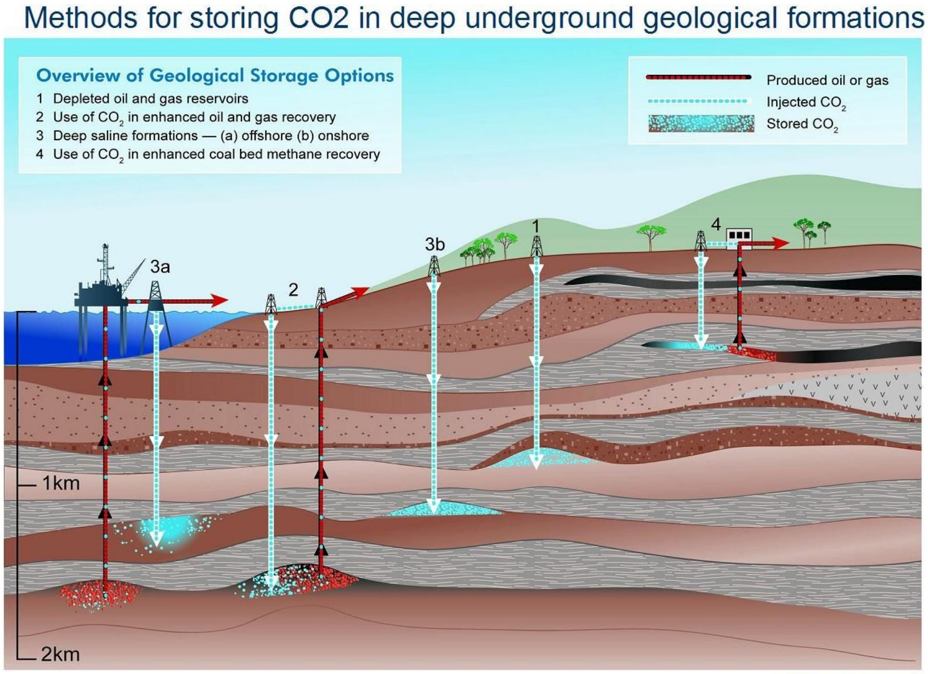

Figure 1.1: CCUS applications in underground geological formations, reprinted from IPCC (2005)

### *1.1.1 Geological Carbon Capture and Storage*

The fundamental components of CCS involve the capture, transportation and eventual injection and storage of CO2 in the subsurface. Geological CCS has been recognized as the most versatile and vital climate mitigation technology that could be applied for providing a stabilization wedge in atmospheric concentrations of CO2 by the end of the century (Global CCS Institute, 2017; Pacala and Socolow, 2004). Up to 220 million tons (Mt) of CO2 has been injected into the subsurface till date with a total of 17 large scale CCS facilities are currently operational globally. An additional annual 37 Mt storage capacity is expected to be added with additional four facilities coming online in 2018 (Global CCS Institute, 2017).

The CCS technology is however not without its technical challenges. Beside operational challenges related facilities installation, a good understanding of the behavior of the injected CO2 in the subsurface can determine the level of success of any CCS project. The hallmark of success in a CCS project is for the injected CO2 trapped and eventually permanently sequestered in the geologic media with. Achieving this objective often begins with the assessment of storage capacity of candidate formations based of relevant mechanisms involving considers pressures, volumetric and trapping mechanisms which are pivotal to CO2 containment in the subsurface (Heidug, 2013).

Injected CO2 undergoes four main mechanisms of trapping in the subsurface, which are structural, residual, solubility and mineral trapping mechanisms (IPCC, 2005). As shown in **Fig. 1.2**, the trapping mechanisms vary in contributions and storage security with time. Structural or stratigraphic trapping mechanism involves geological features such as sealing faults and stratigraphic seals that contain CO2 plume migration under the force of gravity and diffusion in the subsurface. This is known to offer the least storage security and tends to decline in trapping contribution with time as other trapping mechanisms take over. Residual trapping, which depends on relative permeability and capillary hysteresis effects is next in terms of initial trapping contribution. A more secure trapping mechanism is the solubility trapping in which CO2 dissolves in formation fluids, such as brine at in situ pressures and temperature. Finally, in mineral trapping, dissolved CO2, after an extended period of time reacts with in situ chemical molecules to become permanently sequestered.

Beyond CO2 trapping mechanisms, relevant geological features also play significant roles in the success of a CCS project. The subsurface is inherently heterogeneous, especially in terms of hydraulic conductivity, and this is critical in determining flow path of CO2. Calibration of geologic models by integrating observed data acquired from operation projects often provide improved knowledge of the important trends and scale of heterogeneity. Understanding the subsurface is key to effective management of geologic CCS projects.

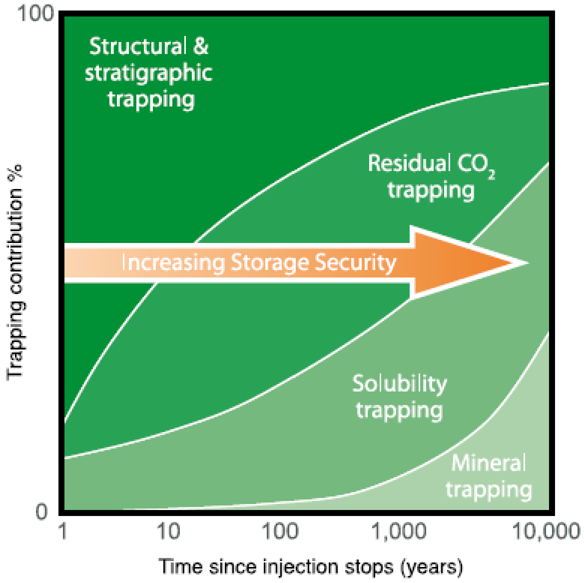

Figure 1.2: CO2 trapping mechanisms, reprinted from IPCC (2005)

### *1.1.2 Carbon Dioxide Enhanced Oil Recovery (CO2 EOR)*

A proven and mature technology for enhancing the productive life of oil fields internationally is CO2 EOR. The technology has been shown to be economically viable oil recovery method for over four decades. The first commercial demonstration of the technology was with the SCROC project in the early 1970s in West Texas (Crameik and Plassey, 1972). About 400 billion barrels of stranded oil resource currently lie in mature fields across the US, of which 52 billion barrels is technically recoverable by CO2 EOR (DiPietro, 2013). More than 100 CO2 EOR projects are operational in the US, with more than 50% located in the Permian basin (Melzer, 2012). With the possibility of an increase in the number of operational facilities, it is predicted that domestic production form the

CO2 EOR technology is project to rise up to 700,000 barrels per day by 2040 as shown in **Fig. 1.3**.

The possibilities of increase in domestic production from mature, and sometimes abandoned fields comes from the effect of CO2 on residual oil in the subsurface. Injected CO2 contacts and dissolves in the in situ residual oil, causing it to swell, thereby causing a reduction in oil viscosity. The eventual increase in oil mobility makes oil recoverable from residual conditions. CO2 can either be first contact or multiple contact miscible in oil, however CO2 ceases to readily soluble in oil below a critical pressure known as the Minimum Miscibility Pressure (MMP) – a fundamental property of the hydrocarbon composition of the oil.

The CO2 EOR technology has been applied in multiple forms. This includes continuous CO2 injection which is often applied to highly water-wet formations, CO2 Water-Alternating Gas (WAG), CO2 huff-and-puff, and so on. Due to its superior advantage of better mitigation of mobility contrasts, there has been as wide spread application of the CO2 WAG method. CO2 WAG, as the name implies, involves solely injecting gas and water in alternating fashion. The interval of alternation and the slug sizes of each fluid depends on the CO2 EOR design, based on reservoir geology and/or operational constraints (Ettehadtavakkol et al., 2014).

Sufficient contact between injected CO2 and resident oil phase is crucial for improved oil recovery efficiency which marks the success of any CO2 EOR project. This underscores the need for high volumetric sweep efficiency during CO2 injection. However this usually becomes a challenge due to (1) density differences which results in unfavorable gravity override, and (2) Mobility contrasts which causes undesired viscous fingering of CO2. Both phenomena in combination cause poor conformance and eventual reduction in CO2 sweep efficiency. These effects are further aggravated by sharp heterogeneity contrasts in hydraulic conductivities. Addressing these challenges often hinges on the application of modern reservoir management techniques.

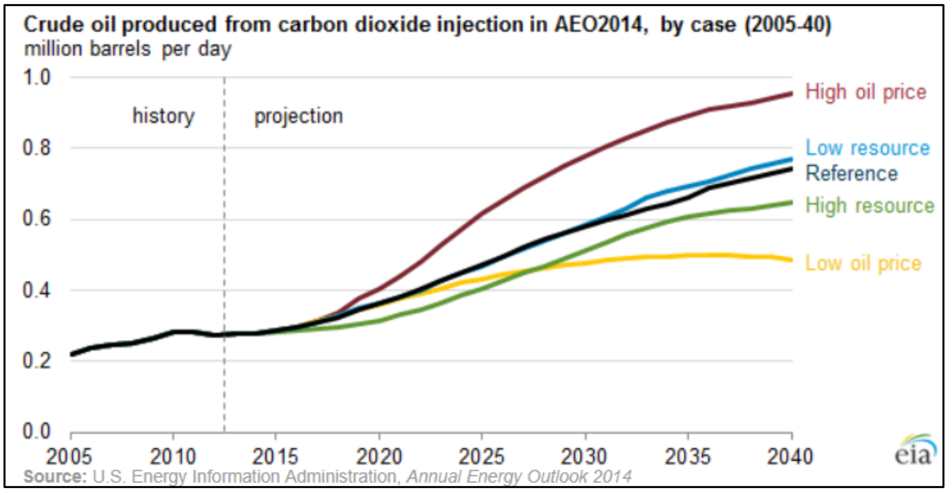

Figure 1.3: Trends in US CO2 EOR production, reprinted from EIA (2014)

### *1.1.3 Reconciling CCS with CO2 EOR for CCUS*

The basic idea of CCUS, pertaining to geological storage of CO2 is a symbiosis relationship between two seemingly conflicting objectives. Although the idea has been in existence for decades, more conscious efforts are recently being made to design CCUS projects to reduce atmospheric carbon footprint while meeting world’s immediate demand for hydrocarbons. Years of data from CO2 EOR production has revealed that certain amount of injected CO2 is always retained in the formation. This signifies some CO2 storage associated with CO2 EOR as it has always been implemented.

One major difference between a regular CO2 EOR process and a planned CCUS process is the CO2 source. Sourcing CO2 from natural underground deposits, as is often done, is believed not to contribute to the climate mitigation efforts. Modern CCUS designs targeted at carbon footprint reduction source CO2 from industrial flue gas and power plants. For instance, the newly commissioned Petra Nova plant captures and transports up to 1.4MtCO2 per annum from the W. A. Parish power plant to the West Ranch field where it utilized in a CO2 EOR scheme. Petra Nova is considered the world's largest post-combustion CO2 capture plant. A distribution of global CO2 injection projects according to their respective CO2 sources and construction time is provided in **Fig. 1.4**. According to the figure, although the CCUS technology began as early as the first large-scale implementation of the CO2 EOR technology, dedicated CCS projects only started in the mid 90's with Sleipner in the North Sea.

Since the mid 90's global CO2 storage capacity, as well as cumulative CO2 injection for CCUS has seen an exponential increase with time, as shown in **Fig. 1.5**. On this path, the number of CCUS projects across the world is expected to double within a decade (Global CCS Institute, 2017). Again, challenges abound with effective management of CCUS processes due to the critical attributes of CO2 that derogate from desired performance. Many CO2 injection projects suffer from conformance problems due to viscous fingering of CO2 and gravity override which are further aggravated by inherent geological heterogeneities. It is believed that application of modern reservoir management techniques in advanced flood design can help increase sweep efficiencies (Wallace et al., 2013), which is believed to be beneficial to both CO2 storage and recovery of residual oil.

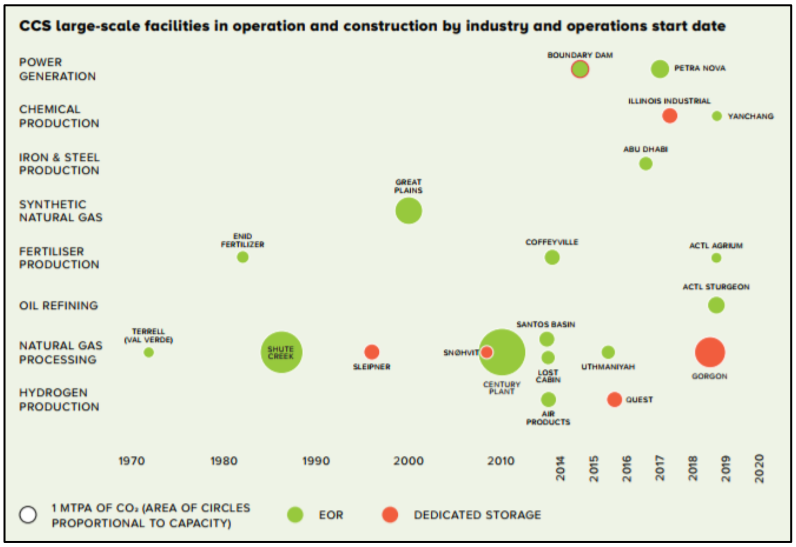

Figure 1.4: Large-scale CCS/CCUS facilities across the globe, reprinted from Global CCS Institute (2017)

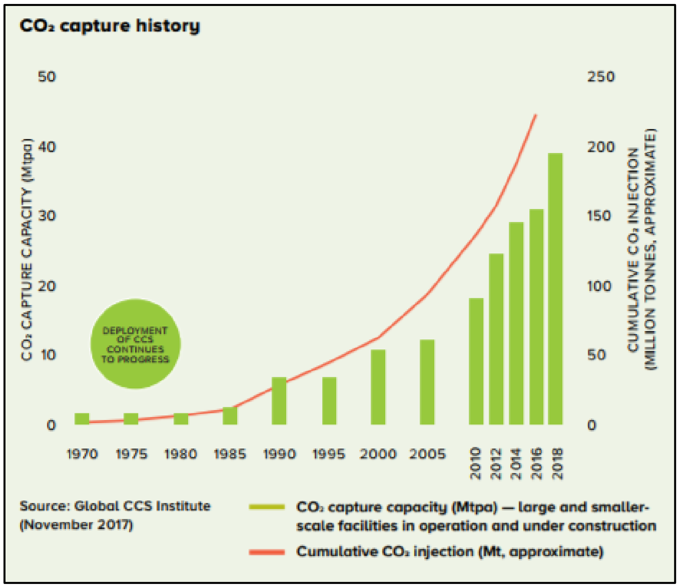

Figure 1.5: Global CO2 storage capacity and cumulative CO2 injection as functions of time, reprinted from Global CCS Institute (2017)

## 1.2 Reservoir Management

The key to addressing the pressing challenges associated with successful implementation of CCUS projects is effective reservoir management techniques (Wallace et al., 2013). The fundamental components of reservoir management procedure include the forward modeling, inverse modeling and optimization workflows. Here we provide a general brief overview of these concepts as it concerns CCUS.

### *1.2.1 Forward Modeling*

This involves all endeavor at representing relevant physics or phenomena that describe certain processes of interest. Certain simplifying assumptions are made, in any framework of choice in creating subsurface flow models which are eventually applied to evaluate different subsurface flow scenarios. Due to advances in technology, modern subsurface flow models are typically constructed based on mathematical and/or computational frameworks. In these frameworks, there is often a trade-off between speed and fidelity. Analytical or semi-analytical models, which are developed based on more simplifying assumptions, require less computational effort but are limited in application. High-fidelity solutions on the other hand, which involve numerical schemes for solving coupled flow equations, are based on less simplifying assumptions which makes them more applicable to realistic situations, however at extra computational cost.

Analytical/semi-analytical models, which are derived from first principles, capture relevant driving mechanisms to facilitate quick diagnostics of the problem. Such models have been applied in reservoir management efforts for decades (Arps, 1945; Havlena and

Odeh, 1963). Recent methods attempt to account for subsurface heterogeneities by reducing reservoir models into graphs of wells and connections (Albertoni and Lake, 2003; Ibrahima et al., 2017; Sayarpour et al., 2009). Analytical streamline-based solutions have also been proposed, using the front tracking technique to compute the propagation of saturation and mole fractions in heterogeneous and dual continuum media (Di Donato and Blunt, 2004; Lie and Juanes, 2005; Nilsen and Lie, 2009; Seto and Orr, 2009; Seto et al., 2007). Specifically for gas injection systems, analytical models accounting for gravity segregation have been proposed (Nordbotten et al., 2005; Rossen et al., 2010). Although elegant and computationally efficient, analytical models struggle in reality at capturing high-resolution effects which are sometimes more impactful to the overall performance of the subsurface flow scenario of interest.

Numerical models are often resorted to when analytical models fail. Numerical models are designed to solve coupled partial differential equations that describe subsurface flow through varying spatial and temporal discretization schemes (Jenny et al., 2003; Karimi-Fard et al., 2003; Møyner and Lie, 2014; Sweby, 1984; Yanosik and McCracken, 1979). All numerical scheme however attempt to solve governing equations that describe fluid flow in the subsurface, starting from the differential material balance for any component $i$ given as (Aziz and Settari, 1979a):

$$\sum_{\pi=o,w,g}\left(\frac{\partial}{\partial t}(\phi y_{i\pi}\rho_{\pi}s_{\pi})-\nabla\bullet y_{i\pi}\hat{\rho}_{\pi}\mathbf{u}_{\pi}+y_{i\pi}q_{i\pi}\right)=0 \qquad (1.1)$$

Where $y_{i\pi}$ represents then mole fraction of component $i$ in phase $\pi$ (which can be oil, water or gas), while $q_{i\pi}$ represents the source (well injection rate) or sink (well withdrawal rate) terms of component $i$ in phase $\pi$ is defined control volume. $\hat{\rho}_\pi$, $s_\pi$ and $\mathbf{u}_\pi$ repectively denote the molar density, saturation and velocity field of phase $\pi$. Finally, $\phi$ denotes formation porosity. The phase velocity can be obtained by Darcy's Law:

$$\mathbf{u}_\pi = -\lambda_\pi \mathbf{k} \bullet \left( \nabla p_\pi - \rho_\pi g \nabla Z \right) \tag{1.2}$$

In which $\lambda_\pi$ and $\rho_\pi$ respectively refer to the mobility (ratio of relative permeability to viscosity) and mass density of phase $\pi$. The phase pressure, which is a difference between the system pressure and capillary pressure $(p_c)$ is denoted as $p_\pi$. Model permeability tensor is represented as $\mathbf{k}$, while gravity and vertical elevation are denoted as $g$ and $Z$ respectively. The governing equation in **Eq. 1.1** can be solved using different schemes including fully implicit, sequential implicit or Implicit Pressure Explicit Saturation (IMPES) form of schemes. The latter two schemes require a decoupling of **Eq. 1.1** into pressure and transport equations. The streamline-based flow simulation utilizes the IMPES scheme in which the system pressure is solved implicitly to obtain the flux field on which streamline trajectories are based. Transport equation, written as follows, is explicitly solved along the streamlines:

$$\phi \frac{\partial c_i}{\partial t} + \nabla \bullet \mathbf{u}_i = 0 \tag{1.3}$$

where $c_i = \sum_{\pi=o,w,g} y_{i\pi} \hat{\rho}_\pi s_\pi$ and $\mathbf{u}_i = \sum_{\pi=o,w,g} y_{i\pi} \hat{\rho}_\pi \mathbf{u}_\pi$

To solve the transport equation along streamlines, **Eq. 1.3** is transformed from the 3D domain into a set of independent 1D equations. In coordinate transformation, an arbitrary velocity can be described in terms of effective density, $\tilde{\rho}$ and a set of bi-streamfunctions as follows:

$$\tilde{\rho}\mathbf{u}_t = \nabla\psi \times \nabla\chi \tag{1.4}$$

The bi-streamfunctions determine the trajectory of a streamline (King and Dunayevsky, 1989) while the effective density serves to conserve mass along the streamline. The formalism leads to the introduction of a new spatial coordinate known as the time-of-flight $\tau$, which is defined as the transit time of a neutral tracer in a particular flux field (Datta-Gupta and King, 2007). Streamline time-of-flight is expressed as:

$$\mathbf{u}_t \bullet \nabla\tau = \phi \tag{1.5}$$

Where $\mathbf{u}_t$ denotes total velocity. By combining **Eqs. 1.4** and **1.5** the transport equation is expressed in a 1D form along the streamlines as follows (Osako and Datta-Gupta, 2007):

$$\frac{\partial c_i}{\partial t} + \frac{\partial}{\partial \tau} f_i^{sl} = -\frac{f_i^{sl}}{\phi} \nabla \bullet \mathbf{u}_t \tag{1.6}$$

It is informative to re-arrange **Eq. 1.2** as follows (Aziz and Settari, 1979a):

$$\mathbf{u}_\pi = \frac{\lambda_\pi}{\lambda_t}\mathbf{u}_t + \frac{\lambda_\pi}{\lambda_t}\mathbf{k} \bullet \sum_{\alpha \neq \pi} \left[\lambda_\alpha \left(\nabla p_c + \Delta\rho g \nabla Z\right)\right]; \text{ where } \lambda_t = \sum_\pi \lambda_\pi \tag{1.7}$$

In this form, the convective component (in the first term) of the phase velocity is decoupled form the gravity and capillary components (in the second term). In an operator-splitting framework, streamline-based methods account for the convective term in a predictor step and the transverse fluxes (including capillarity and gravity terms) in the corrector step (King et al., 2005). In this case $f_i^{sl} = \lambda_\pi / \lambda_t$ while the correction, solve on the underlying grid, accounts for the second term in **Eq. 1.7**. For gravity and/capillary dominated systems, like in CCUS processes, the orthogonal projection approach is recommended. Here convective fluxes as well as significant proportion of the gravity and capillary forces are accounted for in the predictor step, leaving room for relatively small corrections on the underlying simulation grid (Tanaka et al., 2014).

Streamline-based solution to multiphase flow in the subsurface finds a neutral ground between high-fidelity numerical flow simulations and simple analytical models. The high level of numerical resolution achievable in high contrast systems compared to other modeling approaches makes streamline-based method applicable for CCUS problems.

### *1.2.2 Inverse Modeling*

This includes all workflows and procedures for integrating observed data into reservoir models, in the process of which relevant model parameters are estimated. Subsurface model calibration, also referred to as history matching, remains a challenging step in most reservoir management workflows due to the high computational requirements. Since all model calibration workflows rely on some forward model, it is expected that, with the same objective function reduction algorithm, the efficiency model calibration step scale linearly with the forward model evaluation speed. The other challenge with model inversion problems is the inherent non-uniqueness of solutions. This often requires the generation of an ensemble of plausible solutions that all agree with the observation data.

The ultimate goal of a model calibration exercise is to update current state of knowledge of the subsurface model by calibrating reservoir parameters so that the resulting reservoir model reproduces the observed data. Observed data include dynamic field observations such as multiphase production, well test, 4D seismic data and so on. The selection of model parameters to be included in the calibration process requires prior sensitivity studies to determine the ‘heavy hitters’. Model properties that are spatially correlated such as grid petrophysical properties (permeability or porosity) are often re-parameterized. This takes advantage of the spatial correlation of these properties in their spectral representation using few uncorrelated parameters. Using a set of real numbers $\mathbf{v} \in \mathbb{R}^M$, a grid property vector $\mathbf{m} \in \mathbb{R}^N$, for $M \le N$, can be represented in real (on the left) and spectral (on the right) domains as:

$$\mathbf{m} = \Phi \mathbf{v} \Leftrightarrow \mathbf{v} = \Phi^T \mathbf{m} \tag{1.8}$$

Where $\Phi$ denotes a collection of orthonormal eigenvectors of a characteristic parameterization matrix.

Many forms of parameterization schemes have been proposed (Bhark, 2011; Bhark et al., 2011b; Honorio et al., 2015; Jafarpour and McLaughlin, 2008; Jafarpour and McLaughlin, 2009; Khaninezhad et al., 2012; Sarma et al., 2008b). One popular schemes are the Principal Component Analysis (PCA) in which $\Phi$ is obtained from the singular value decomposition (SVD) of the property covariance matrix. The other is the Discrete Cosine Transforms (Strang, 1999) which has been generalized to the Grid Connectivity-based Transforms (GCT) to handle all forms of reservoir model grid geometries (Bhark et al., 2011a). Here unlike in PCA, $\Phi$ is obtained from SVD of the grid Laplacian. In other words, GCT precludes the extra difficult task of constructing a covariance matrix for the grid properties. In addition, GCT becomes more applicable in non-Gaussian grid properties, characterized by high permeability streaks, for example.

Solving a model calibration problem involves an optimization problem which seeks the best set of parameters that minimizes a defined residual between model response and observed data. Objective functions are typically constructed depending of the solution paradigm. In a sensitivity-based formalism (Kulkarni et al., 2000; Vasco et al., 1999), the objective function is constructed as follows:

$$J(\mathbf{m}) = \left\|\delta\mathbf{d}_{obs} - \mathbf{S}\delta\mathbf{m}\right\|_2^2 + \eta_1\left\|\delta\mathbf{m}\right\|_2^2 + \eta_2\left\|\Gamma\delta\mathbf{m}\right\|_2^2 \tag{1.9}$$

Where $\delta\mathbf{d}_{obs} = \mathbf{d}_{obs} - g(\mathbf{m})$ ( $g(\mathbf{m})$ is the forward model response based on $\mathbf{m}$ ), $\delta\mathbf{m}$ is the parameter deviation from the prior model and the parameter sensitivities is expressed as:

$$\mathbf{S} = [S_{ij}] = \frac{\partial g_i(\mathbf{m})}{\partial m_j} \tag{1.10}$$

The second and third terms of the objective functions are respectively the regularization and roughness penalties. $\Gamma$ is a spatial smoothness operator while $\eta_1$ and $\eta_2$ are specific weights which respectively determine the strengths of the prior model and roughness conditions. Guidelines in the selection of these weights are provided in (Parker, 1994). The optimal solution that minimizes the objective function can be obtained by solving the least-squares problem (Paige and Saunders, 1982):

$$\begin{pmatrix} \mathbf{S} \\ \eta_1 \mathbf{I} \\ \eta_2 \Gamma \end{pmatrix} \delta \mathbf{m} = \begin{pmatrix} \delta \mathbf{d}_{obs} \\ 0 \\ 0 \end{pmatrix} \tag{1.11}$$

This model inversion formalism has been utilized extensively in the updating of high-resolution geologic models using streamline-based methods (Cheng et al., 2005; Cheng et al., 2007; Cheng et al., 2004; He et al., 2002). This is because of the quasi-linear feature of the construction. More importantly, in the streamline-based inversion approach, sensitivities are computed analytically with a single numerical simulation run making it applicable to large multi-million geologic models. Finally, grid property updates are robust and avoid overfitting, thereby preserving the geological realism of the subsurface model.

In the Bayesian paradigm, the posterior distribution of the model parameters $P(\mathbf{m} \,|\, \mathbf{d}_{obs})$ relates to the product of the likelihood $P(\mathbf{d}_{obs} \,|\, \mathbf{m})$ and the prior distribution $P(\mathbf{m})$ of the parameter distribution with some proportionality constant (Oliver et al., 2008):

$$P(\mathbf{m} \,|\, \mathbf{d}_{obs}) \propto P(\mathbf{d}_{obs} \,|\, \mathbf{m}).P(\mathbf{m}) = \exp\left(-J(\mathbf{m})\right) \tag{1.12}$$

The posterior distribution can be expressed as a multivariate Gaussian function with the argument $J(\mathbf{m})$ given as:

$$J(\mathbf{m}) = \frac{1}{2}\left[\left(\mathbf{d}_{obs} - g(\mathbf{m})\right)^T \mathbf{C}_D^{-1}\left(\mathbf{d}_{obs} - g(\mathbf{m})\right) + \left(\mathbf{m}_{prior} - \mathbf{m}\right)^T \mathbf{C}_{\mathbf{m}}^{-1}\left(\mathbf{m}_{prior} - \mathbf{m}\right)\right] \tag{1.13}$$

Where $\mathbf{C}_D$ and $\mathbf{C}_{\mathbf{m}}$ are respectively the data covariance matrix and the parameter covariance matrix. This formalism allows a generation of multiple solutions with finite non-zero values of the posterior distribution function $P(\mathbf{m} | \mathbf{d}_{obs})$. Eq. 13 can be solved for optimal values for $\mathbf{m}$ using the Gauss-Newton or Levenberg-Marquardt algorithms in a gradient-based approach (Nocedal and Wright, 2006a). Sampling algorithms however exist and have been applied to obtaining multiple plausible solutions from the posterior distribution function (Ma et al., 2008; Maucec et al., 2007; Olalotiti-Lawal, 2013; Xie et al., 2011). Ensemble-based methods have also shown promise in achieving probabilistic model calibration of subsurface models (Aanonsen et al., 2009; Emerick and Reynolds, 2013; Evensen, 2003; Watanabe and Datta-Gupta, 2012).

Finally, a recently introduced approach to history matching, which is applicable to potentially conflicting objectives utilizes the multiobjective optimization concept (Das and Dennis, 1997; Deb et al., 2002). In this approach, diverse multiple trade-off solutions are generated as the final result (Hajizadeh et al., 2011; Olalotiti-Lawal and Datta-Gupta, 2015; Park et al., 2015). Typically, calibrated model(s) are utilized for field performance forecasts and/or field development optimization purposes.

### *1.2.3 Field Development Optimization*

A final fundamental component of reservoir management is field development optimization. Usually, this step is contingent on the availability of credible models that are conditioned to available data. Most field development optimization problems consider optimal placement of wells, well drilling schedule and production and injection rate schedules under pre-specified operational or economic constraints. While design variables depend on the type of optimization in question, decision variables have historically been cumulative hydrocarbon production or net present value (NPV) of the asset. The NPV-based optimization concept introduces economic parameters such as discount factors in the optimization procedure. Like in the solution to subsurface model calibration problems, solution approaches to field development optimization problems take different approaches.

Well placement optimization problems seek the optimal locations of multiple wells or completions in the reservoir to maximize defined decision variables. This results in a class of optimization problems referred to as Mixed Integer Non-Linear Problems (MINLP). Solutions to this problem have been proposed based on gradient or sensitivity-based methods (Møyner et al., 2015; Sarma and Chen, 2008; Zandvliet et al., 2008) as well as population-based or evolutionary algorithms (Badru and Kabir, 2003; Bouzarkouna et al., 2012; Emerick et al., 2009; Guyaguler and Horne, 2001; Isebor et al., 2014; Onwunalu and Durlofsky, 2011). A typical challenge with population-based or evolutionary algorithm methods is the large amount of computations required to obtain desired solutions. Gradient-based methods, on the other hand are frequently get trapped in local extrema. Approaches which utilize fast model evaluation proxies, which are therefore amenable to exhaustive search of the parameter space have been proposed to address the issue (Møyner et al., 2015; Taware et al., 2012).

In many cases, especially in mature fields, field development plans that require no additional drilling campaigns are more economically attractive. Ensemble-based methods have been applied using a closed-loop reservoir management approach is obtaining optimal rate schedules (Chen et al., 2009; Jansen et al., 2009; Sarma et al., 2005; Wang et al., 2009). Davidson and Beckner (2003) opposed an integrated production optimization technique which utilizes the Sequential Quadratic Programming (SQP) algorithm (Nocedal and Wright, 2006b) in obtaining optimal rate schedules. An effective rate optimization approach was proposed that also utilizes SQP but however effectively computes required gradients and hessian from analytical streamline-derived sensitivites (Alhuthali et al., 2006; Alhuthali et al., 2010). Gradient-free methods which also exploit the strength of streamlines have also been proposed (Park and Datta-Gupta, 2013; Tanaka et al., 2017; Thiele and Batycky, 2006). Specifically for CCUS applications, both streamline-based and ensemble-based methods have been proposed (Chen and Reynolds, 2015; Sharma et al., 2016).

## 1.3 Contributions and Thesis Outline

This work provides contribution in each of the components of reservoir management discussed in the previous section as it pertains to CCUS applications. Details on these are reported in the following chapters. The robustness of the proposed methodologies and algorithms are demonstrated with real field applications. Below are the highlights of each chapter:

(1) A comprehensive streamline-based simulation of CO2 sequestration saline aquifers is presented in the second chapter. This work is motivated by the need to effectively handle subsurface heterogeneity effects dating the injection of supercritical CO2 in saline aquifers. The algorithm, implemented in an existing streamline simulation code (Tanaka, 2014), is validated with commercial compositional simulator. The effects of

compressibility and formation dry-out effects, which were ignored in previous streamline-based methods, are implemented and validated. Finally, an application to the North Sea's Johansen formation is presented.

(2) A multi-resolution grid connectivity-based parameterization scheme for efficient subsurface model calibration was proposed. A motivation for this work comes from a common scenario in mature fields characterized by localized distribution of data. It is common in geological CCUS applications that active wells are localized in specific regions in the reservoir domain. Constructing GCT basis functions that takes into consideration such special cases results in improved reservoir characterization. This concept is illustrated with a synthetic model and a field-scale Brugge benchmark case (Peters et al., 2010). An application to the West Ranch field – which supports the Petra Nova CCUS project – is presented.

(3) A field development optimization based streamline-based optimization of intelligent wells is proposed. The workflow, based on previously proposed methodology (Alhuthali et al., 2010), optimizes the incremental oil recovery efficiency, CO2 utilization factor as well as the CO2 storage efficiency. Finally, the value and utility of the proposed methodology is demonstrated with an application to the North Sea's Norne field.

# CHAPTER II

# COMPREHENSIVE STREAMLINE SIMULATION OF CARBON DIOXIDE STORAGE IN SALINE AQUIFERS

Subsurface sequestration of CO2 has received high level of attention from the global scientific community in response to climate change due to higher concentrations of CO2 in the atmosphere. Mathematical models have thus been developed to aid the understanding of multiphase flow of CO2 and trapping mechanisms during subsurface sequestration. Solutions to these models have ranged from analytical, semi-analytical and numerical methods, each having its merits and demerits in terms of underlying physics, computational speed and accuracy.

We present a streamline-based method for modeling CO2 transport in saline aquifers which relies on the sub-grid resolution of streamlines in capturing small and large-scale heterogeneity effects during CO2 injection. Our approach is based on an iterative IMPES scheme and accounts for the physical processes characteristic of CO2 injection in saline aquifers. These include compressibility, gravity, capillarity, mutual solubility, precipitation and formation dry-out effects. We present series of examples encompassing different levels of geologic and geometrical complexity to illustrate the accuracy and computational efficiency of the approach.

Our streamline simulation method provides an extension of previous streamline-based models through rigorous treatment of transverse fluxes arising from compressibility, gravity and capillary effects.

## 2.1 Introduction

Climate change is a topical environmental issue which has been linked to the rise in global average temperatures because of increase in greenhouse gases (GHG) such as carbon dioxide (CO2) and methane in the atmosphere in the last century. The past few decades have witnessed a global concerted effort at reversing the trend by reducing the concentration of these gases, particularly CO2 in the atmosphere. A promising strategy is Carbon Capture and Storage (CCS) which involves capturing CO2 from industrial sources such as coal fired power plants, transportation of the CO2 and injection in subsurface geologic formations for permanent storage. Candidate formations include depleted hydrocarbon reservoirs, unmineable coal deposits and saline aquifers, which is known to show the highest potential for large scale subsurface storage (USDOE, 2015).

Like most subsurface flow processes, injection of CO2 in saline aquifers poses certain risks (Arts et al., 2008) arising from the dearth of data and subsurface uncertainty. Important risks include leakage of CO2 through old wells or non-sealing faults into underground water or the earth surface. These pose significant hazard to public health and the environment (Apps et al., 2010; Siirila et al., 2012). Proper site selection therefore requires understanding of CO2 plume migration in the short and long terms in the subsurface and understanding flow and trapping mechanisms of CO2 under varying thermodynamic conditions, geologic settings and structures at different time scales. The dominant trapping mechanisms of CO2 including structural, residual, capillary, solubility and mineral have been well documented in the literature (Bachu et al., 2007; Bachu et al., 1994; Ennis-King and Paterson, 2003; IPCC, 2005; MacMinn et al., 2010; Saadatpoor et al., 2010).

Analytical and numerical predictive models incorporating relevant trapping mechanisms at varying fidelity levels have been developed for reliable evaluation of saline aquifer candidates for CO2 sequestration. Analytical models are valuable in identifying key parameters and/or dimensionless groups for better understanding important physics underlying the process and provides an efficient tool for screening of aquifer candidates for CO2 storage (Mathias et al., 2009b). Nordbotten et al. (2005) presented an analytical solution for CO2 plume evolution during injection in saline aquifers with homogenous media properties and uniform initial conditions. Vilarrasa et al. (2013) proposed a semi-analytical solution as an improvement over the existing analytical solutions by accounting for non-uniform CO2 flux from the well across the aquifer cross-section. Mathias et al. (2009a) and Mijic et al. (2014) included the Forcheimer model in their analytical model to study the influence of non-Darcy flow and gas compressibility on well injectivity. While analytical solutions provide significant benefits in terms of lower computational cost, capturing important details such as small and large scale permeability heterogeneities remains a challenge.

Numerical models allow for more realistic description of subsurface flow of CO2 in saline aquifers. Numerical simulation codes such as TOUGH2_ECO2N (Pruess, 2005), CMG-GEM-GHG (Nghiem et al., 2004) and E300-CO2STORE (Schlumberger, 2014) implicitly/semi-implicitly solve conservation equations using typically finite difference/volume schemes. Therefore, more detailed description of non-linear relationships between model parameters with system state variables such as pressure, temperature and fluid saturations becomes possible. This allows higher fidelity representation of relevant subsurface flow phenomena such as residual and capillary trapping mechanisms (Saadatpoor et al., 2010; Spiteri et al., 2005), gravity induced convection and formation dry out effects (Giorgis et al., 2007; Pruess and Müller, 2009). Capturing these detailed physics, which sometimes require local grid refinements, however often come with much higher computational cost compared with analytical models.

The streamline simulation has been applied (Obi and Blunt, 2006; Qi et al., 2009) to improve upon the computational efficiency of classical finite volume models. Besides faster solutions, streamline models offer visual and physically intuitive representation of the flow, making the results easy to analyze. With streamline-based methods, 3D transport problems are reduced to a set of independent 1D problems oriented along the direction of the total flux (Datta-Gupta and King, 2007). Streamline-based approaches also reduce numerical artifacts and better represent heterogeneities through sub-grid resolutions, making it suitable for large scale and geologically realistic systems, as illustrated in **Fig. 2.1**. Obi and Blunt (2006) proposed the streamline simulation approach for CO2 sequestration modeling in highly heterogeneous formations, using Henry's Law for CO2 solubility in brine and first order reaction model. Qi et al. (2009) later proposed an improved streamline simulation method to account for mutual solubility of CO2 in aqueous phase and water in CO2-rich phase. Both models showed good agreement with analytical solution in 1D domain, but were not benchmarked with standard simulation models for field scale applications. More importantly, these models have assumed incompressible flow which has been shown to potentially result in erroneous prediction of plume geometry (Vilarrasa et al., 2010).

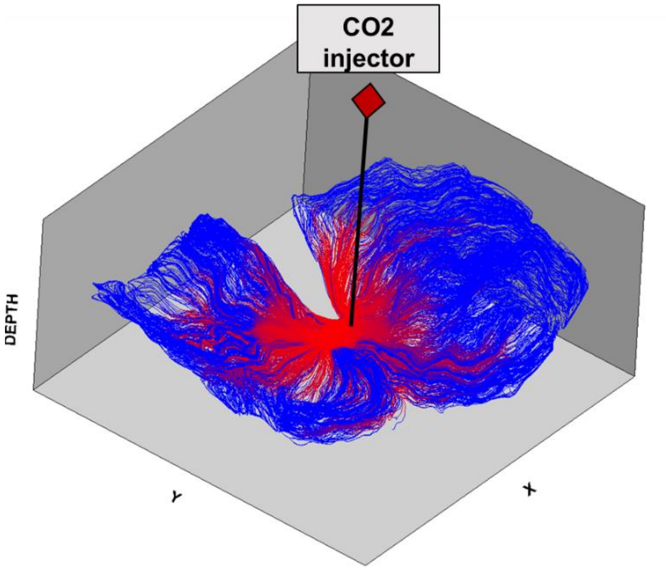

Figure 2.1: Generated streamline distribution for a CO2 injection in a faulted reservoir. Streamlines are contoured by phase saturations (gas phase in red). This figure illustrates the capability of streamlines in capturing sub-grid resolution

We present a comprehensive streamline-based method for simulation of CO2 sequestration in saline aquifers. Our approach accounts for fluid compressibility effects by incorporating an effective density term that allows for fluid expansion and compression along (Cheng et al., 2006; Osako and Datta-Gupta, 2007). Transverse fluxes such as gravity, capillarity and diffusion are accounted for using the orthogonal projection approach (Tanaka et al., 2014). Mutual solubility effects and precipitation effects are included to model well infectivity alteration during CO2 injection. Comparison between streamline simulation results and commercial compositional finite difference simulation results show good agreement in terms of pressure, phase saturations, component concentrations, while offering improved computational benefit. The outline of this chapter is as follows: First we present the simulation model formulation including material balance and fluid property models. Next we provide the steps involved in our streamline simulation approach. We then we present 1D and 2D cross-section illustrative examples. Finally, we demonstrate the robustness of our approach using application to the Johansen field (Eigestad et al., 2009), a candidate for large scale storage of anthropogenic CO2.

## 2.2 Simulation Model

We begin with the governing equations and transformation into streamline Time-of-Flight (TOF) coordinates (Datta-Gupta and King, 2007). Next we discuss the fluid property and phase equilibria model applied in our approach, followed by modeling of salt precipitation and formation dry-out. The dry-out phenomenon in CO2 sequestration in saline aquifers has been well studied and shown to affect injection and formation pressure (Giorgis et al., 2007; Peysson et al., 2014), which in turn affects CO2 distribution between CO2-rich and aqueous phases – a critical component in the computation of CO2 storage efficiencies. Finally, we discuss the reaction model and formation porosity and permeability variations as a result of salt precipitation and reaction.

### *2.2.1 Governing Transport Equations*

Reactive transport in CO2-brine system during CO2 sequestration in saline aquifers is here modeled using a three-component, two-phase system. Water $(w)$ and CO2 $(c)$ components are distributed in the aqueous $(aq)$ and CO2-rich phases $(g)$ while the salt $(s)$ component is only present in the aqueous phase. Phase and component transport can be modeled by solving a system of coupled nonlinear equations as follows:

$$\frac{\partial}{\partial t}\left(\phi\rho_g s_g\right)+\nabla\bullet\left(\rho_g\mathbf{u}_g\right)=\left(\Delta m_{w,g}-\Delta m_{c,aq}\right) \tag{2.1}$$

$$\frac{\partial}{\partial t}\left(\phi\rho_{aq} s_{aq}\right)+\nabla\bullet\left(\rho_{aq}\mathbf{u}_{aq}\right)=\left(\Delta m_{c,aq}-\Delta m_{w,g}\right)-\Delta m_{Rxn} \tag{2.2}$$

$$\frac{\partial}{\partial t}\left(\phi y_w\rho_g s_g\right)+\nabla\bullet\left(y_w\rho_g\mathbf{u}_g\right)=\Delta m_{w,g} \tag{2.3}$$

$$\frac{\partial}{\partial t}\left(\phi x_c\rho_{aq} s_{aq}\right)+\nabla\bullet\left(x_c\rho_{aq}\mathbf{u}_{aq}\right)=\Delta m_{c,aq}-\Delta m_{Rxn,c} \tag{2.4}$$

$$\frac{\partial}{\partial t}\left(\phi x_s\rho_{aq} s_{aq}\right)+\nabla\bullet\left(x_s\rho_{aq}\mathbf{u}_{aq}\right)=-\Delta m_{Rxn,s} \tag{2.5}$$

**Eqs. 2.1** and **2.2** describe phase transport for the CO2-rich $(g)$ and aqueous $(aq)$ phases respectively. **Eqs. 2.3–2.5** on the other hand, describe component transport for water dissolved in the CO2-rich phase as well as CO2 and salt dissolved in the aqueous phase respectively. The phase saturations, velocities and densities are denoted by $s_\pi, \mathbf{u}_\pi$ and $\rho_\pi$; $\pi \in \{g, aq\}$ respectively whereas the mass fraction of component $\upsilon$ in aqueous and CO2-rich phases are respectively denoted by $x_\nu$ and $y_\nu$; $\nu \in \{c, s, w\}$. Incremental masses of CO2 dissolved in the aqueous phase and of pure water dissolved in the CO2-rich phase per unit time are respectively denoted as $\Delta m_{c,aq}$ and $\Delta m_{w,g}$. Overall additional mass change in the aqueous phase per unit time as a result of chemical reactions is denoted by $\Delta m_{Rxn}$ while $\Delta m_{Rxn,c}$ and $\Delta m_{Rxn,s}$ denote the additional mass change in aqueous CO2 and salt due to chemical reactions.

Imposing the condition that phase saturations must sum up to unity everywhere at all times, **Eqs. 2.1** and **2.2** can be combined to obtain the overall mass balance equation as:

$$\sum_{\pi=g,aq} B_\pi \left[ s_\pi \frac{\partial}{\partial t}\left(\frac{\phi}{B_\pi}\right) + \nabla \bullet \left(\frac{\mathbf{u}_\pi}{B_\pi}\right)\right] = \left(\frac{1}{\rho_{aq}-\rho_g}\right)\left(\Delta m_{c,aq} - \Delta m_{w,g}\right) + \frac{m_{Rxn}}{\rho_{aq}} \tag{2.6}$$

Here the phase formation volume factor, denoted by $B_\pi$ is the ratio of phase densities at surface conditions to phase densities at subsurface conditions. Phase velocities can be expressed as function of grid pressure gradient following the usual Darcy's law:

$$\mathbf{u}_\pi = -\lambda_\pi \mathbf{k} \bullet \left(\nabla p_\pi - \rho_\pi g \nabla z\right) \tag{2.7}$$

where $\lambda_\pi$ represents the phase mobility, $\mathbf{k}$ the grid permeability tensor and $p_\pi$ the phase pressure which is the difference between system pressure $p$ and gas-water capillary pressure $p_{cgw}$. **Eqs. 2.6** and **2.7** can be solved implicitly to obtain instantaneous spatial distribution of the system pressure $p$, which is also taken as the pressure of the non-wetting phase (CO2-rich phase). Note that for this step, $s_\pi, \Delta m_{w,g}, \Delta m_{c,aq}$ and $m_{Rxn}$ values are obtained from the previous time step. This is the implicit step of the IMPES scheme that is applied in our streamline simulation approach. From the pressure solution, the velocity field can be obtained using **Eq. 2.6**. For the purpose of streamline simulation, the aqueous phase velocity is expressed in terms of total velocity:

$$\mathbf{u}_g = F_g \mathbf{u}_t + \frac{\lambda_{aq}\lambda_g}{\lambda_t}\mathbf{k} \bullet \left(\nabla p_{cg,aq} + \Delta\rho g \nabla z\right) \tag{2.8}$$

where $F_g$ is the fractional flow of the CO2-rich phase calculated by $\lambda_g / \lambda_t$ while the fractional flow of the aqueous phase is simply obtained as $F_{aq} = 1 - F_g$. Phase velocities can be resolved along the direction of the total velocity by orthogonal projection as a means for effectively accommodating gravity and capillary along streamlines, so that **Eq. 2.8** becomes (King et al., 2005; Tanaka et al., 2014):

$$\mathbf{u}_g = F_g \mathbf{u}_t + \frac{\lambda_{aq}\lambda_g}{\lambda_t}\mathbf{k} \bullet \left(\nabla p_{cg,aq} + \Delta\rho g \nabla z\right) = f_g \mathbf{u}_t + \mathbf{u}_{g\perp} \tag{2.9}$$

Where

$$f_g = \frac{\mathbf{u}_t \bullet \mathbf{u}_g}{u_t^2} = F_g + \frac{1}{u_t^2}\frac{\lambda_{aq}\lambda_g}{\lambda_t}\mathbf{u}_t \bullet \mathbf{k} \bullet \left(\nabla p_{cg,aq} + \Delta\rho g \nabla z\right) \tag{2.10}$$

$$\mathbf{u}_{g\perp} = \left(\mathbf{I} - \hat{\mathbf{u}}_t\hat{\mathbf{u}}_t\right) \bullet \mathbf{u}_g = \frac{\lambda_{aq}\lambda_g}{\lambda_t}\left(\mathbf{I} - \hat{\mathbf{u}}_t\hat{\mathbf{u}}_t\right) \bullet \mathbf{k} \bullet \left(\nabla p_{cg,aq} + \Delta\rho g \nabla z\right)$$

The beauty of the orthogonal projection approach is its robustness and ease of implementation with no requirement of anti-diffusive flux computation as demanded by the operator splitting approach (Berenblyum et al., 2003). Furthermore, for most practical applications, significant portion of the gravity and capillary effects are accounted for along the streamlines, leaving transverse fluxes $\mathbf{u}_{aq\perp}$ of relatively smaller magnitudes to be corrected for on the underlying grid. Larger time step sizes are therefore possible, with overarching effect of improved computational efficiency (Tanaka et al., 2014).

### 2.2.2 *Streamline Simulation*

We adopt the generalized representation of a velocity field using a set of bi-streamfunctions and the introduction of the effective density, $\rho$ to account for compressibility effects (Osako and Datta-Gupta, 2007):

$$\rho\mathbf{u}_t = \nabla\psi \times \nabla\chi \tag{2.11}$$

The introduction of the bi-streamfunctions facilitates an efficient 1D flow description along a new spatial coordinate known as the time of flight, $\tau$ .The time of flight is defined as the transit time of a neutral tracer along total velocity $\mathbf{u}_t$, mathematically expressed in the differential form as:

$$\mathbf{u}_t \bullet \nabla\tau = \phi \tag{2.12}$$

This allows a $(\tau, \psi, \chi)$ coordinate system in which $\mathbf{u}_t$ is perpendicular to both $\nabla\psi$ and $\nabla\chi$. Therefore, it can easily be shown that applying the time of flight definition in **Eq. 2.12** to a gradient operator in this coordinate system results in the operator: $\mathbf{u}_t \bullet \nabla = \phi \frac{\partial}{\partial\tau}$ which can be applied to any scalar field in the model domain. Applying this operator to the flux conservation, knowing that $\nabla \bullet \rho\mathbf{u}_t$ must vanish, we obtain the following form for the velocity divergence which is finite for general compressible systems:

$$\nabla \bullet \mathbf{u}_t = -\phi \frac{\partial \ln \rho}{\partial \tau} = -\sigma \tag{2.13}$$

The previously discussed transport equations can then be written in the streamline coordinates, applying the orthogonal projection phase fluxes along the direction of the total velocity and the definition of the velocity divergence. The CO2-rich phase transport equation, for instance, becomes:

$$\frac{\partial}{\partial t}\left(\rho_g s_g\right) + \frac{\partial}{\partial \tau}\left(\rho_g f_g\right) = \sigma \frac{\rho_g f_g}{\phi} \tag{2.14}$$

The second term of the LHS can be rearranged into a form complaint with the 1D solution scheme (Tanaka et al., 2014):

$$\frac{\partial}{\partial \tau}\left(\rho_g f_g\right) = \frac{\partial}{\partial \tau}\left(\rho_g F_g + \frac{\rho_g}{u_t^2} \frac{\lambda_{aq}\lambda_g}{\lambda_t}\left[\left(\hat{\mathbf{u}}_t \bullet \mathbf{k} \bullet \hat{\mathbf{u}}_t\right)\left(\phi \frac{\partial p_{cg,aq}}{\partial \tau}\right) + k_z \phi \Delta \rho g \frac{\partial z}{\partial \tau}\right]\right) \tag{2.15}$$

Where $k_z$ is the z-direction permeability component of the tensor $\mathbf{k}$. Note that compressibility effect turns out to be accounted for along streamlines as an extra sink/source as shown in the right hand side of **Eq. 2.14**. The CO2-rich phase as well as the component transport equations can be treated similarly. Similarly, component transport equations result in the following 1D predictor equations:

$$\frac{\partial}{\partial t}\left(y_v \rho_g s_g\right) + \frac{\partial}{\partial \tau}\left(y_v \rho_g f_g\right) = \sigma \frac{y_v \rho_g f_g}{\phi} \tag{2.16}$$

$$\frac{\partial}{\partial t}\left(x_v \rho_{aq} s_{aq}\right) + \frac{\partial}{\partial \tau}\left(x_v \rho_{aq} f_{aq}\right) = \sigma \frac{x_v \rho_{aq} f_{aq}}{\phi} \tag{2.17}$$

where $v \in \{c, s, w\}$. It is important to point out here that mutual solubility calculations are conducted as phase and saturation fronts are advanced along streamlines. As will be shown later, this is critical to effectively capturing the formation the dry-out phenomena. Phase saturation and component mass fraction profile solutions obtained along the streamlines are mapped on the finite difference grid where transverse fluxes and other physics such as dissolution and reaction are accounted for on the underlying grid using the following corrector forms:

$$\frac{\partial}{\partial t}\left(\phi\rho_g s_g\right) = -\nabla \bullet \left(\rho_g \mathbf{u}_{g\perp}\right) \tag{2.18}$$

$$\frac{\partial}{\partial t}\left(\phi y_v \rho_g s_g\right) = -\nabla \bullet \left(y_v \rho_g \mathbf{u}_{g\perp}\right) \tag{2.19}$$

Similar expressions can be written for the aqueous phase and its components. Note that reaction contribution is accounted for here as well on the underlying grid. It is important to note that for practical injection rates of supercritical CO2 into the aquifer, as we have for most CO2 sequestration applications, dominant fluxes are already handled along the streamlines, leaving minimal transverse fluxes (orthogonal to the total flux direction) to be corrected for on the grid. Also in our formulation, only incremental dissolution of components into the phases are included in the equations. This, together with the reaction term in general, represents a small portion of total adjustments on the phase saturation and concentration distributions during the corrector step of our simulation workflow. Consequently, much smaller computational overhead is incurred during the corrector step on the finite difference grid, compared to the predictor step along streamlines.

### *2.2.3 Multiscale Streamlines*

To mitigate grid resolution effects associated with gravity override in subsurface gas injection modeling, we applied a global grid refinement scheme for the transport equations. Similar to previously multiscale streamline simulation methods (Aarnes et al., 2005; Gautier et al., 1999; Stenerud et al., 2008), we solve for pressure field on a coarse grid and map the flux field to the fine grid for saturation and compositional transport solution. Here, however, the pressure and flux fields are solved on the original native grid and the coarse flux field is downscaled unto the refined grid for streamline tracing, 1D saturation and composition propagation and traverse flux correction steps.

Flux reconstruction on the refined grid followed the Pollock approach using the previously proposed adaptive refinement tracing method (Matringe and Gerritsen, 2004). For a general 3-D grid refinement problem, refined grid fluxes are estimated in two steps. First, the flux values along each of the three directions is obtained independently by linear interpolation. In other words, for a three-level coarse grid refinement along the ***i***-direction, total fluxes at both end faces of the coarse cell are linearly interpolated to estimate total fluxes of two faces (within the coarse cell) which form the ***i***-faces of 3 pillars of refined grid cells. Next, the calculated total flux at each ***i***-face of a pillar of grids is downscaled commensurate with connection areas of individual refined grid cell (as defined by the coarse grid dimensions) to obtain the corresponding ***i***-face fluxes of the refined grid cells. For practical field-scale subsurface models, isoparametric transformations are utilized to account for irregular corner point grid geometries (Datta-Gupta and King, 2007; Jimenez et al., 2010).

In our approach, flow properties used for the refined grids including the flux divergence term, are directly populated from corresponding parent coarse grid values, Also, like the regular Pollock's algorithm, our flux construction remains conservative ( $\nabla \bullet \rho \mathbf{q} = 0$), thereby naturally enhancing mass conservation. Finally, at each well completion grid we compute a local pressure distribution $p$ in the refined grid by solving a local pseudo-steady state differential mass balance equation described by:

$$\nabla \bullet \frac{\mathbf{k}}{\mu} \nabla p = c_t \phi V_G \frac{\partial \overline{p}}{\partial t} + q_{well} \tag{2.20}$$

Where $q_w$ denote the well completion rate at subsurface conditions, while $\phi$, $\mu$, $c_t$ and $V_G$ respectively represent the porosity, fluid viscosity, total compressibility and bulk volume of the parent coarse well grid at the current time step. Note here that the permeability tensor $\mathbf{k}$ is essentially homogeneous and isotropic.

The local pressure distribution is constrained by the average pressure value $\overline{p}$ computed from **Eq. 2.6** on the coarse grid as well as by the coarse cell face fluxes. Also similar to Gautier et al. (1999), the local pressure system construction takes into account fluxes in neighboring coarse cells. The solution of **Eq. 2.20** requires the solution of a single linear system which is only as large as the size of grid refinement. For a three-level vertical grid refinement strategy, **Eq. 2.20** results only in a series of third order linear systems for each open completion. The solution of all these independent linear systems is inconsequential computationally compared to the global pressure solve. Total fluxes in the refined grid are computed based on the calculated pressure field using Darcy equation.

The value of our multiscale streamline methodology is illustrated with a scenario in which fluid is being injected at the center of a 2D heterogeneous infinite domain. In **Fig. 2.2**, we compare the streamlines generated with regular Pollock's algorithm with that generated with our multiscale methodology based on the trajectories and the times of flight along the streamlines. Although equal number of streamlines were traced in both cases, smoother gradation of $\tau$ values can be observed with the multiscale method. With finer $\tau$ discretizations obtained in the multiscale method, we hypothesize a major mitigation of adverse grid resolution effects on achievable streamline sub-grid resolutions during transverse flux corrections (Bratvedt et al., 1996).

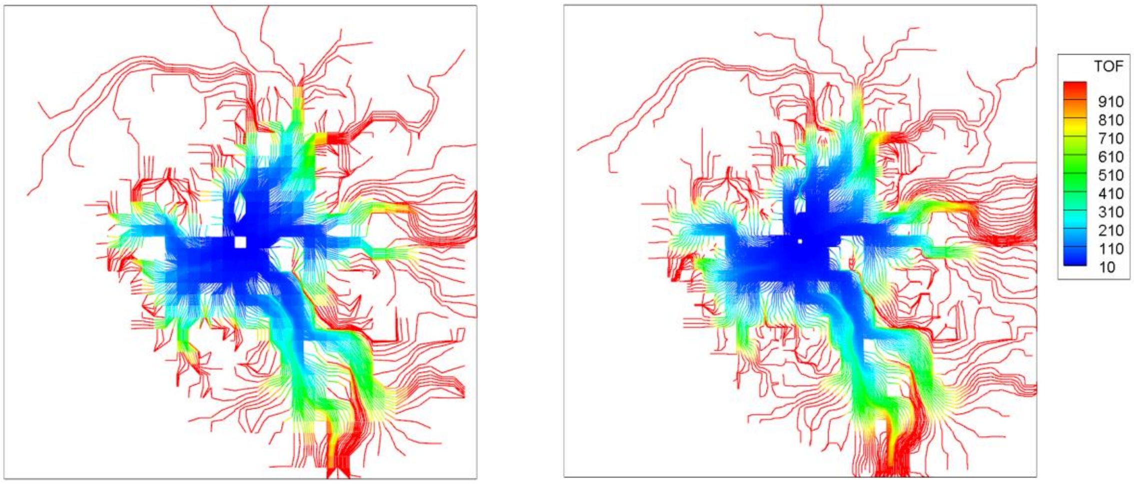

(a) (b)

Figure 2.2: Comparing streamline trajectory and time of flight between (a) regular streamline tracing and (b) multiscale streamline tracing

### 2.2.4 Fluid and Solubility Model

The incremental mass transfer per unit time of CO2 component into the aqueous phase $\Delta m_{c,aq}$ and water into the CO2-rich phase, $\Delta m_{w,g}$ is obtained based on the proposed by Spycher et al. (2003) and Spycher and Pruess (2005) which allows for fast and non-iterative computation of mutual solubility of water and CO2 components in the phases. This extended solubility model which applies for pressure-temperature ranges of interest to CO2 sequestration in saline aquifers, provides equilibrium mole fraction of water dissolved in the CO2-rich phase, $\tilde{y}_w$ and mole fraction of dissolved CO2 in the aqueous phase $\tilde{x}_c$ at specific system pressure, temperature and brine molality using the following equations:

$$\tilde{y}_w = \frac{K^0_{H_2O} a_{H_2O}}{\Phi_{H_2O} P_{tot}} \exp\left( \frac{\left(p - p^0\right)\overline{V}_{H_2O}}{RT} \right) \tag{2.21}$$

$$\tilde{x}_c = \frac{\Phi_{CO_2}\left(1 - \tilde{y}_w\right)P_{tot}}{55.508\gamma'_x K^0_{CO_2}} \exp\left( - \frac{\left(p - p^0\right)\overline{V}_{H_2O}}{RT} \right) \tag{2.22}$$

where $R$ is the gas constant and $K^0$ denotes thermodynamic equilibrium constants for the distribution of water and CO2 components between aqueous and CO2-rich phases at specified Temperature $T$ and reference pressure $p^0 = 1.0 bar$, $\Phi$ denotes component fugacity coefficients in the CO2-rich phase, $\overline{V}$ the partial molar volume of pure phases between reference pressure $p^0$ and $p$. The activity of liquid water due to the presence of dissolved salts is denoted by $a_{H_2O}$, while $\gamma'_x$ denotes the activity coefficient of CO2 dissolved in the aqueous phase. This approach assumes infinite dilution of H2O component in the CO2-rich phase for calculating fugacity coefficients using a calibrated Redlich-Kwong (Redlich and Kwong, 1949) equation of state (Spycher et al., 2003). The mass fraction of H2O tends to be ideally very small in the CO2-rich phase makes the assumption reasonable from the mutual solubility computational accuracy standpoint. The computational advantage of the simplifying assumption is that the equilibrium model reduces to a set algebraic equations used for solving mutual solubilities without iteration once system pressure, temperature and salt molality are known. Computed equilibrium mole fractions are converted to mass fractions and in turn, used in the computation of mutual mass solubilities per time between the phases as will be shown in a later section.

Standard phase property correlations were incorporated in our simulation model based on the high accuracy achievable as well as their limits of validity which subsume the ranges of formation pressures and temperatures of interest for CO2 sequestration in saline aquifers Aqueous phase density was obtained as a volume weighted average of brine density $\rho_{Br}\left(x_{s,Br},T\right)$ and dissolved aqueous CO2 density $\rho_{cd}\left(T\right)$:

$$\rho_{aq}=\rho_{Br}\left(x_{s,Br},T\right)\left\{1-x_c\left(1-\frac{\rho_{Br}\left(x_{s,Br},T\right)}{\rho_{cd}(T)}\right)\right\}^{-1};\quad x_{s,Br}=\frac{x_s}{1-x_c} \tag{2.23}$$

Where brine density $\rho_{Br}\left(x_{s,Br},T\right)$ is obtained from Dittman (1977) correlation which approximates brine density as a function of brine concentration and system temperature. Aqueous CO2 density, on the other hand is computed from the correlation proposed by Garcia (2001) which provides the corrected molar volume of CO2 due to dissolution in the aqueous phase as a function of Temperature in degree Celsius. The corrected density can then be calculated as a ratio of CO2 molecular weight $M_{CO_2}$ and corrected molar volume:

$$\rho_{cd} = \frac{M_{CO_2}}{37.51 - 0.09585T + 8.740\times10^{-4}T^2 - 5.044\times10^{-7}T^3}\times10^6 \tag{2.24}$$

Aqueous phase viscosity $\mu_{aq}$ is computed from the standard correlation by (Kestin et al., 1981) which gives the dynamic viscosity of aqueous solution of NaCl within the temperature range $20-150^{\circ}C$ and pressure range $0.1-35MPa$ with $\pm0.5\%$ accuracy. The CO2-rich phase density, $\rho_g$ follows the Span and Wagner (1996) model which, based on an equation of state, provides $\rho_g$ at temperatures and pressures up to $1100K$ and $800MPa$ respectively with $\pm0.05\%$ accuracy. Dynamic viscosity of CO2-rich phase, $\mu_g$ is computed from the Fenghour et al. (1998) correlation which is valid at temperatures and pressures up to $1000K$ and $300MPa$ respectively with approximate accuracy of $\pm0.3\%$. For simplicity, we have assumed negligible effect of dissolved CO2 on $\mu_{aq}$ and of vaporized water on $\mu_g$ .

## 2.3 Simulation Steps

Our streamline-based simulation approach follows an iterative IMPES scheme as shown in **Fig. 2.3**. At first global iteration, pressure and fluxes are computed based on phase saturations and component concentrations at old time step. New time level phase saturations are obtained from streamline 1D transport solutions followed by corrector solutions as well as equilibrium and reactions calculations on the finite difference grid.

The pressure and flux are computed with updated properties in the second global iteration and the process until global residual is less than specified values. The steps involved are discussed in more detail as follows:

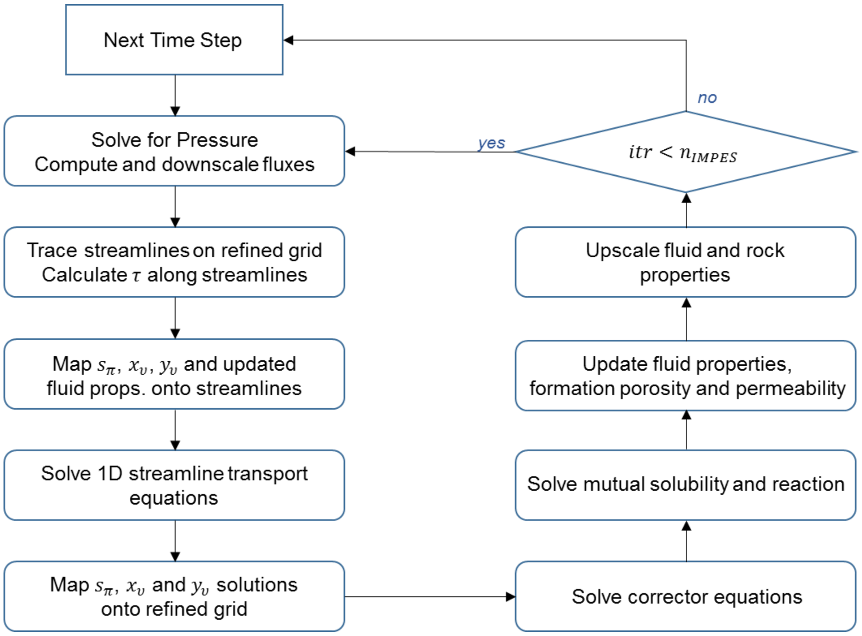

Figure 2.3: Iterative IMPES scheme for streamline simulation

(1) Solve the overall mass balance equation in **Eq. 2.6** to obtain the spatial distribution of the field system pressure at the new time level, $p^{n+1}$ using phase saturations and mass fractions at old time level, $s_\pi^n$, $x^n$, $y^n$. Using the pressure solution, compute phase fluxes using **Eq. 2.8**. Downscale phase fluxes unto the refined grid.

(2) Trace streamlines along total field velocity, obtained from the sum of phase fluxes based on the algorithm proposed by Pollock (1988).

(3) Solve phase and component transport equations along streamlines using **Eqs. 2.14 – 2.17**. This step results in intermediate phase saturations and component mass fractions $s_\pi^{n+1/2}, x^{n+1/2}$, $y^{n+1/2}$ in each streamline segment.

(4) Next is to solve for mutual solubility to redistribute the components between the CO2-rich and aqueous phases by readjusting their respective mass fractions $x^{n+1/2}$ and $y^{n+1/2}$ along each streamline. The following are the steps involved for an arbitrary streamline segment:

   i. Similar to Qi et al. (2009) we start by computing overall initial masses of CO2 $(M_c)$, water $(M_w)$ and salt $(M_s)$ present per bulk volume:

$$
\begin{aligned}
M_c &= \phi^n \left[ x_c^{n+1/2} \rho_w^{n+1/2} s_w^{n+1/2} + \left(1 - y_w^{n+1/2}\right) \rho_g^{n+1/2} s_g^{n+1/2} \right] \\
M_w &= \phi^n \left[ \left(1 - x_c^{n+1/2} - x_s^{n+1/2}\right) \rho_{aq}^{n+1/2} s_{aq}^{n+1/2} + y_w^{n+1/2} \rho_g^{n+1/2} s_g^{n+1/2} \right] \qquad (2.25) \\
M_s &= \left(\phi_0^n - \phi^n\right) \rho_s + \phi^n x_s^{n+1/2} \rho_{aq}^{n+1/2} s_{aq}^{n+1/2}
\end{aligned}
$$

   Where $\rho_s$ denotes salt density and $\phi_0^n$ porosity prior to salt precipitation

   ii. Next is to calculate salt molality, $n_s$ for the equilibrium component mole fractions:

$$
n_s = \frac{x_{s,Br}}{1 - x_{s,Br}} \frac{1000}{MW_{salt}}; \quad x_{s,Br} = \frac{x_s^{n+1/2}}{1 - x_c^{n+1/2}} \qquad (2.26)
$$

   where $x_{s,Br}$, the salt mass fraction in the aqueous phase without dissolved CO2 component.

iii. Compute equilibrium mole fractions of CO2 ( $\tilde{x}_c$ ) and H2O ( $\tilde{y}_w$ ) in the aqueous and CO2-rich phases using **Eqs. 2.21** and **2.22**. These are then converted to mass fractions:

$$y_w^{n+1} = \frac{\tilde{y}_w.MW_{H_2O}}{\tilde{y}_w.MW_{H_2O} + (1-\tilde{y}_w).MW_{CO_2}} \tag{2.27}$$

$$x_c^{n+1} = \frac{\tilde{x}_c.MW_{CO_2}}{\tilde{x}_c.MW_{CO_2} + \tilde{x}_s.MW_{salt} + (1-\tilde{x}_s-\tilde{x}_s).MW_{H_2O}} \tag{2.28}$$

iv. Update phase saturations based on the new equilibration mass fractions:

$$s_{aq}^{n+1} = \frac{1}{\phi^n \rho_{aq}^{n+1}} \left[ \frac{M_w - y_w^{n+1}(M_w + M_c)}{((1-x_s^{n+1/2})(1-y_w^{n+1}) - x_c^{n+1}} \right]; \quad s_g^{n+1} = 1.0 - s_{aq}^{n+1}$$

(2.29)

Negative phase saturation in this step signifies phase disappearance which necessitates an update in component mass fractions in the remaining phase:

$$\text{If } s_{aq}^{n+1} > 1.0: \ s_g^{n+1} = 0; \ y_w^{n+1} = 0; \ x_c^{n+1} = \frac{M_c}{\phi^n \rho_w}; \ x_s^{n+1/2} = x_{s,Brine}\left(1 - x_c^{n+1/2}\right) \tag{2.30}$$

$$\text{If } s_{aq}^{n+1} < 0.0: \ s_g^{n+1} = 1.0; \ y_w^{n+1} = 1 - \frac{M_c}{\phi^n \rho_g}; \ x_c^{n+1} = 0; \ x_s^{n+1/2} = 0 \tag{2.31}$$

v. The final step in the mutual solubility calculations is to cater for salt dissolution and precipitation which contributes to the formation dry-out phenomenon. Salt precipitates if salt mass fraction in CO2-free aqueous solution, $x_{s,Br} > x_{s,Br}^{CR}$ . Here $x_{s,Br}^{CR}$ denotes the critical salt mass fraction which represents the maximum salt concentration that can dissolve in CO2-free aqueous solution at the system temperature. This is computed from the Potter et al. (1977) correlation which provides $x_{s,Br}^{CR}$ as a function of temperature $T$ in ${}^\circ C$ :

$$x_{s,Br}^{CR} = 0.26218 + 7.2 \times 10^{-5} T[{}^\circ C] + 1.06 \times 10^{-6} \left(T[{}^\circ C]\right)^2 \tag{2.32}$$

vi. To account for salt precipitation, first total mas of water dissolved in the CO2-rich phase, $m_{wg}$ and of salt dissolved in the aqueous phase, $m_{sw}$ are calculated:

$$m_{wg} = \phi^n \rho_g s_g^{n+1} y_w^{n+1}; \quad m_{sw} = M_s - \left(\phi_0^n - \phi^n\right)\rho_s \tag{2.33}$$

Then used in the computation of $x_{s,Br}$ as follows:

$$x_{s,Br} = \frac{X_s}{1 + X_s}; \quad X_s = \frac{m_{sw}}{M_w - m_{wg}} \tag{2.34}$$

These are then supplied to the following to algorithm from which the final salt mass fraction update $x_s^{n+1}$, intermediate porosity (due to precipitation) $\phi^{n+1/2}$ and updated salt molality $n_s$ of the aqueous phase are obtained:

***If*** $x_{s,Br} > x_{s,Br}^{CR}$ : Salt precipitates out of aqueous phase

$$m_{s,PPT} = \left(\phi^n s_{aq}^{n+1} \rho_{aq} - m_{wg}\right)\left(1 - x_c^{n+1}\right)\left(x_{s,Br} - x_{s,Br}^{CR}\right) \tag{2.35}$$

$$\phi^{n+1/2} = \phi^n - m_{s,PPT} / \rho_s \; ; \quad x_s^{n+1} = \frac{x_{s,Br}^{CR}}{1 - x_c^{n+1}} \; ; \; n_s = \frac{x_{s,Br}^{CR}}{1 - x_{s,Br}^{CR}} \frac{1000}{MW_{salt}} \tag{2.36}$$

***Else If*** $\phi^n \le \phi_0^n$ : Apparent salt concentration is subcritical; precipitated salt is present

$$m_{s,PPT} = \left(\phi_0^n - \phi^n\right)\rho_s - \left(\phi^n s_{aq}^{n+1} \rho_{aq} - m_{wg}\right)\left(1 - x_c^{n+1}\right)\left(x_{s,Br}^{CR} - x_{s,Br}\right) \tag{2.37}$$

***If*** $m_{s,PPT} \ge 0$ : Part of precipitated salt dissolves, leaving $m_{s,PPT}$

$$\phi^{n+1/2} = \phi_0^n - m_{s,PPT} / \rho_s \ ;\ x_s^{n+1} = \frac{x_{s,Br}^{CR}}{1 - x_c^{n+1}} \ ;\ n_s = \frac{x_{s,Br}^{CR}}{1 - x_{s,Br}^{CR}} \frac{1000}{MW_{salt}} \tag{2.38}$$

***Else***: All precipitated salt dissolve in aqueous phase

$$\phi^{n+1/2} = \phi_0^n \ ;\ n_s = \frac{M_s}{M_w - m_{wg}} \frac{1000}{MW_{salt}} \tag{2.39}$$

$$x_s^{n+1} = \frac{\left(1 - x_c^{n+1}\right) n_s \, MW_{salt} / 1000}{1 + n_s \, MW_{salt} / 1000}$$

***End***

***End***

The impact of formation dry out is significant near the CO2 injector. When large volume of dry CO2 comes in contact with the aqueous phase resulting in more water from the aqueous phase vaporizing into the CO2-rich phase. This results in significant increase in $m_{wg}$ and in turn, in $x_{s,Br}$ until a certain point where calculated $x_{s,Br} > 1$ leading to a negative calculated salt molality, $n_s$. At this stage the streamline segment cell completely dries up and phase saturations and component mass fractions are updated as follows:

$$\phi^{n+1/2} = \phi^n \left( 1 - \frac{\rho_{aq} s_{aq}^{n+1} x_s^{n+1}}{\rho_s} \right) \tag{2.40}$$

$$s_{aq}^{n+1} = 0 \ ;\ s_g^{n+1} = 1 \tag{2.41}$$

$$y_w^{n+1} = 1 - \frac{M_c}{\phi^n \rho_g} \ ;\quad x_c^{n+1} = x_s^{n+1} = 0 \tag{2.42}$$

(5) Map updated phase saturations, component mass fractions and porosity from streamlines to the refined grid to correct for gravity and capillary effects. Repeat step

4 on the grid. Note that corrections on the grid due to transverse fluxes as well as mutual solubility, and consequently resulting changes in saturations and mass fractions, are very minimal and require a very small fraction of the overall computation cost.

(6) Incremental mass of CO2 dissolved in the aqueous phase $\Delta m_{c,aq}^{n+1}$ and of water dissolved in the CO2-rich phase $\Delta m_{w,g}^{n+1}$ needed for the system pressure update are thus computed as follows using updated phase saturations and component mass fractions.

$$\begin{aligned} \Delta m_{c,aq}^{n+1} &= \phi^{n+1/2} s_w^{n+1} x_c^{n+1} - \phi^n s_w^n x_c^n \\ \Delta m_{w,g}^{n+1} &= \phi^{n+1/2} s_g^{n+1} y_w^{n+1} - \phi^n s_g^n y_w^n \end{aligned} \tag{2.43}$$

(7) The final update of the grid porosity is obtained after accounting for reaction. Similar to Obi and Blunt (2006) we have assumed a simple first order reaction between aqueous CO2 and dissolved salt to permanently deposit a secondary mineral on the pore walls of the grid. We start by calculating the limiting reaction concentration as follows:

$$C_0 = \rho_{aq} \min\left( x_c^{n+1} \big/ MW_{CO_2}, x_s^{n+1} \big/ MW_{salt}, (1 - x_c^{n+1} - x_s^{n+1}) \big/ MW_{H_2O} \right) \tag{2.44}$$

Therefore changes due to chemical reaction of rate constant $k$ over time step $\Delta t$ can be obtained as:

$$\frac{\phi^{n+1}}{\phi^{n+1/2}} = \frac{\phi_0^{n+1}}{\phi_0^n} = 1 - C_0 s_{aq}^{n+1} MW_{RockSalt} \left(1 - e^{-k\Delta t}\right) \big/ \rho_{RockSalt} \tag{2.45}$$

Here $MW_{RockSalt}$ and $\rho_{RockSalt}$ denote molecular weight and density of the reaction product – deposited secondary mineral. Note that we have assumed similar percentage change in $\phi$ and $\phi_0$ which are grid porosity with and without aqueous salt precipitation respectively. Incremental aqueous phase and component mass change due to chemical reaction needed for the pressure update is calculated as follows:

$$\Delta m_{Rxn} = C_0 s_{aq}^{n+1}\left(1 - e^{-k\Delta t}\right)\left(MW_{CO_2} + MW_{salt} + MW_{H_2O}\right) \tag{2.46}$$

$$\Delta m_{Rxn,c} = C_0 s_{aq}^{n+1} MW_{CO_2}\left(1 - e^{-k\Delta t}\right);\ \Delta m_{Rxn,s} = C_0 s_{aq}^{n+1} MW_{salt}\left(1 - e^{-k\Delta t}\right)$$

(8) Grid permeability is updated as a consequence grid porosity changes due to aqueous salt precipitation and chemical reaction. In our approach we adopted the 'tube-in-series' model proposed by Verma and Pruess (1988). The two-parameter model is based on the fractional length of pore bodies $\Gamma$ and the fraction of original grid porosity $\phi_r$ for which permeability vanishes. Using this model, the fractional change in permeability is given as:

$$\frac{k}{k_0} = \theta^2 \frac{1 - \Gamma + \Gamma/\omega^2}{1 - \Gamma + \Gamma\left[\theta/\theta + \omega - 1\right]^2} \tag{2.47}$$

$$\theta = \frac{1 - S_s - \phi_r}{1 - \phi_r};\ \omega = 1 + \frac{1/\Gamma}{1/\phi_r - 1}$$

Where $k_0$ and $k$ are original and updated grid permeability values respectively. For all the examples presented in this work we have assumed 0.8 for values of $\phi_r$ and $\Gamma$, while solid phase saturation is computed as $S_s = 1 - \phi^{n+1}/\phi_{00}$, where $\phi_{00}$ represent original grid porosity.

(9) Upscale grid properties on the coarse grid for the next global pressure solve. First upscale updated grid porosities using bulk volume weighted averages. Then saturations and concentrations based on pore volume weighted averages. Finally,

update coarse scale permeability values based on as a geometric mean of harmonic-arithmetic and arithmetic-harmonic resultant permeability values.

The iterative IMPES approach uses updated phase saturations and component mass fractions through the global iteration process. This leads to better accommodation of the effects of buoyancy and rock property changes due to precipitation and reaction and improves the solution after 2 or 3 iterations based on our observation. Processes with small viscous to gravity ratios will likely require more iterations to reach the specified global convergence criteria. It is worthwhile to note that an alternative algorithm may involve carrying out mutual solubility calculations on finite difference grid after step 5 (Qi et al, 2009). However, as we will show later on, this results in critical phenomena such as salt precipitation and effect on well injectivity being poorly captured especially for strongly water-wet formations.

Once the injection well is shut-in well fluxes go to zero, meaning streamline-based convection calculations are no longer available. As a result, our formulation identically reduces to a conventional finite difference method to account for transverse fluxes (gravity, capillarity and diffusion) and chemical reaction. Simulation results from our streamline-based approach have been compared with that from a commercial finite difference simulator with emphasis on simulation responses during the injection period. This is because accurate prediction of fluid phase and component concentration distribution at injection shut-in is fundamental to reliable modelling of long term CO2 trapping mechanisms post-injection.

## 2.4 Case Examples

We present examples to validate our streamline-based simulation approach with the CO2STORE module in ECLIPSE reservoir simulator (Schlumberger, 2014). CO2STORE is a dedicated commercial simulator for carbon sequestration in saline aquifers which models relevant trapping mechanisms and accounts for underlying physics. We begin with a simple 1D problem and then to 2D homogeneous and heterogeneous cross-section models to demonstrate buoyancy effects on CO2 plume propagation. We have assumed negligible capillarity and molecular diffusion effects for the time being, although these effects can be accounted for using operator splitting technique (Obi and Blunt, 2006). We have applied the parameters in **Table 2.1** to all simulation cases presented in this work. We will discuss the computational benefit afforded by our streamline simulation-based simulation approach compared with finite difference models.

Next, we compare the results from mutual solubility calculations on streamline segments and on finite difference grids after the mapping step. We then compare the differences in responses with and without capillarity to illustrate the impact of accounting for mutual solubility. Finally, to demonstrate the robustness of our approach, we apply the streamline-based simulation approach to evaluate the Johansen field CO2 sequestration project.

### *2.4.1 Example 1: 1D Case*

The first example models a 1D convection problem. The essence of this case is to provide a conceptual model for quick illustration of the physics associated with CO2 injection while we ignore influence of gravity segregation for the time being, and also to validate the correct handling of phase saturation and component concentration calculations in our method by comparing with results from CO2STORE using an equivalent input set. The model comprises a homogeneous rectangular rock piece of length $200ft$, discretized into $200$grid cells of equal dimension$1ft \times 1ft \times 1ft$ as shown in **Fig. 2.4**. The rock is assumed to have uniform initial permeability and porosity values of $100mD$and $0.2$ respectively with negligible capillary effects. Initial pressure and brine saturation were $1500psia$ and 1.0 respectively. Dry CO2 is injected at $5.0Mscf/D$ for $1.5Days$(equivalent of$0.425PVI$ cumulative) while the other end is open to flow and thus, maintained at the initial pressure of$1500psia$ to simulate a continuous aquifer and to prevent unwanted premature pressure buildup in the formation.

Table 2.1: General simulation parameters

| **Parameter** | **Value** |
|---|---|
| Aquifer Temperature [$^\circ F$] | 140 |
| Brine Salinity [mass fraction NaCl] | 0.2 |
| First Order Reaction Rate [$/yr$] | 5.0E-04 |
| Salt Density, $\rho_s$ [$lb/ft^3$] | 135 |
| CO2 Surface Density, $\rho_g^\circ$ [$lb/ft^3$] | 0.116 |
| Pure Water Surface density, $\rho_w^\circ$ [$lb/ft^3$] | 62.37 |
| Rock Salt Density, $\rho_{Rocksalt}$ [$lb/ft^3$] | 135 |
| Molecular Weight of Salt, $MW_{salt}$ [$lb/lb-mol$] | 58.4 |
| Molecular Weight of CO2, $MW_{CO_2}$ [$lb/lb-mol$] | 44.0 |
| Molecular Weight of Water, $MW_{H_2O}$ [$lb/lb-mol$] | 18.0 |
| Molecular Weight of Rock Salt, $MW_{Rocksalt}$ [$lb/lb-mol$] | 100 |
| Aqueous Phase Endpoint Relative Permeability, $k_{r,aq}^e$ [-] | 0.95 |
| Aqueous Phase Relative Permeability Exponent, $n_{aq}$ [-] | 4.0 |
| Aqueous Phase Critical Saturation, $s_{wc}$ [-] | 0.1 |
| CO2-rich Phase Endpoint Relative Permeability, $k_{rg}^e$ [-] | 0.4 |
| CO2-rich Phase Relative Permeability Exponent, $n_g$ [-] | 2.0 |
| CO2-rich Phase Residual Saturation, $s_{gr}$ [-] | 0.2 |

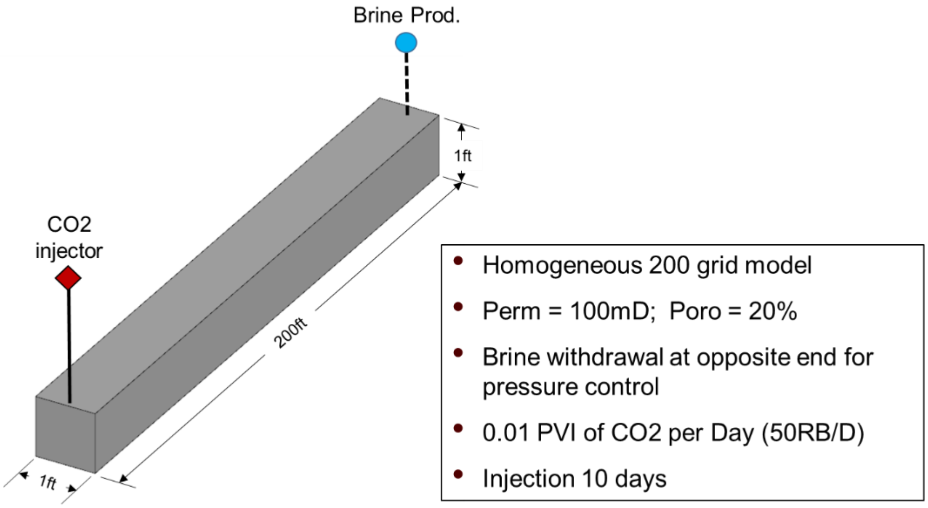

- Homogeneous 200 grid model
- Perm = 100mD; Poro = 20%
- Brine withdrawal at opposite end for pressure control
- 0.01 PVI of CO2 per Day (50RB/D)
- Injection 10 days

Figure 2.4: Set-up for the 1D simulation case showing the CO2 injector at one end of the porous of rock and the brine producer well (used to mimic a semi-infinite medium) on the other end

Simulation results in terms of grid pressure, CO2-rich phase saturation and aqueous CO2 and salt mass fractions are compared with CO2STORE at $0.5Day$, $1.0Day$ and $1.5Days$ as shown in **Fig. 2.5**. All comparisons show excellent agreement with the commercial finite difference simulator. It is easy to notice the effect of fluid compressibility and mobility effects in the pressure profile as indicated by sharp differences in pressure gradients between the two phase region and the brine phase region. Consequently, ignoring compressibility effects, as in previous streamline-based simulation methods, may result in erroneous flux computations computation leading to incorrect CO2 plume migration predictions.

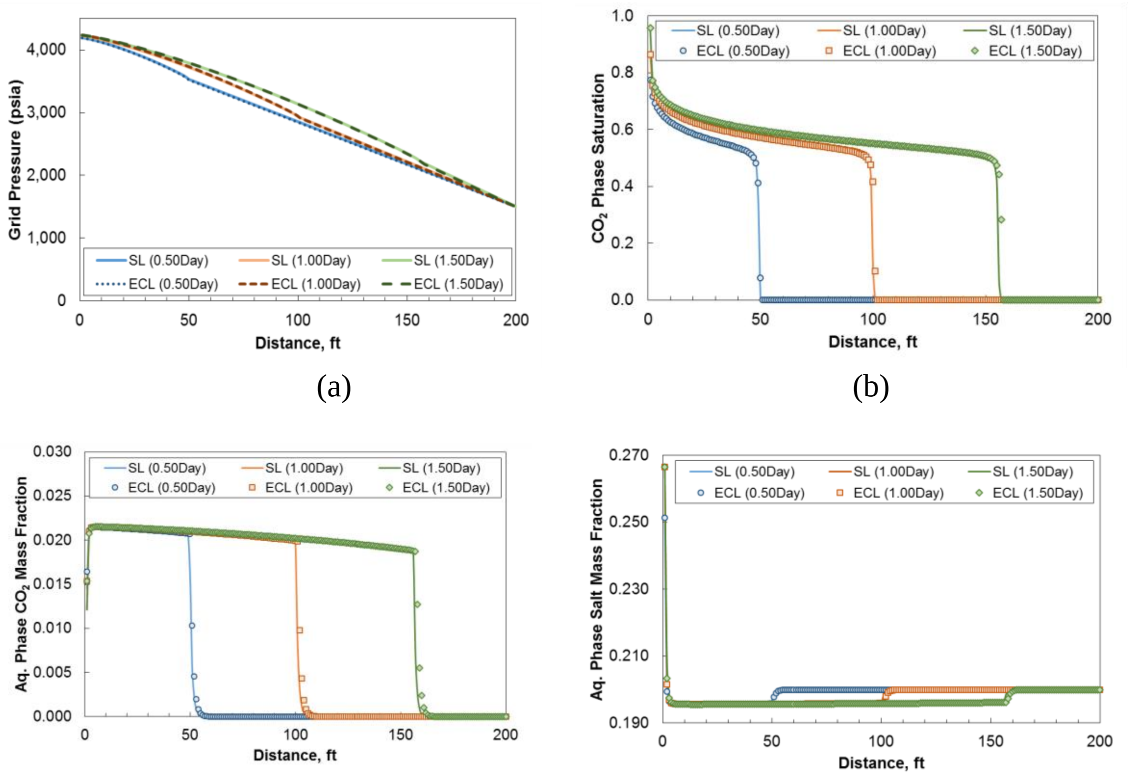

(a)

(b)

(c)

(d)

Figure 2.5: Model validation in 1D with commercial FD compositional simulator showing (a) Grid pressure profile (b) CO2-rich phase saturation (c) Aqueous phase CO2 mass fraction, and (d) Aqueous phase salt mass fraction

Behind the two phase front, aqueous phase CO2 concentration shows an expected slight variation with grid pressure which is consistent with experimental data (Spycher and Pruess, 2005). An equally important feature captured by our model is the slow evaporation of water from the aqueous phase into the CO2-rich phase which results in gradual drying out of the grid cells in the vicinity of the CO2 injection well or completion. This causes a sharp increase in the salt concentration and in turn, a decrease in aqueous phase CO2 concentration. The aqueous phase saturation gradually decreases below critical value and, depending on the injection rate and duration, completely vanishes eventually leaving a CO2-rich phase saturation equal to 1.0. In streamline based simulation methods, these phenomena are difficult to capture without mutual solubility calculations on streamline segments prior to mapping to the finite difference grid.

### *2.4.2 Example 2: Homogeneous 2D Cross Section*

Next we demonstrate a cross-section model to illustrate the effect of buoyancy during CO2 injection and post-injection periods. Consider a slice of porous media of length $5298 ft$, width $5.298 ft$ and depth $50 ft$ uniformly discretized into $100\times1\times50$ grids as shown in **Fig. 2.6(a)**. We assume homogeneous permeability and porosity value of $100 mD$ and $0.2$ respectively with negligible capillary effects. Dry CO2 is injected at a constant reservoir volume rate of $50 RB/D$ ($0.01 PVI/D$ equivalent) through an injection well (shown in red line in **Fig. 2.6(a)**) completed only in the bottom three layers of the model. Brine saturation and initial pressure were kept constant at $1.0$ and $2500 psia$ respectively at initial conditions. To imitate open aquifers, pressure was maintained constant at the other end of the model throughout the injection period. Supercritical CO2 is injected for a period of 10 days before injection well shut in, after which plume migration was monitored over a period of 1000 years.

**Figs. 2.6(b)** and **(c)** show the streamline distribution with time of flight contours and CO2 rich phase saturation at the end of CO2 injection period respectively. Solutions are mapped on the underlying grid and compared with the results from CO2STORE. CO2 rich phase saturations are compared in **Fig. 2.7** while aqueous phase CO2 mass fractions are compared in **Fig. 2.8**. Overall, our model showed good agreement with the commercial simulator. High values of CO2 rich phase saturations (and consequently, less than connate aqueous phase saturations) as well as low aqueous phase CO2 mass fractions in the vicinity of the injection completions indicate the impact of formation dry out which is captured by our streamline based simulation method. A well-studied feature of CO2 injection in saline aquifers is flow instability which results from an increase in aqueous phase density due to dissolution of CO2 (Ennis-King and Paterson, 2003; Garcia, 2001; Hesse et al., 2008; Neufeld et al., 2010). This creates a vertical convection current which in turn causes fingering of CO2 bearing aqueous phase through virgin brine phase as shown in **Fig. 2.8**. Besides fluid phase and component concentration profiles on simulation grids, we compared CO2 injector bottomhole pressures (BHP) as a function of time shown in **Fig. 2.9**. A good agreement was also recorded between our approach and CO2STORE.

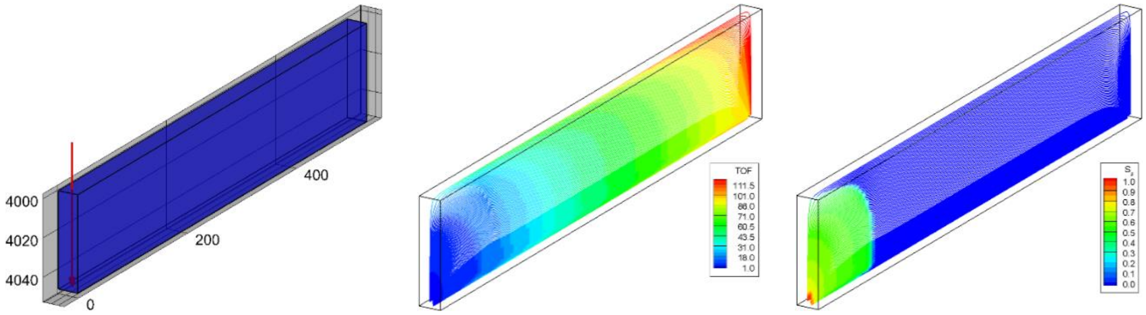

(a) (b) (c)

Figure 2.6: (a) Homogeneous 2D cross-section model showing the CO2 injection well in red line (b) Streamline distribution with Time of Flight contoured along each streamline (c) Saturation of CO2 rich phase at injector shut-in contoured along streamlines

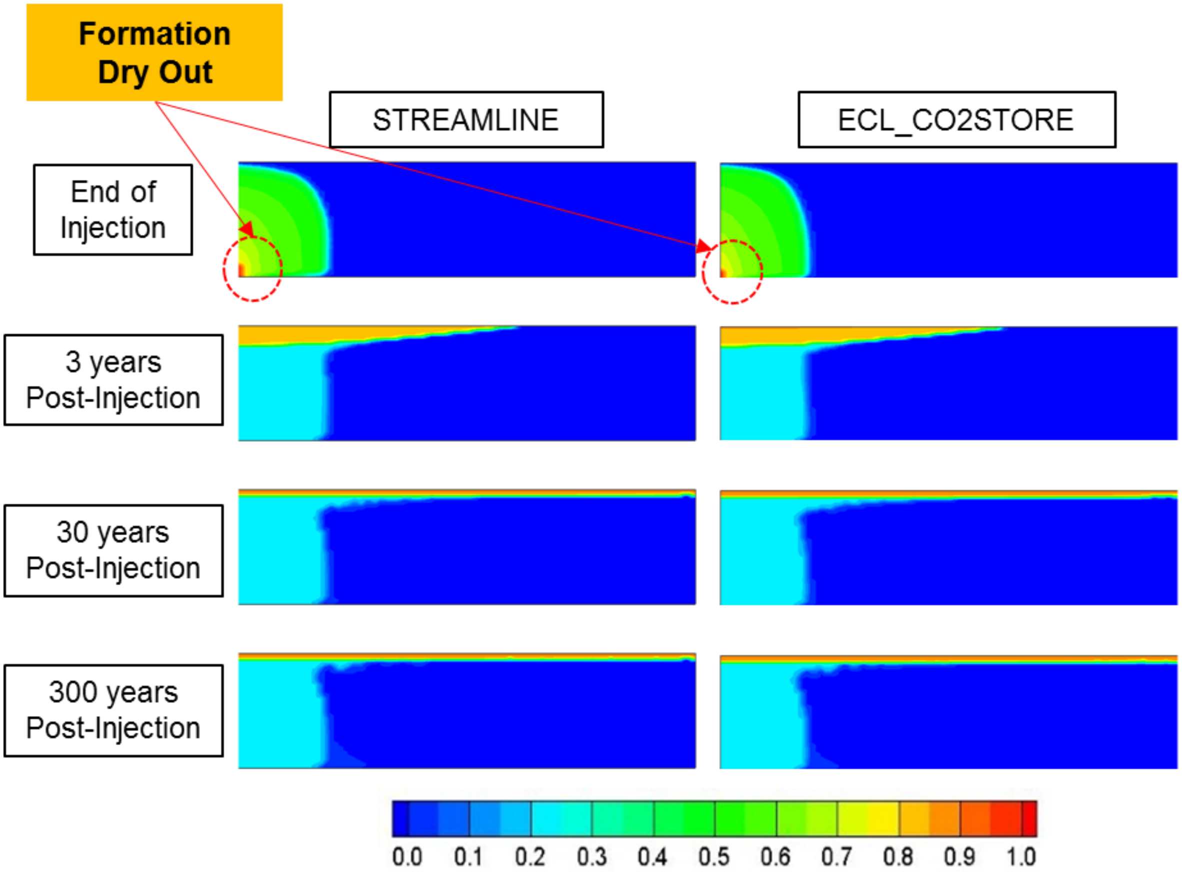

Figure 2.7: Time Lapse of CO2-rich phase saturation for 2D cross-section homogeneous model

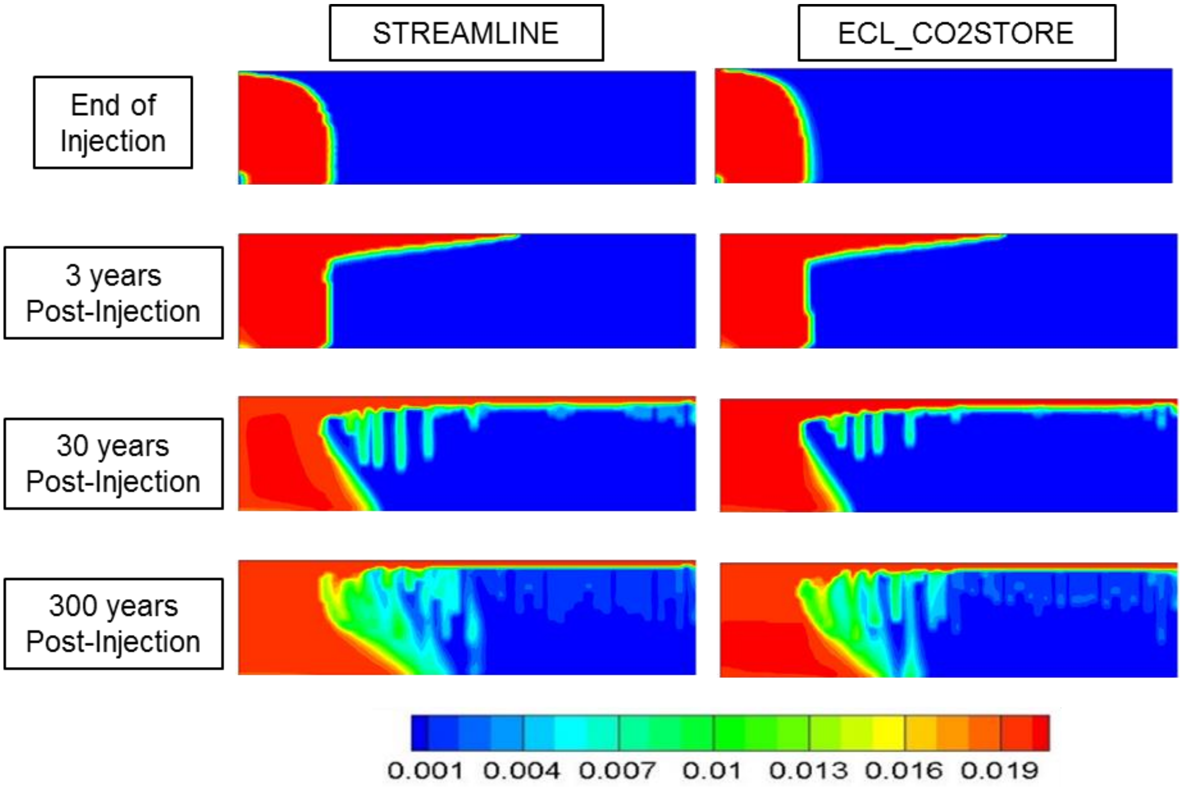

Figure 2.8: Time Lapse of CO2 mass fraction in the aqueous phase for 2D cross-section homogeneous model

Permeability and porosity variations with time throughout the porous media as a result of salt precipitation and mineralization are shown in **Fig. 2.10**. Note that rock porosity and permeability are altered mainly due to salt precipitation during injection period. Time scales of active CO2 trapping mechanisms can be clearly described through the life cycle plot shown in **Fig. 2.11**. After injector shut-in free CO2 plume continues to migrate and get trapped by residual mechanism. This leads to a steady decrease in free CO2 saturation and increase in residual CO2 until the plume hits the other end of the formation in the constrained domain and can no longer migrate. Residual CO2 begins to decline due to dissolution in brine facilitated by gravity fingering and convective mixing.

At 300 years, reaction and CO2 mineralization begin to take effect resulting in significant permeability and porosity reduction throughout the porous media as shown in **Fig. 2.10**.

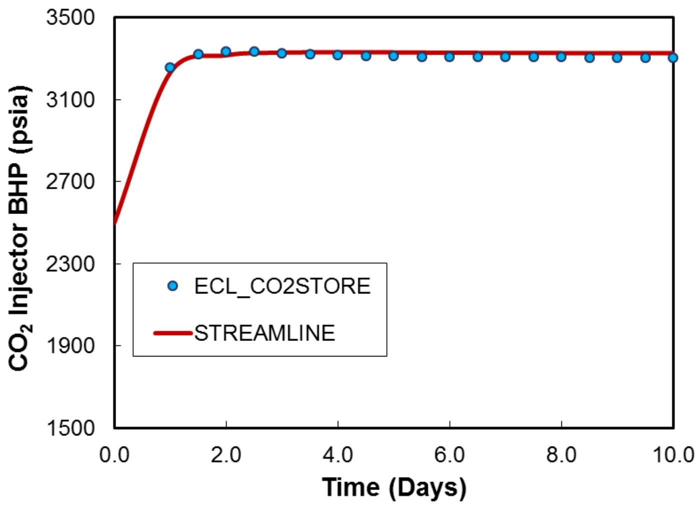

Figure 2.9: CO2 injector bottomhole pressure for homogeneous 2D cross-section homogeneous case

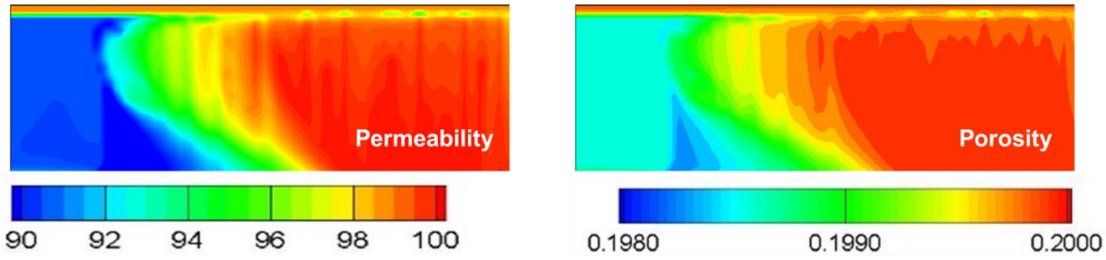

Figure 2.10: Grid porosity and permeability changes due to salt precipitation and reaction at 1000 years, post-injection

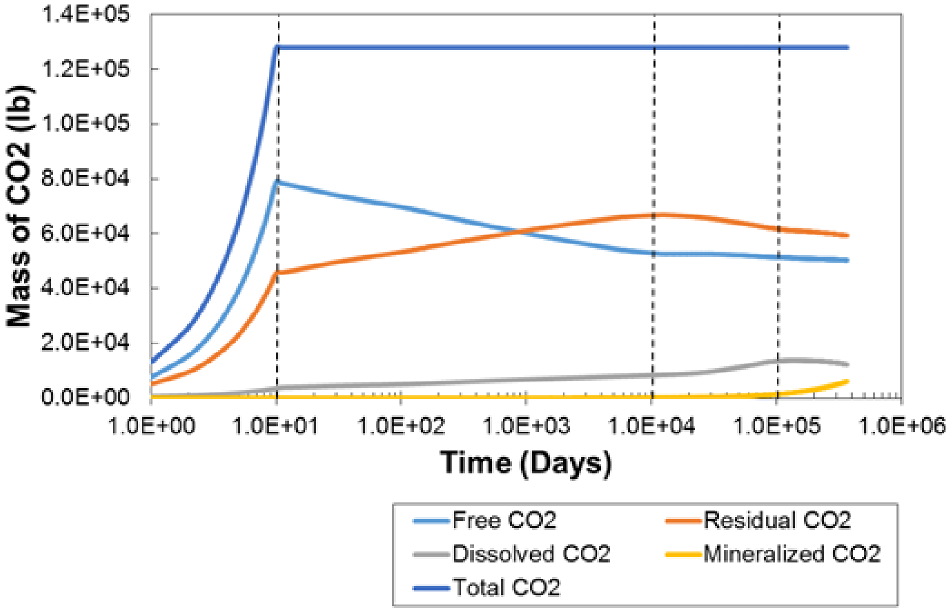

Figure 2.11: CO2 Life cycle over 300 years post-injection for homogeneous 2D cross-section homogeneous case

### *2.4.3 Example 3: Heterogeneous 2D Cross Section*

A study was also conducted using a vertical cross section model with heterogeneous permeability field obtained from the first 35 (non-channelized) layers of the SPE 10 comparative model (Christie and Blunt, 2001). The flow domain is uniformly discretized into $150 \times 1 \times 35$grid cells, each grid have similar dimensions as the homogeneous 2D cross section example discussed above. Grid permeability distribution shown (in natural logarithm) in **Fig. 2.12(a)** ranges between $0.02-8000 mD$ to add more geologic realism into the model. For simplicity, the formation is assumed incompressible while porosity takes a constant value of $0.2$ and capillary fluxes are negligible. Initial conditions are similar with the homogeneous 2D cross section example with initial pressures and brine saturations taking uniform values of $2500 psia$ and $1.0$ respectively. This model likewise consists of a CO2 injector at one end of the rectangular model and completed within the bottom 5 layers of the simulation grid. Similar boundary conditions of $50RB/D$ ($\approx 0.01PV/D$ equivalent) constant injection rate of CO2 and constant pressure at the outlet was imposed over $15 Days$ of CO2 injections. Again, the CO2 plume effects on formation was monitored over a period of 1000 years post-injection.

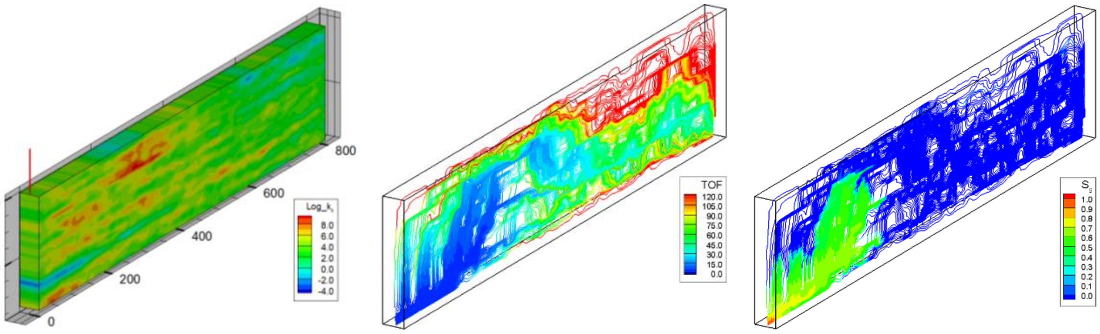

(a) (b) (c)

Figure 2.12: (a) Heterogeneous 2D cross-section model showing logarithm of permeability distribution and CO2 injection well in red line (b) Streamline distribution with Time of Flight contoured along each streamline (c) Saturation of CO2 rich phase at injector shut-in contoured along streamlines

An appealing feature of the streamlines methodology is the intuitive visualization of flow though connected volumes in the heterogeneous domain. The streamline distribution for this model with time of flight contours shown in **Fig. 2.12(b)** provide useful information not only about flow distribution, but also relative connectivity within the domain. Fluids typically flow along preferential paths with lower times of flight along the streamlines. This can be easily observed by visual inspection of the CO2 rich phase saturation at the end of injection as calculated along the streamlines shown in **Fig. 2.12(c)**. Solutions on the streamline time of flight domain are mapped to the Cartesian domain for easy visual comparison with CO2STORE.

Temporal and spatial profiles of CO2 rich phase saturations and aqueous phase CO2 mass fractions on the finite difference grids are compared separately in **Figs. 2.13** and **2.14** respectively. Good agreement between the two simulations methods was recorded as well. Also the near-injection grid precipitation phenomena is well captured as indicated by unit saturations of the CO2 rich phase and lower mass fraction of CO2 dissolved in the aqueous phase. Injector BHP comparison, shown in **Fig. 2.15** likewise shows good agreement between our streamline based method and CO2STORE.

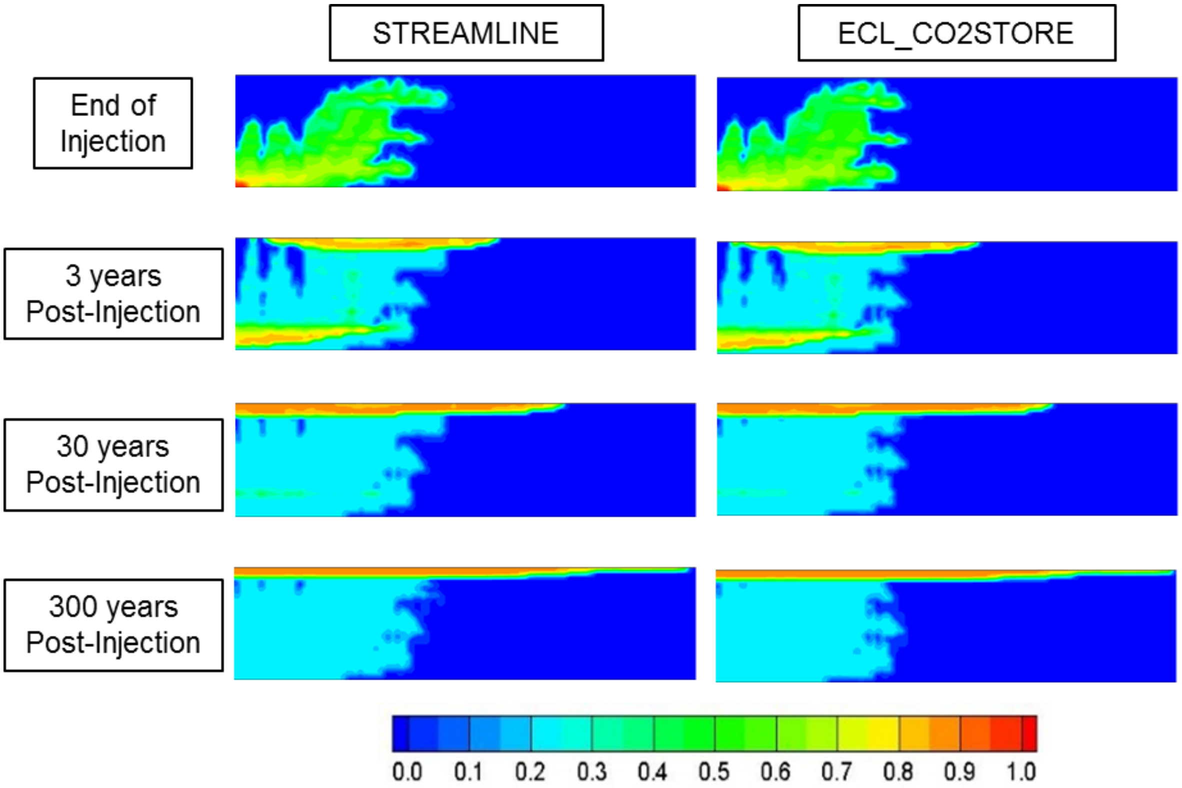

Figure 2.13: Time Lapse of CO2-rich phase saturation for 2D cross-section heterogeneous model

For this example, a CO2 life cycle plot is provided in **Fig. 2.16** as a graphic representation of the variations and time scales of CO2 trapping mechanisms over 1000*years* post-injection. Comparing this plot with **Fig. 2.11**, it can be observed that the point of maximum residual trapping of the CO2 is delayed in the heterogeneous model compared with the homogeneous model. One explanation for this is an improvement in vertical sweep due to flow barriers which delay gravity override in the heterogeneous model even though comparable volumetric rates of CO2 were injected in both cases. Consequently, higher residual trapping results with greater reduction in free CO2 structurally trapped at $1000 years$. Time scales for solubility and mineral trapping are more or less comparable in both the homogeneous and heterogeneous examples, except for slight delay in the onset of convective mixing in the heterogeneous case.

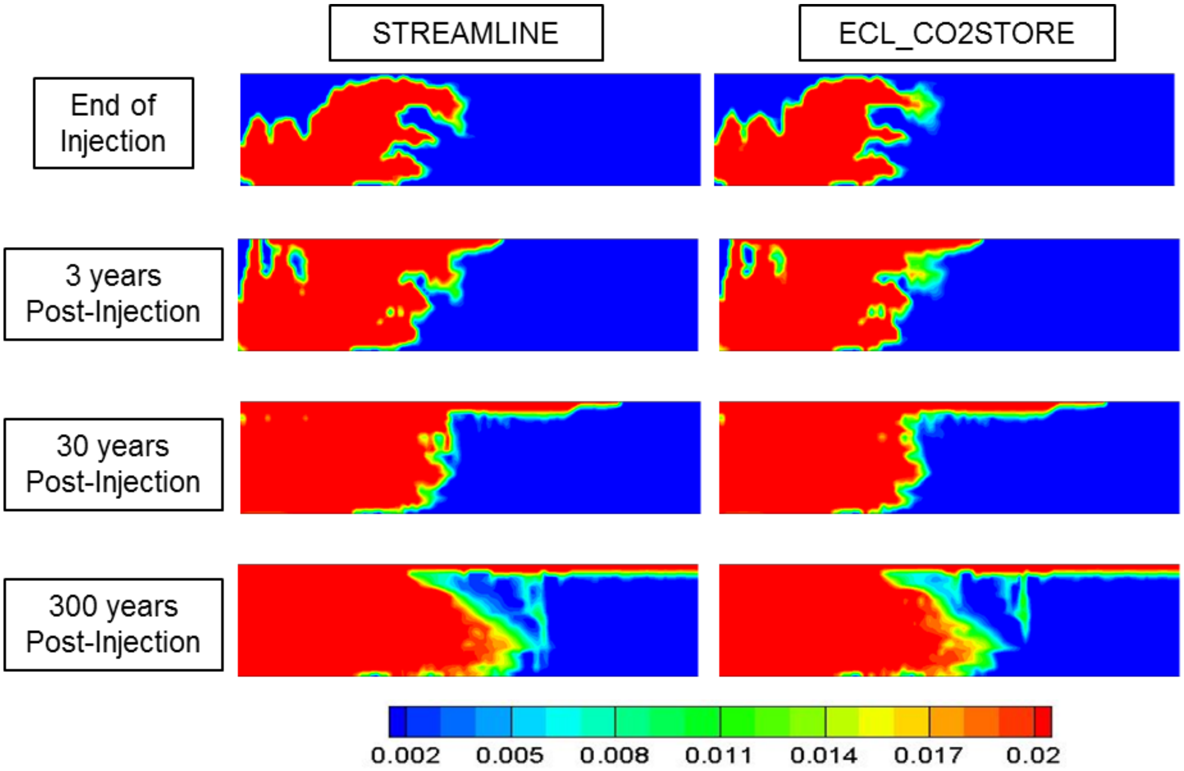

Figure 2.14: Time Lapse of CO2 mass fraction in the aqueous phase for 2D cross-section heterogeneous model

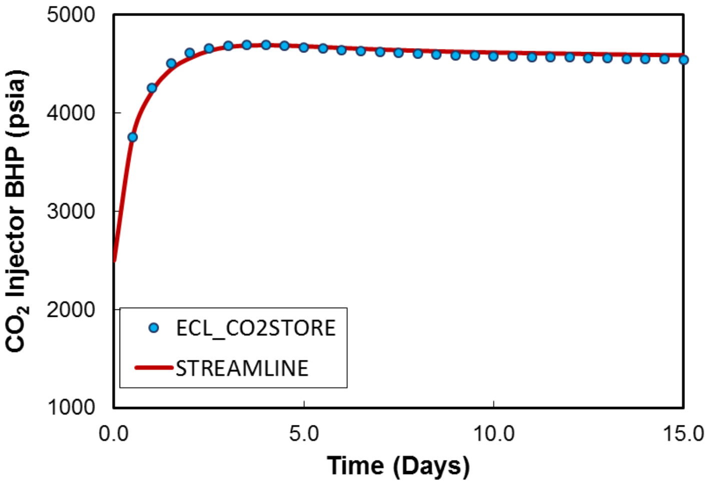

Figure 2.15: CO2 injector bottomhole pressure for heterogeneous 2D cross-section case

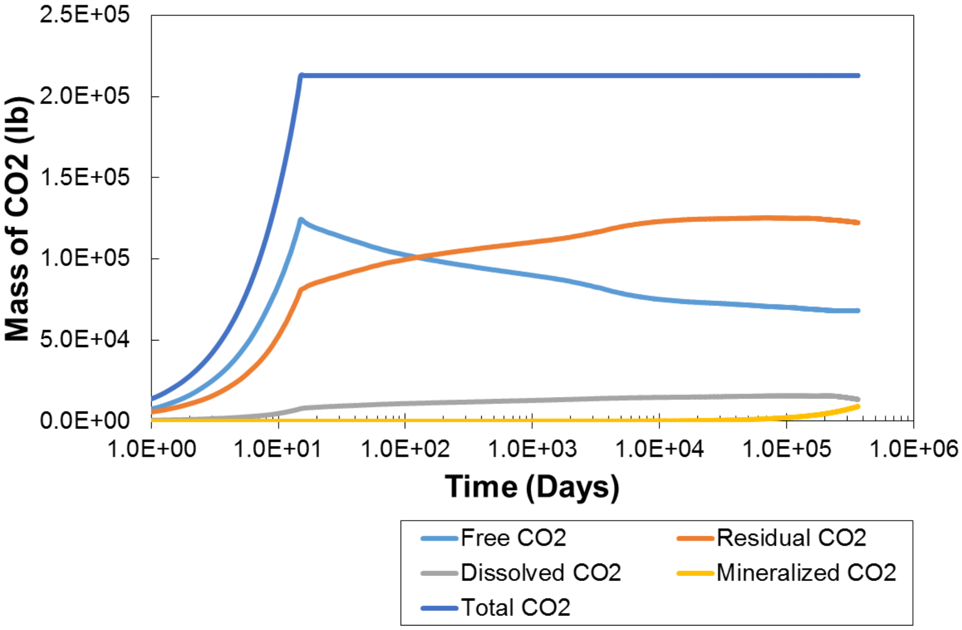

Figure 2.16: CO2 Life cycle over 300 years post-injection for heterogeneous 2D cross-section case

## 2.5 Discussion of Results

In this section we present a summary of the results so far including the computational benefit of our streamline-based methodology compared to conventional finite volume methods. We also provide a description of the improvement offered by our method over existing streamline based methods for CO2 sequestration applications.

### *2.5.1 Value of Streamline Simulation*

The subsurface environment is typically heterogeneous and quick assessment of storage potentials of saline aquifers requires efficient analytic and flow simulation approaches. Streamline simulation has been extensively studied and shown to effectively handle large and small-scale heterogeneities while avoiding grid orientation and numerical artefacts (Batycky, 1997; Chaban Habib, 2005; Datta-Gupta and King, 2007). Consequently, streamline simulation potentially offers benefits in improved tracking of CO2 plume during injection. In all examples presented so far, we have consistently shown reasonable agreement between our simulation approach and commercial finite difference simulator based on standard flow dynamics metrics including spatial profiles of phase saturations, component mass fractions and injector BHP variations with time. Here we investigate the value of our streamline-based simulation methodology in terms of convergence and computational advantage.

#### *2.5.1.1 Convergence Studies*

In this section, we compare simulation convergence performance between the regular streamline methodology, multiscale streamlines approach and finite difference simulation. For both homogeneous and heterogeneous 2D cross-section models, we conducted a series of numerical experiments at various grid resolutions to investigate the rate of convergence of each simulation approach. For both cases, we start with a $40 \times 5$ grid model with $50 \times 50 \times 20\,ft$ grid dimensions and vertically refine by a factor of 2 twice to obtain additional models of vertical grid dimensions $10$ and $20$. The reference model was set to have a vertical grid resolution $nz = 80$. An infinite aquifer domain was mimicked with pore volume multiplier value of $3000$ at both ends of the model. We imposed a constant initial reservoir pressure of $2500\,psia$ for both models and CO2 is injected at $200 RB/D$ over a period of $200 days$. A homogenous porosity value of $0.2$ was applied with permeability value of $100 mD$ for the homogeneous model, while the natural logarithm of permeability for the heterogeneous model ranges from $-6$ to $6$.

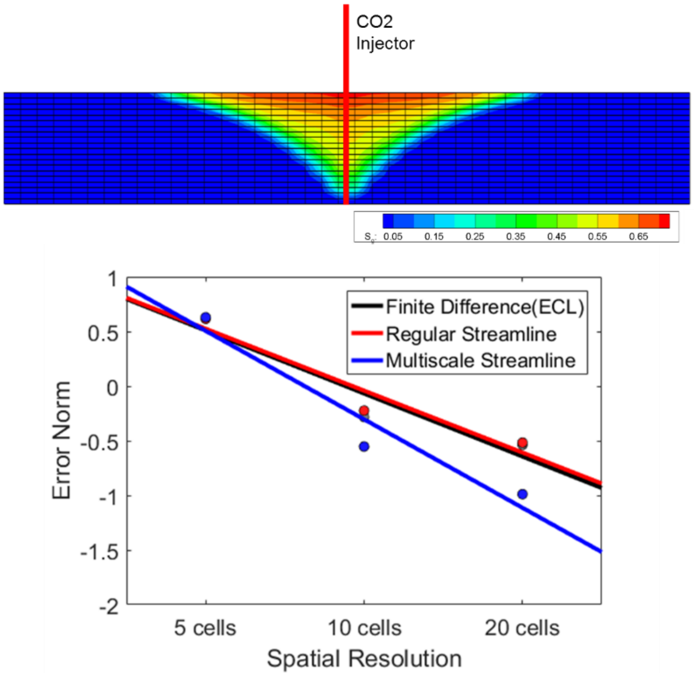

Figure 2.17: Grid resolution study for homogeneous 2D cross-section case showing the gas saturation profile for the 20-cell vertical resolution case (top) and the grid convergence comparison plots (bottom)

The results and observation obtained from the numerical experiments is summarized in **Fig. 2.17** and **2.18** for the homogeneous and heterogeneous models respectively. For all three simulation methods, we summarize the grid resolution experiment with a plot of the error norm, computed as $\log_{10}\left(\left\|s_g - s_{g_{REF}}\right\|\right)$, is plotted against the number of vertical grid cells. The error is simply the L2 norm of the difference between the calculated gas saturation on the low resolution grid $s_g$ and the reference gas saturation computed on the 80-layer grid $s_{g_{REF}}$. An improved convergence was observed with the multiscale streamline simulation methodology for both homogeneous and heterogeneous models.

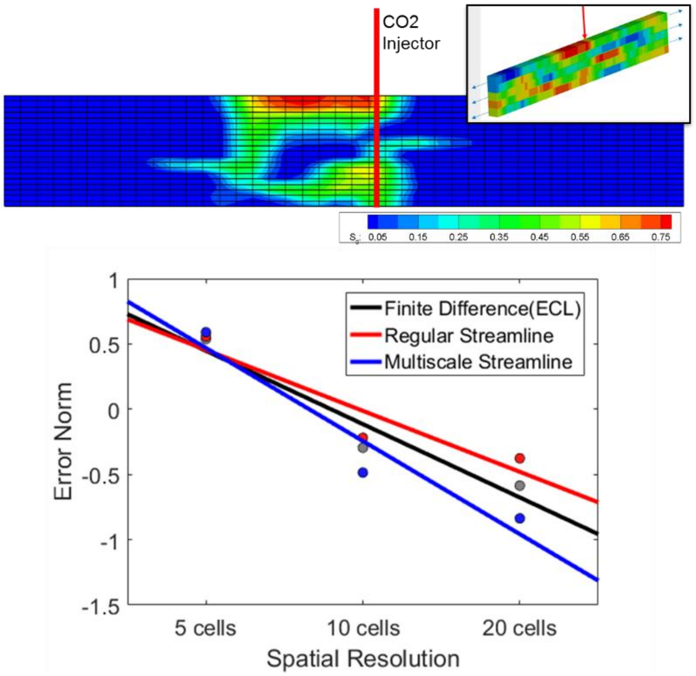

Figure 2.18: Grid resolution study for heterogeneous 2D cross-section case showing the gas saturation profile for the 20-cell vertical resolution case (top) and the grid convergence comparison plots (bottom). Inset shows the *ln*(permeability) distribution on the coarse 5-layer grid

This is seen to be a direct implication of the higher resolution $\tau$ discretization which also allows for gravity corrections on the refined grid, thereby minimizing the smearing effect that results from grid-to-streamline mappings during streamline simulation.

### *2.5.1.2 Time Stepping*

As shown in **Fig. 2.19**, in all the three cases number of required time steps is reduced by a factor of $10$ on the average compared to CO2STORE. This may be attributed to the unique effectiveness of streamline based methods at handling convective transport leaving mild flux corrections per predictor step. Number of iterative IMPES iterations, is thus small for reasonably high injection rates as those practical for CO2 sequestration applications. We however recognize, as a limitation, that this benefit of streamline based approach may diminish as transverse fluxes increase with gravity and/or capillary dominated systems.

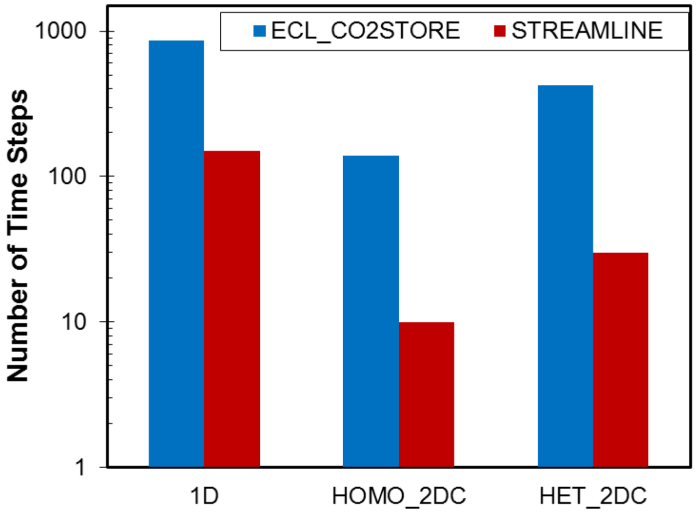

Figure 2.19: Comparison of required number of time steps

### *2.5.2 Flow Visualization*

Here we demonstrate the value of streamline-based flow visualization in providing insights into subsurface flow dynamics during and post injection. Apart for the visual appeal which the streamline method is known for, it enhances the understanding of subsurface flow mechanisms at various stages of CO2 sequestration in saline aquifers. We provide an illustration with the homogeneous 2D-cross-section case discussed in Example 2. **Figs. 2.(a)–(g)** provide series of snapshots covering different flow regimes during injection and post-injection periods. Streamlines, computed based on the total flux field, are overlain on the aqueous phase CO2 mass fraction profiles. To put it in context, the contributions of the four main trapping mechanisms are also provided in intuitive understanding of dominant trapping mechanism associated with each flow regime.

Recall that streamline trajectory can always be computed as long as flux field magnitudes are non-zero within the domain of interest. Forced convection, established by fluid fluxes from wells, results in streamlines which essentially connect the sources and sinks during the injection period as shown in **Figs. 2.(a)** and **(b)**. As mentioned earlier, both CO2 injection and brine producer wells are completed in the lower 5 layers of the model. And due to the high injection rate constraint, resulting in high viscous-to-gravity ratio, flux magnitude is relatively lower above the completion zone. This is clearly depicted by the streamline distribution in the domain.

Natural convection currents take over right after the wells are shut in as shown in **Fig. 2.(c)**. These natural currents result from the expansion of the CO2-rich phase due to a combination of gravity-induced advection forces and compressibility effects (Vilarrasa et al., 2010; Vilarrasa et al., 2013). Here streamlines loop multiple times and only a few streamlines need to be traced to effectively visualize the flux field. The natural currents are sustained through the plume migration period as shown in **2.(d)**. As can be observed from the adjoining plot, the residual trapping contribution become dominant during the plume migration as the CO2-rich phase invade pure brine saturated regions of the aquifer. The increase in the aqueous phase density as a result of CO2 dissolution makes the system becomes dynamically unstable. At a later time, characteristic of the model properties, gravity fingers develop which results in gravity-induced convective mixing as

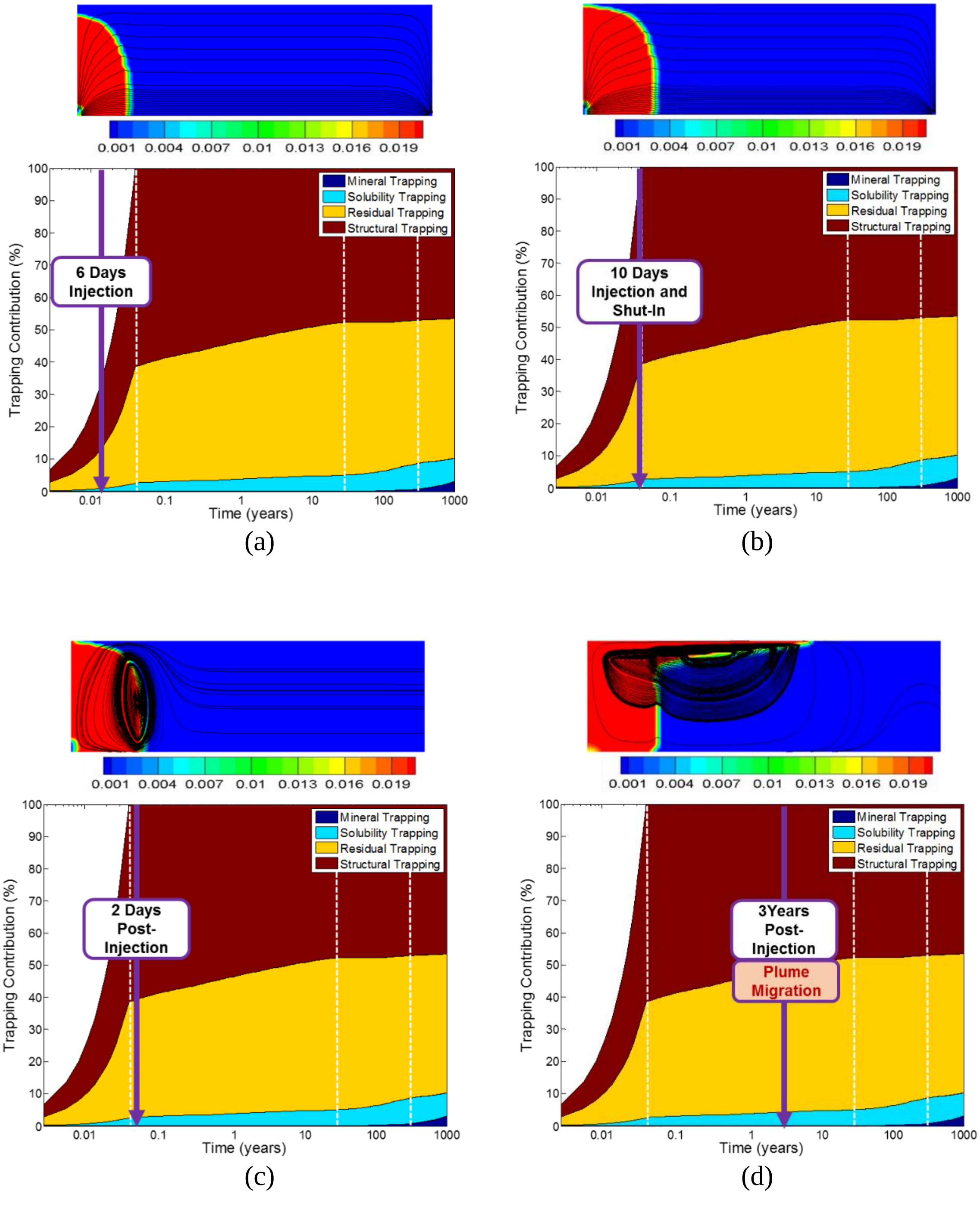

(a) (b)

(c) (d)

Figure 2.20: Flow visualizations before and after CO2 injector shut-in

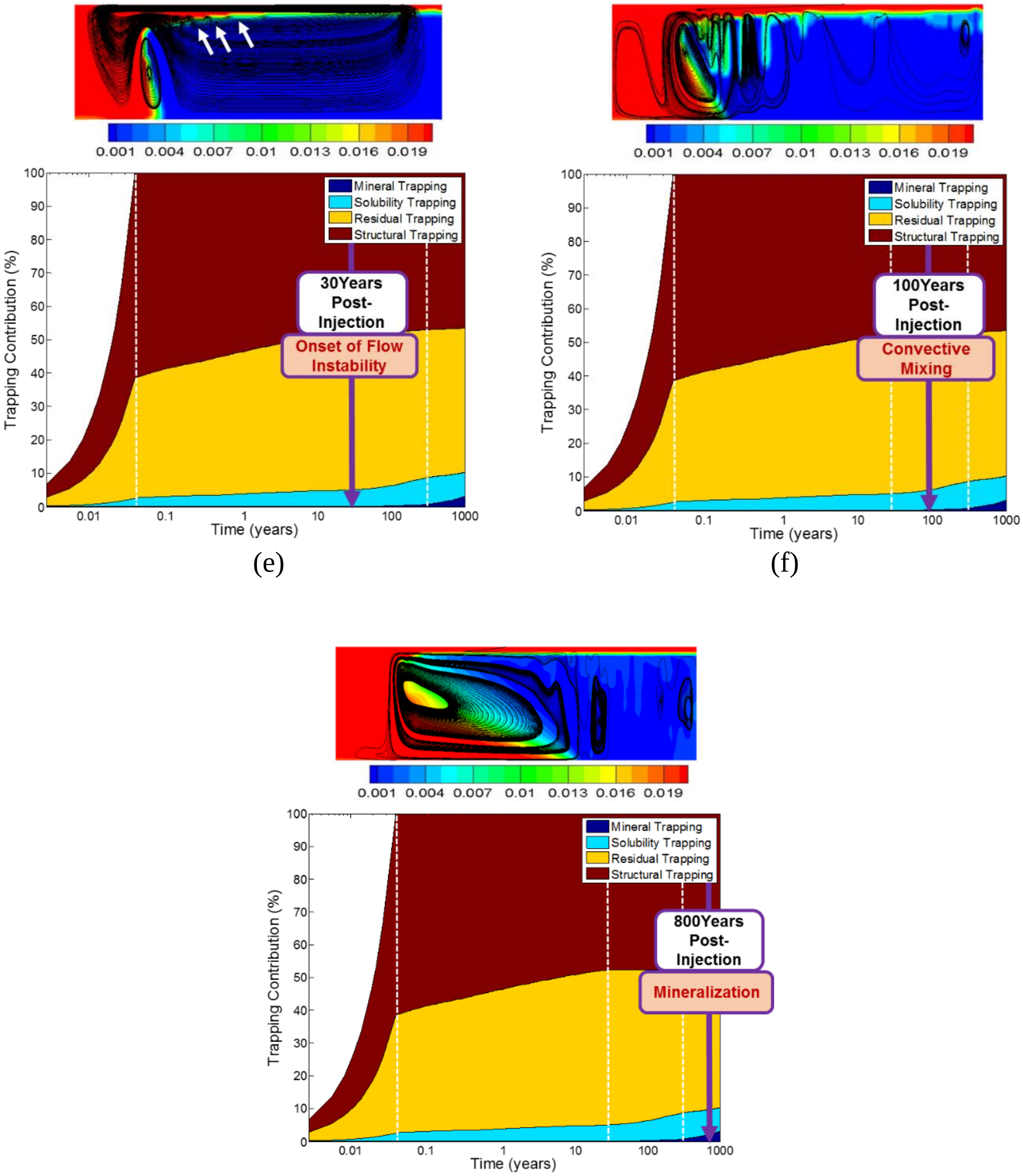

(e) (f)

(g)

Figure 2.20 (continued): Flow visualizations before and after CO2 injector shut-in shown in **Figs. 2.(e)** and **(f)**. Again, from the trapping contributions plot, CO2 dissolution trapping mechanism become dominant here. Studies on the convective fingering phenomenon, utilizing both numerical and experimental approaches, have been extensively reported (Neufeld et al., 2010; Pau et al., 2010; Riaz et al., 2006). The time to onset of flow instability as well as the size of the gravity fingers, is largely dependent on the Rayleigh's number $Ra$, which is a dimensioinless ratio of gravity to diffusive forces. Large CO2 diffusion forces results in high $Ra$ values, which reduces the time towards convective mixing, and vice versa (Hidalgo and Carrera, 2009). In our implementation, we have ignored molecular diffusion effects for simplicity purposes. As a result, onset time to flow instability and consequently, dissolution trapping contribution may be under-estimated.

Finally, the slumping flow regime become important. This occurs at large time (in this case 800 years) as shown in **Fig. 2.(g)** to further enhance the dissolution trapping mechanism. As indicated by the streamlines which are mostly concentrated at the aqueous CO2 interface, the flow regime is also driven by gravity forces. Szulczewski et al. (2013) classified the different types of slumping flow regimes depending on the shape of the interface due to the interplay between gravity and diffusive forces. We obtained straight-line slumping regime in our application due to the underlying assumption of negligible diffusive fluxes.

### *2.5.3 Fluid Compressibility Effects*

The strengths of streamline based simulation and flow description in heterogeneous porous media have previously been exploited for CO2 sequestration modeling by few authors (Obi and Blunt, 2006; Qi et al., 2009). These streamline models were however built on the assumption of incompressible fluids, which may not be quite accurate for the CO2 rich phase. Aside the fact that ignoring compressibility effects may lead to inaccurate pressure buildup estimation in the aquifer, studies have clearly shown that compressibility effects have significant impact on the eventual size and shape of the CO2 plume during injection (Vilarrasa et al., 2010). A possible explanation for this is the non-linear relationship that exists between pressure, CO2 rich phase and the aqueous phase mass fraction of CO2. High pressures results in larger equilibrium concentration of CO2 in the aqueous phase, which in turn affect the system of mass balance equations which solves to give the pressure distribution. Therefore, since the 1D streamline grids are generated based on the total fluxes computed from the pressure distribution, disregarding compressibility effects becomes detrimental to realistic representation of the flow physics.

We illustrate this with two numerical experiments were conducted with separate boundary conditions using the 1D model. We have chosen the simple model so that buoyancy effects do not interfere with compressibility effects, however as we will show later using a field example, similar conclusions can be reached with 3D geologically realistic cases. For both cases, the initial formation pressure is $3000\,psi$ and, again a constant pressure boundary was maintained at the opposite end of the injection well to mimic and open reservoir boundary. The injection well was constrained at a constant pressure of $5500 psi$ for the first experiment, while CO2 was injected as a constant reservoir rate of $1.7 RB / D$.

The compressibility effects are presented for the BHP constrained and rate constrained cases in **Figs. 2.21 a**nd **2.22** respectively. For the constant injection BHP case, it is expected that the CO2 rich phase saturation shock front for the compressible case will be ahead of the case where compressibility is not considered. This is because compressibility acts here as an additional source where the flux divergence is positive. It also shows up as a higher grid pressure at locations where CO2 rich phase saturation is non zero as shown in **Fig. 2.21**. Higher surface rate injection therefore results for the compressible case, which imply higher infectivity and ultimately, larger storage capacity than the incompressible case. For the constant reservoir injection rate constraint experiment, the CO2 plume apparently migrates faster in the incompressible case at $1.5 days$ as shown in **Fig. 2.22**. This seems contradictory, but it turns out that the lag in the compressible case is due to the lower injection BHP at early time, during which compressibility acts as a local sink and pressure slowly builds up in the reservoir. Higher surface injection rate, and thus, high storage capacity is however achieved with the compressible case again in this experiment due to compressibility effects. Concretely, both experiments show that ignoring compressibility effects, as in previous streamline-based models, under-estimates the storage capacity by a factor of $15\%$.

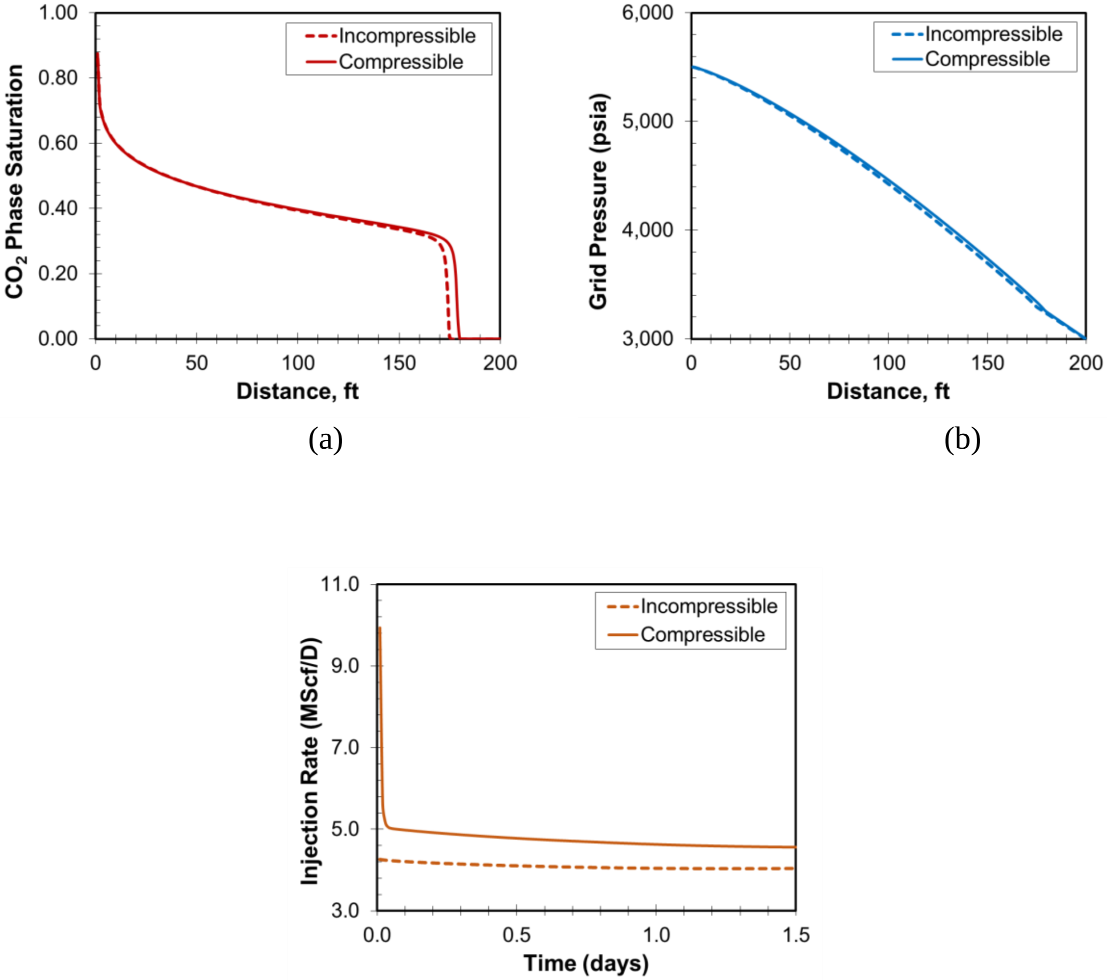

(a) (b)

(c)

Figure 2.21: Simulation responses for a constant injection pressure case showing (a) CO2 phase saturation profile, (b) cell pressure profile and (c) CO2 surface injection rate for the constant bottomhole pressure case

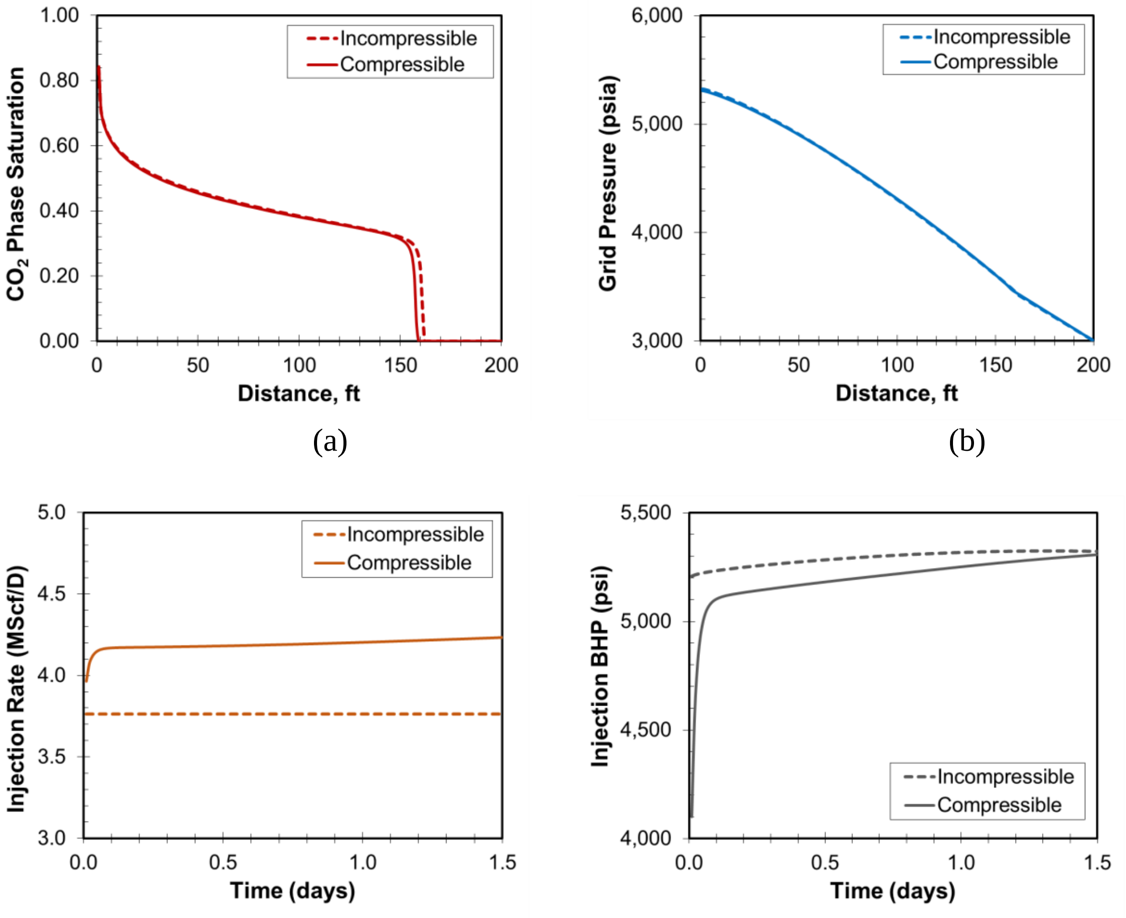

(a) (b)

(c) (d)

Figure 2.22: Simulation responses showing (a) CO2 phase saturation profile, (b) cell pressure profile, (c) CO2 surface injection rate and (d) Injector bottomhole pressure response for the constant subsurface volume injection rate case

### *2.5.4 Formation Dry-Out Effects*

On another note, formation dry out effects due to salt precipitation in the near injection well region, as shown by previous studies (Giorgis et al., 2007; Pruess and Müller, 2009), has significant negative influence on well infectivity over time. This poses a significant challenge to the overall operation of CO2 sequestration projects and as such, incorporating this effect in simulation models becomes important. Solubility calculations based on modified Redlich-Kwong equation of state (Spycher and Pruess, 2005) was included in the recent streamline model (Qi et al., 2009) but with more emphasis on the aqueous phase components, which turned out to ignore formation dry out effects. Besides that, solubility calculations were carried out after mapping convective transport solutions from the streamline domain onto the finite difference grids. This approach suffers from a smearing effect whereby component distribution between phases is more or less averaged over a set a grid cells as decided by the pressure update time step. This makes it difficult to fully capture formation dry out effects except with very frequent pressure updates. In our streamline based approach, mutual solubility calculations are carried out in tandem with convective transport before mapping to the grid. This ensures local precipitation effects are better captured without resorting to small time steps.

We demonstrate this effect by comparing the grid-based and streamline-based mutual solubility calculations with the homogeneous 2D cross section but under two different conditions: with and without capillary fluxes. For the case with capillary pressure we applied the van Genuchten type capillary pressure function (Van Genuchten, 1980) expressed as:

$$p_c = p_g - p_{aq} = p_0\left(\tilde{S}^{\left(\frac{n}{1-n}\right)} - 1\right)^{\frac{1}{n}}; \quad \tilde{S} = \frac{s_{aq} - s_{aq,c}}{1 - s_{aq,c}} \tag{2.48}$$

Where $s_{aq,c}$ denote aqueous phase connate saturation, $p_0 = 0.1$ and $n = 1.31$. All other conditions such as discretization, well locations and completions and injection rates are kept the same as described in the homogeneous 2D cross section example. Average solid saturation and permeability reductions in the injection grids are tracked for both cases over the simulation period of $10 days$. The results of this experiment are presented in **Figs. 2.23(a)** and **(b)** for cases without and with capillary effects respectively. The general trend is an increase in solid saturation and reduction in grid permeability due to salt precipitation. For the case without capillary effects, precipitation in the injection grid stops at 4days making solid saturation and grid permeability stay constant for the rest of the simulation period. At this point injection grids have effectively dried out with unit gas phase saturations. On the other hand under the influence of capillarity as in the second case, the injection grids do not dry out within the simulation time frame. This is because the strong water-wet nature of the rock causes more brine to be drawn to the injection grids as water continually gets vaporized into the CO2 rich phase. As a result, solid saturation increases while grid permeability reduces dramatically compared to the case without capillary effects. This is a reproduction of the effects previously studied by other authors (Giorgis et al., 2007; Kleinitz et al., 2003; Ott et al., 2015; Peysson et al., 2014) but with streamline based methods.

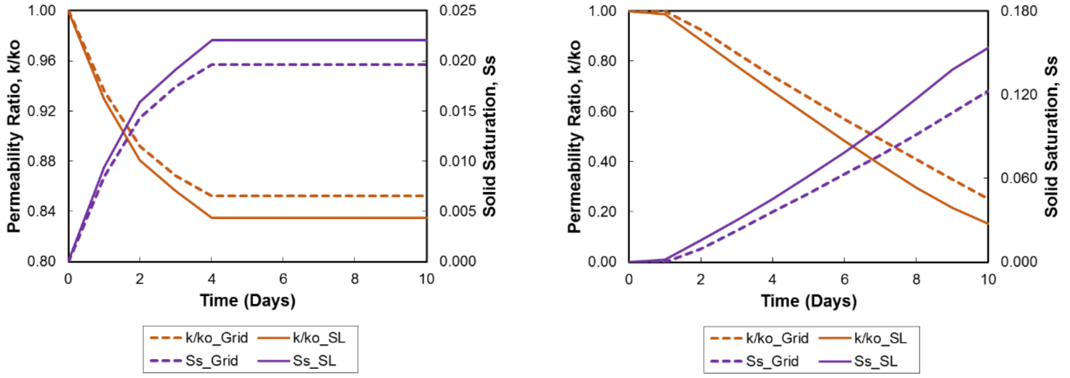

(a) (b)

Figure 2.23: Comparison of permeability and porosity changes obtained from grid-based and streamline-based mutual solubility calculation models (a) without capillarity and (b) with capillarity

Equally important is the observation from the comparison between grid-based and streamline-based mutual solubility calculations for both cases with and without capillary effects. The previously discussed smearing effect associated with the grid-based approach results in poor capture of the near well region precipitation phenomena. This is indicated as smaller increase in solid saturation and smaller reduction in grid permeability when the grid dries out. Without capillary forces, there are mild differences between the two solubility calculation approaches with about 10% and 2% differences in solid saturation and permeability reduction respectively. As formation get more and more water wet, the weakness of the grid-based approach in capturing the near well details get more significant with about 25% and 40% differences in solid saturation and permeability reduction respectively. Clearly such disparity in near well grid permeability results in differences in well injectivities which in turn can impact the evaluation of the aquifer storage potential and/or overall project viability.

## 2.6 Field Example: Johansen Case

### *2.6.1 Background on Field Model*

Finally we applied our streamline-based CO2 sequestration modeling approach to the Johansen field (Eigestad et al., 2009), one of the world's few aquifers considered for large scale storage of anthropogenic CO2. The Johansen formation, located offshore the Norwegian coast, was intended to serve two gas fired power plants in its vicinity having combined CO2 emissions of over 3Mt/year. The Johansen formation exists at depths between $7{,}200$ and $10{,}000\,ft$ below sea level, therefore with large overburden pressure which makes it suitable for CO2 Storage. The geological model indicates layers of sand and shale deposition with average thickness of over $300\,ft$.

A sector model of the field was publically made available with $100\times100\times11$ grid discretization with average cell dimensions of $1{,}500\times1{,}500\times70\,ft$. The Johansen sand is practically 'sandwiched' by the Dunlin shale in the top 5 grid layers and the Amundsen shale in the last grid layer. For the purpose of our simulations, we assume these shale zones are sealing and are therefore the respective simulation grids are considered inactive. **Fig. 2.24** presents the model structure and grid properties (ignoring shale layers) with permeability ranging between $64-1{,}660\,mD$ and porosity between $10-28\%$. The major fault existing in the middle of the formation is assumed to be sealing due to its large throw. All other faults in the formation are assumed to be sealing, and thus assigned zero transmissibility multipliers.

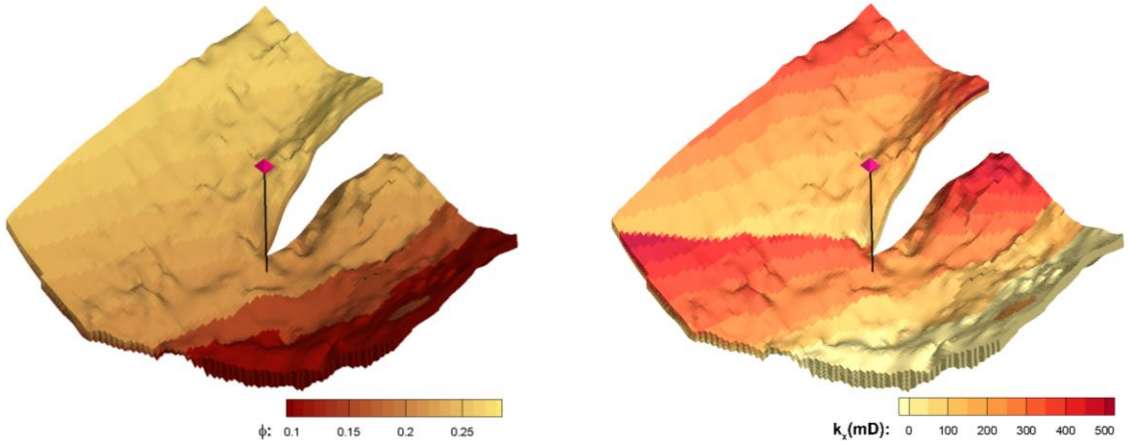

(a) (b)

Figure 2.24: (a) Grid porosity and (b) Logarithm of grid permeability distribution of Johansen model

### *2.6.2 Numerical Simulation Set-up*

The simulation model consists of a single well located in the center of the formation, similar to Eigestad et al. (2009). The well, assumed to connect to all 5 sand layers with a wellbore radius of $0.5\,ft$, injects supercritical CO2 at a rate of $483\,MMscf/D$ into the formation. This is equivalent to $29{,}000\,tons/day$ or $10\,Mtons/yr$. We applied a pore volume multiplier of $2{,}000$ in boundary cells to mimic a continuous aquifer. CO2 injection period lasted for $30{,}000$ days ($\approx 82$ years) and CO2 plume was monitored over a period of $2{,}000$ years post-injection.

A streamline based simulation model was conducted on the model with $1{,}000$ streamlines sufficient to span the domain. Pressure distribution shown in **Fig. 2.25(a)** indicate significant amount of pressure gradient (up to $2{,}000\,psia$) exists owing to large structural variations in the aquifer model. Streamline distribution at the end of the injection period is shown in **Fig. 2.25(b)** with the $\tau$ contoured along each streamline. Phase saturations and component mass fraction results from our streamline-based simulation approach was compared with the results from CO2STORE in **Fig. 2.26**. Again, good agreement was obtained between the two methods. Formation dry out effects are clearly noticeable, as indicated by unit CO2 rich phase saturations together with corresponding high aqueous phase salt concentration and low concentration of dissolved CO2 in the vicinity of the injection well. CO2 injector BHP also shows good agreement with the commercial simulator as shown in **Fig. 2.**.

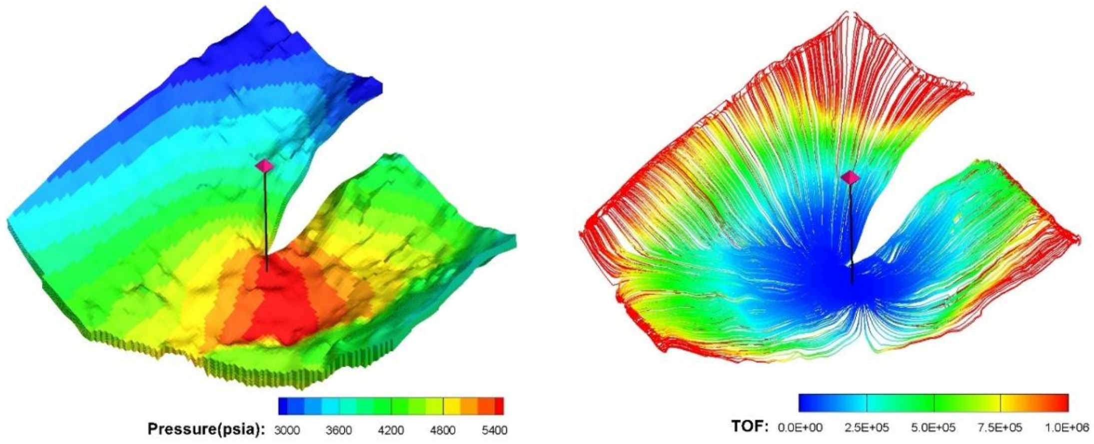

(b) (b)

Figure 2.25: (a) Grid pressure and (b) Streamline distribution with time of flight contours at Injector shut-in

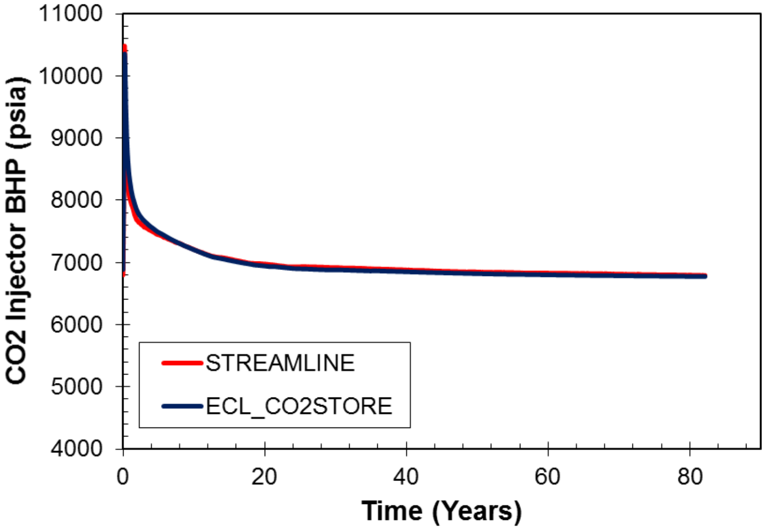

Figure 2.26: CO2 Injector BHP comparison between streamline-based simulation and CO2STORE for Johansen case

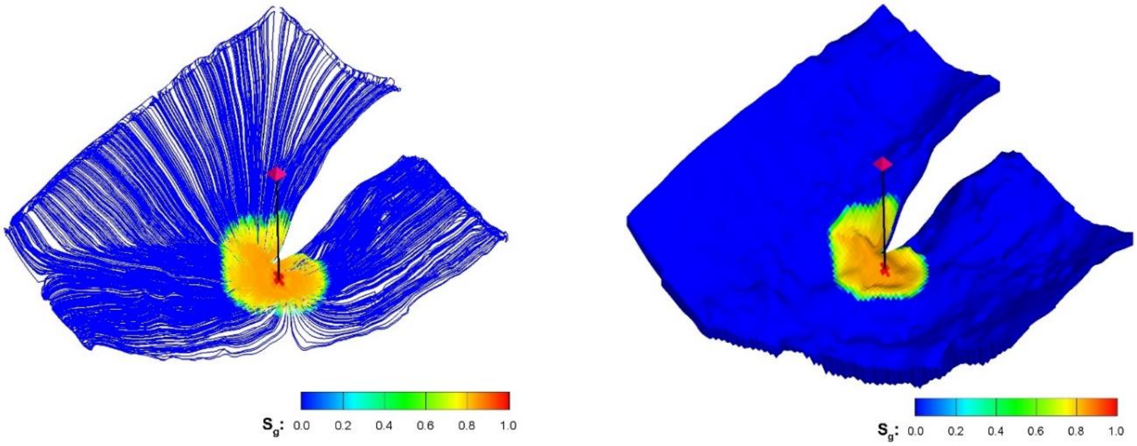

(a) (b)

Figure 2.27: CO2 rich phase saturation from (a) streamline and (b) CO2STORE

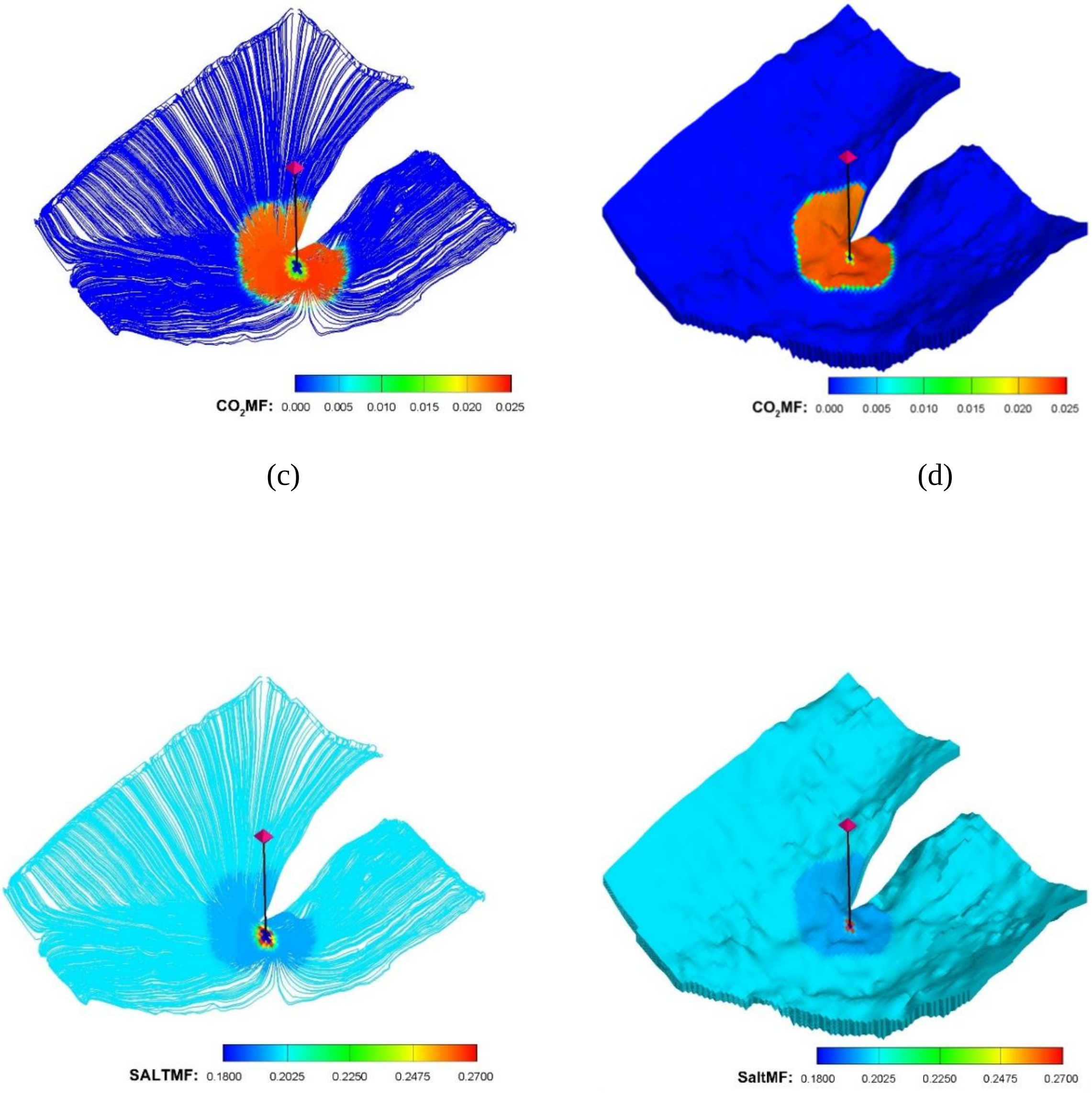

(c) (d)

(e) (f)

Figure 2.27 (Continued): Aqueous phase CO2 mass fraction from (c) streamline and (d) CO2STORE; aqueous phase salt mass fraction from (e) streamline and (f) CO2STORE

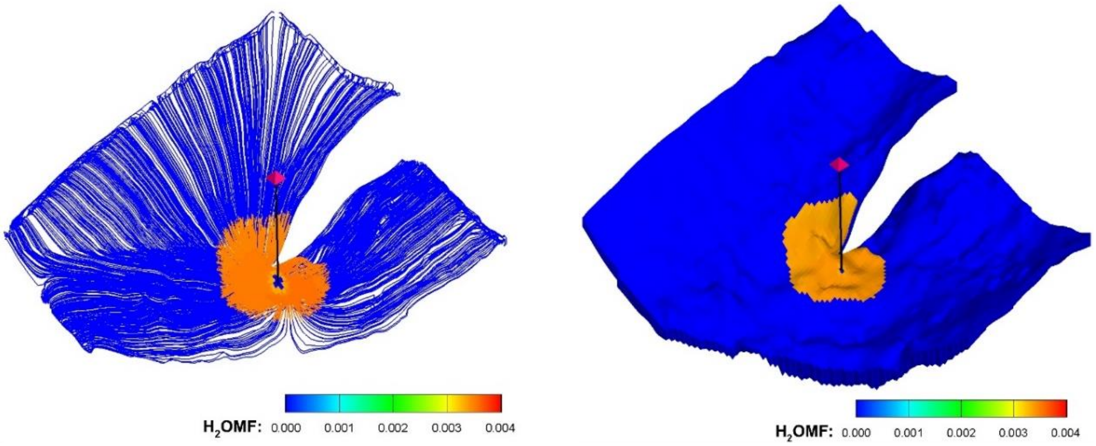

(g) (h)

Figure 2.27 (Continued): Water mass fraction in the CO2 rich phase from (g) streamline and (h) CO2STORE at the end of gas injection

### *2.6.3 Fluid Compressibility Effects*

Again, fluid compressibility effect was replicated for the Johansen case. Here CO2 injection was constrained at a constant bottomhole pressure value of $6000\,psia$ over an injection period of $80\,years$. In **Fig. 2.28(a)**, we overlay plots of five saturation contours each for both compressible and incompressible cases on the finite difference grid. It turns out, consonant with the 1D pressure constrained injection case presented in Fig. , that the incompressible saturation front mostly lags the compressible one. Similar explanation suffices for this observation. During injection fluid compressibility effects acts as a pseudosink since flow divergence in the vicinity of the injection well becomes less than zero. As a result, larger fluid volumes at surface and reservoir conditions invade the reservoir, as confirmed with the surface injection rate plots in **Fig. 2.21**.

In addition however, for realistic fully 3D models where gravity override is important, fluid compressibility play a significant role in plume migration at the lead edge of the CO2 plume directly beneath an impermeable seal. Therefore putting it all in context, ignoring fluid compressibility effects in streamline simulation of CO2 injection in saline aquifers results in under-estimation of the extend of plume migration during CO2 injection. Also, in agreement with the estimate made for the 1D simulation case, approximately 15% reduction in aquifer storage capacity results from ignoring fluid compressibility effects.

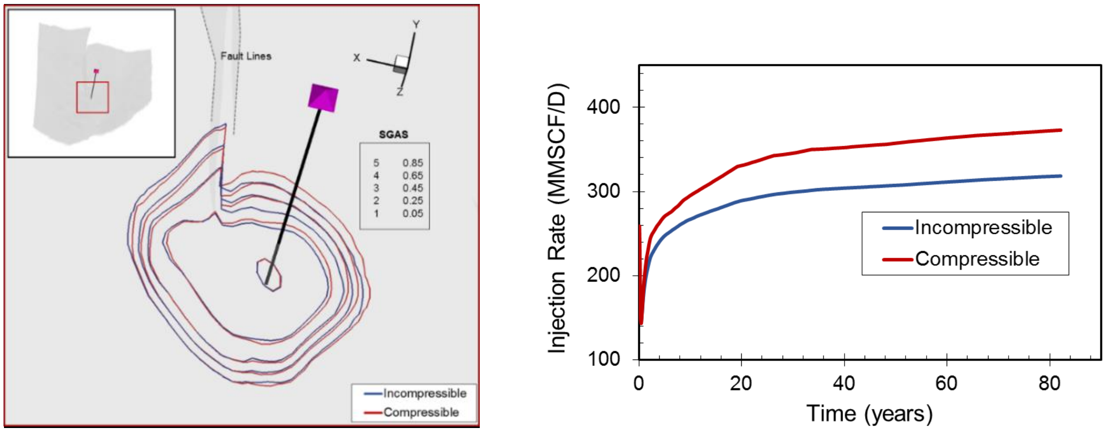

(a) (b)

Figure 2.28: Plots showing fluid compressibility effects with respect to (a) CO2 plume migration and (b) surface injection rate of CO2

### *2.6.4 Life Cycle of CO2*

The post injection period is characterized by upwards migration of CO2 plume under the influence of gravity forces, in the process of which more residual CO2 is trapped as shown in the life cycle plot in **Fig. 2.29**. A closer look at the CO2 rich phase saturation profile at 2,000years post-injection in **Fig. 2.30(a)** reveals structural trapping whereby pools of CO2 rich phase are immobilized at saturations higher than residual saturation values due to the geometry of the surface the sealing caprock. Note that the amount of structurally trapped CO2 due to seal undulations (Juanes et al., 2010; Nilsen et al., 2015) is included in the quantity of free CO2 plotted in **Fig. 2.29** and not specifically quantified. Assuming these caprocks are perfectly sealing, the structurally trapped pools of CO2 gradually reduce in size due to convective mixing that is generated over time.

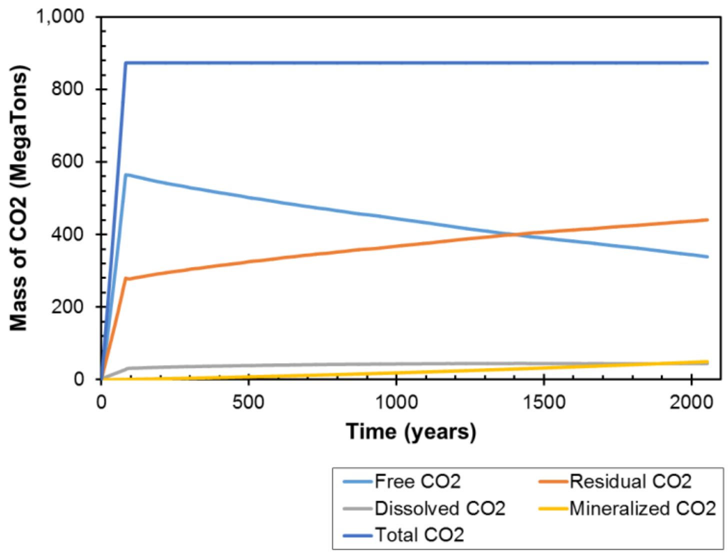

Figure 2.29: CO2 Life cycle for the Johansen case

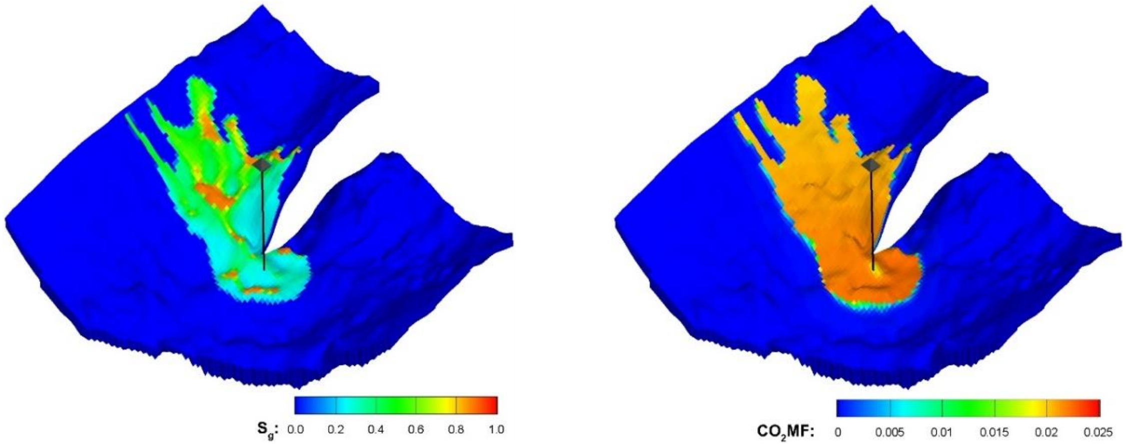

(a) (b)

Figure 2.30: (a) CO2 rich phase saturation and (b) Aqueous phase CO2 mass fraction at 2000 years post-injection

## 2.7 Concluding Remarks

A streamline-based simulation approach for CO2 sequestration in saline aquifers has been presented. The approach improves on previous streamline models to account for pertinent physics which are vital for reliable prediction of the multiphase flow during CO2 storage process. Our method is based on an iterative IMPES scheme in which fluid properties, phase saturations and component concentrations are updated in each global iteration until a specified tolerance limit is reached. In each global iteration, phase and component transport equations are solved along streamlines and corrected for transverse fluxes on the underlying grid.

Our approach elegantly captures the effect of fluid and rock compressibility along streamlines as an extra source in each streamline segments. This development over previous streamline models helps to improve on the pressure calculations resulting in superior equilibrium calculations. Furthermore, compared to previous streamline models, formation dry out effects are better modelled in our approach. This is because mutual solubility computations were carried out along streamlines unlike in previous streamline-based methods. This enables more accurate prediction of well injectivity variations during CO2 injection especially for highly water wet media. These are evident in the series of examples presented in this chapter where the results of our streamline-based simulation compare reasonably well with commercial simulator (ECLIPSE-CO2STORE) results.

In this chapter we demonstrate the solution approach to a reactive transport problem by decoupling the Multiphysics into a series of partial differential equations described in section ***2.2.1***, which are sequentially solved in a iterative fashion. It is clear, based on the results obtained from the cases presented that the impact of the nonlinearities associated with the multiphase-multicomponent problem can be reasonably relaxed using our approach, resulting in fewer amount of time steps required for modeling the CO2 injection period. We however submit that the computational advantage achievable using this approach may reduce as transverse fluxes such as gravity, capillarity and molecular diffusion become more dominant.

# CHAPTER III

# MULTIRESOLUTION GRID CONNECTIVITY-BASED REPARAMETERIZATION FOR EFFECTIVE SUBSURFACE MODEL CALIBRATION[1]

Low-rank representation of reservoir property fields has evolved over the years and offered significant benefits for robust subsurface model calibration problems. In particular, the Grid Connectivity-based (GCT) parameterization techniques provide a framework for efficient updates of high resolution models while preserving essential geologic features. For many subsurface flow problems, high fluxes are localized in the model and the normal GCT scheme struggles to effectively resolve the associated high-resolution model properties, because of the inherent smoothing effects. We propose a Multi-Resolution Grid Connectivity Transform (M-GCT) to address this shortcoming. In this parameterization scheme, the basis functions utilized for field property parameterization are constructed from adaptively coarsened grids which are based on the total fluid flux distribution in the model. The M-GCT basis functions display improved image compression within the Area of Interest (AOI) compared to the normal GCT scheme. The power and utility of the M-GCT scheme is demonstrated using a series of numerical experiments with 2D models and a field scale reservoir model.

---

[1] Part of the data reported in this chapter is reprinted with permission from "Post-Combustion CO2 EOR Development in a Mature Oil Field: Model Calibration Using a Hierarchical Approach" by Olalotiti-Lawal, F., Onishi, T., Datta-Gupta, A. et al. 2017: Paper SPE-187116-MS presented at the SPE Annual Technical Conference and Exhibition, San Antonio, Texas, USA. Copyright 2017 Society of Petroleum Engineers.

## 3.1 Introduction

Understanding subsurface flow mechanisms is crucial for reliable performance predictions, and therefore remains critical in many areas of subsurface engineering including ground water modeling and hydrocarbon reservoir engineering. Subsurface fluid flow dynamics is sensitive to model features including the geology (stratigraphy, depositional settings, existence of faults and conductive fractures), fluid type (single/multiphase/multi-component, compressible/incompressible), wettability (relative permeability and capillary pressure), and so on. These features are reasonably captured through geostatistical techniques and integrated subsurface modeling (Deutsch and Journel, 1992; Ertekin et al., 2001) which utilizes multiple data sources such as seismic, well logs and laboratory measurements in initial model building. It is however necessary that reservoir models be regularly calibrated at later times by integrating newly acquired dynamic data, including multiphase production, injection and 4D seismic data. Updated hydrocarbon reservoir models provide better understanding of the subsurface and hence, enable informed operational and investment decisions over the life of the asset. Fundamentally this task, often referred as model calibration or history matching, requires careful identification and estimation of critical parameters such as hydraulic conductivity (permeability) which impacts subsurface fluid flow.

Subsurface model calibration problems are inherently ill-posed (Oliver et al., 2008), which is a direct consequence of the under-determined nature of the problems. In other words, there are typically more model parameters than there are conditioning data. As such, the solution is non-unique and requires regularization in the form of smoothing of anchoring to prior information (Tarantola, 2005; Vasco et al., 1999). Assisted history matching techniques have shown great potential in addressing the challenges with the inverse problems related to subsurface model calibration. Most widely used are gradient-based techniques such as the adjoint method which utilizes the adjoint gradients computed in tandem with the forward numerical simulation run. These gradients, which represent the derivatives of production data misfit with respect to model parameters, are passed to standard optimizers the minimize data misfits. Streamline-based inversion techniques (He et al., 2002; Vasco et al., 1999) have also been introduced for convection-dominant flow regimes. This technique not only computes sensitivities more efficiently compared to the adjoint-based method, but also benefits from the quasi-linear attribute of the streamline-based inversion problem. Apart from deterministic approaches to subsurface model calibration, gradient-free and stochastic approaches are also widespread. Rapid growth in computing technology has enabled the application of evolutionary and stochastic algorithms such as Genetic Algorithms (Oliver and Chen, 2011; Schulze-Riegert et al., 2002), Particle Swarm Optimization (Mohamed et al., 2010), Markov Chain Monte Carlo (MCMC) (Ma et al., 2008; Maucec et al., 2007; Olalotiti-Lawal, 2013) algorithms to subsurface model calibration problems. However, these methods are limited in the number of parameters they can handle. Model reparameterization is therefore necessary to significantly reduce the parameter space and, thus better pose the subsurface model calibration problems. This is the primary motivation of this chapter.

By casting the grid property of interest, such as reservoir permeability of hydraulic conductivity on a system of orthogonal basis functions, the property field can typically be reconstructed as a linear combination of only a small number of these functions. Since the basis coefficients are uncorrelated, the low rank approaches for property representation become attractive for spatial model calibration problems. Existing parameterization techniques differ by the basis construction as well as the basis combination procedures. The Karhunen-Leove Transform (Karhunen, 1947; Loeve, 1978) also known as the Principal Component Analysis (PCA) relies on the Gaussian process assumption for grid properties and the basis functions are eigenvectors resulting from the Singular Value Decomposition (SVD) of the property covariance matrix. Due to the rapid decay of corresponding eigenvalues, only a small number of the basis functions are needed in a history matching problem as illustrated by several authors (Ma et al., 2008; Sarma et al., 2008a; Sarma et al., 2008b). A major shortcoming for the PCA is that parameter covariance matrices are usually not readily available and difficult to construct with spatially sparse data which is typical for petroleum reservoirs. Moreover, the underlying Gaussian assumption limits its applicability to spatial parameter distributions in the presence of connectivity of extreme values, for example, high permeability channels and low permeability barriers (Journel and Alabert, 1990).

Then application of the Discrete Cosine Transforms (DCT) (Strang, 1999) was proposed to address the limitations of the PCA method (Jafarpour and McLaughlin, 2008). Bhark et al. (2011a) later proposed a generalization of the DCT re-parameterization approach, referred to as the Grid Connectivity Transform (GCT) to handle a broad range of reservoir grids (structured, corner point and unstructured grids). In the GCT approach, basis functions are obtained as the eigenvector of the grid Laplacian which considers only the reservoir grid connectivity information in a sparse matrix. For the purpose of parameter update, a linear combination of the basis functions generates a multiplier field with which the property field is updated by individual grid property-based Schur product operation. The parameterization technique has found application in various history matching workflows, both deterministic and probabilistic (Olalotiti-Lawal and Datta-Gupta, 2015; Park et al., 2015). Multiplier fields are typically smooth, since they are generated with a small number of lower frequency (high energy) basis functions. However, for reservoir models with significant small-scale variations of flux field, such as high well density reservoirs, relatively larger number of basis functions are typically required to reasonably capture underlying high frequency flux profiles. This is particularly the case for gas ($CO_2$) injection processes flow distributions are generally more sensitive to local contrasts in hydraulic conductivity properties, because of typical unfavorable mobility ratios.

We propose a variant of the GCT designed to incorporate additional resolution locally within the reservoir domain in the parameterization procedure. By coarsening the low flux regions of the model, while retaining the original resolution of the high activity (flux) regions, otherwise referred to as the Area of interest (AOI) our proposed approach results in improved resolution with better image compression within the AOI. This parameterization scheme is derived from an adaptive JPEG image compression algorithm and generalized for reservoir model grid systems. In the adaptive digital image compression procedure, the image undergoes a quadtree decomposition (De Natale et al., 1992; Samet, 1984) which compromises unstructured sub-images. Particularly in the edge-adaptive compression technique (Ramos and Hemami, 1996), the size (pixel count) of each sub-image depends on the level of visual activity, as determined by the proportion of edges identified by an edge detection algorithm. Consequently, critical details of the image are better preserved with the same memory overhead as with the traditional JPEG routine. As an analogy to reservoir property field parameterization, regions of high visual activity symbolize high flux regions of the field in within which high frequency update might be required for improved and more efficient model calibration.

In this work, a Multi-Resolution Grid Connectivity Transform (M-GCT) is proposed, in which the basis construction relies on prior dynamic information, such as well distribution, in the reservoir model. The objective of this study is to investigate the potential benefits and possible limitations of the M-GCT in the context of subsurface model calibration. This chapter is organized as follows: First, the comparative performances of the normal and M-GCT parameterization schemes are discussed and compared. Second, a series of 2D numerical experiments, utilizing a layer of the SPE10 comparative model (Christie and Blunt, 2001), are conducted to investigate the power and utility of the M-GCT compared with the Normal GCT scheme for subsurface model calibration. Similar experiments are conducted with the Brugge benchmark model (Peters et al., 2010) to validate the applicability and robustness of the M-GCT scheme at the field scale. Our results clearly demonstrate the advantage of the M-GCT parameterization scheme in terms of improved localized parameter resolution and data compression leading to superior subsurface model updates.

## 3.2 Grid Connectivity-Based Reparameterization

One of the key objectives in subsurface model parameterization is to represent reservoir property continuity with few uncorrelated parameters. This approach minimizes parameter redundancies in reservoir description and hence, facilitates stability of the model calibration problem. As a generalization of the concept of Discrete Cosine Transform (DCT) for image compression (Jafarpour and McLaughlin, 2008; Strang, 1999), the Grid Connectivity Transform (GCT) was proposed to effectively handle complex geologic grid geometry and structures (Bhark et al., 2011a). In GCT, geologic model features such as faults, pinch outs and inactive cells in structured, corner point and unstructured grid framework are accounted for in the construction of the grid Laplacian. A singular value decomposition of the Laplacian provides a set of basis functions which are utilized in updating reservoir property field at scales and resolution required by the observed data (Bhark, 2011).

A notable advantage of the GCT over other parameterization methods is its reliance only on the grid connectivity information for the construction of the Laplacian matrix. The steps in the construction of the Laplacian matrix $\mathbf{L}$ involves translating the reservoir model containing $N$ grid cells to an undirected graph $G = (V, E)$ with the grid nodes represented by a set of $N$ vertices $V$ and connections between the grid cell represented by a set of edges $E$. Then an $N \times N$ symmetric adjacency matrix $\mathbf{A}$ is constructed with elements $a_{ij}$ as follows:

$$a_{ij} = \begin{cases} 1 & if\,(i,j) \in E \\ 0 & if\,(i,j) \notin E \end{cases} \tag{3.1}$$

In other words, the overall graph connectivity structure is encoded in the adjacency matrix $\mathbf{A}$. Finally, the graph Laplacian is obtained as $\mathbf{L} = \mathbf{D} - \mathbf{A}$, where $\mathbf{D}$ is an $N \times N$ diagonal matrix whose diagonal entries are defined as the row-wise sum of the elements of $\mathbf{A}$. As an illustration, **Fig. 3.1** shows a $10 \times 10$ structured grid with the graph Laplacian constructed from the corresponding graph of order $N = 100$. As indicated by the annotations on the grid figure, the grid Laplacian is constructed based on only the grid cells connection information.

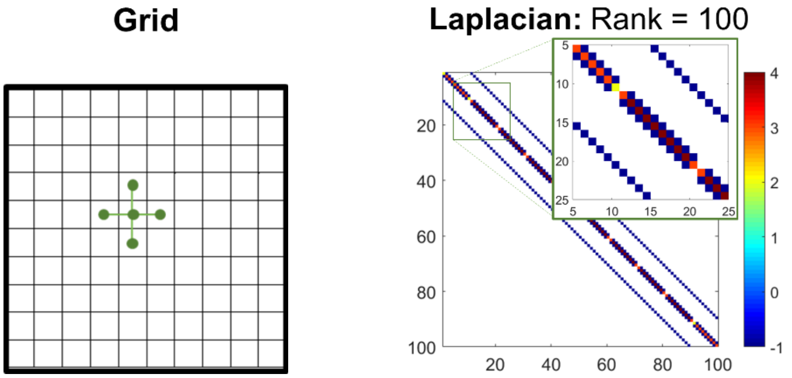

(a) (b)

Figure 3.1: An illustrative 10x10 grid with the corresponding connectivity Laplacian based on the grid connectivity information. Grid Laplacian for the 2D model is penta-diagonal having rank equal to the number of gird cells

Grid Laplacians constructed in such manner are typically banded for structured grids. For unstructured and complex reservoir grids involving Non-Neighbor Connections (NNCs) because of faults and pinch-outs, grid Laplacians may not be strictly banded depending on the level of structural complexity of the grids. Nonetheless, grid Laplacians are generally very sparse and this is beneficial computationally for spectral decomposition in the generation of the basis functions, which are basically the eigenvectors of the grid Laplacian. For all computations reported in this work, we utilize the ARPACK library (Lehoucq et al., 1998), in-built in MATLAB (Mathworks, 2016) for eigenvalue decomposition. The package contains an implementation of an efficient iterative eigen-problem solver which exploits the sparse and symmetric nature of the grid Laplacian in each Lanczos iteration for improved computational cost (Trefethen and Bau III, 1997).

The subset of the basis functions $\Phi_i$ obtained for the grid Laplacian shown in **Fig. 3.1** are shown in **Fig. 3.2**, arranged in the order of increasing frequency. The basis functions are essentially the modal vibrational harmonics based on the grid connectivity structure (Bhark, 2011). Any grid property field $\mathbf{u} \in \mathbb{R}^N$ can be represented as a linear combination of the basis functions given by:

$$\mathbf{u} = \sum_{i=1}^{m} v_i \Phi_i \equiv \Phi \mathbf{v} \tag{3.2}$$

Where $m \leq N$. A useful property of the basis vectors is their orthogonality, i.e. $\Phi^T \Phi = \mathbf{I}$. This allows seamless transition between real (on the left) and spectral representations (on the right) of grid property fields

$$\mathbf{u} = \Phi\mathbf{v} \Leftrightarrow \mathbf{v} = \Phi^T\mathbf{u} \tag{3.3}$$

Further improvement on the compression power of the GCT is achieved by preferential selection of the basis functions as guided by the prior property field, if available. This adaptive GCT approach entails projecting the prior model to the frequency domain comprising a sufficient number of basis functions. Basis function are then selected according to the sorting indices (in descending order) of the absolute values of the resulting basis coefficients $\mathbf{v}$ which are obtained from the spectral transformation described by **Eq. 3.3**. Finally, using the basis functions are the building blocks, it is possible to re-construct the property field with few number of uncorrelated parameters as desired using the following expression:

$$\mathbf{u}_{estimate} = \Phi\,\Phi^T\mathbf{u} \tag{3.4}$$

For the rest of this chapter, we shall refer to the image compression algorithm describe so far as the Normal GCT algorithm. This method is general and robust in terms of compliance to multiple reservoir grid types and wide applicability to reservoir parameter field estimation. However, parsimonious selection of basis functions improves smoothing effects that result in loss of localized features. For instance, in a subsurface model calibration problem where production wells are clustered in a relatively smaller area of the reservoir domain, the Normal GCT parameterization approach will effectively require large number of basis functions to adequately resolve the flow field to achieve reasonable match of the production data. Our proposed Multi-Resolution Grid Connectivity Transform (M-GCT) algorithm addresses this shortcoming by introducing improved localized resolution.

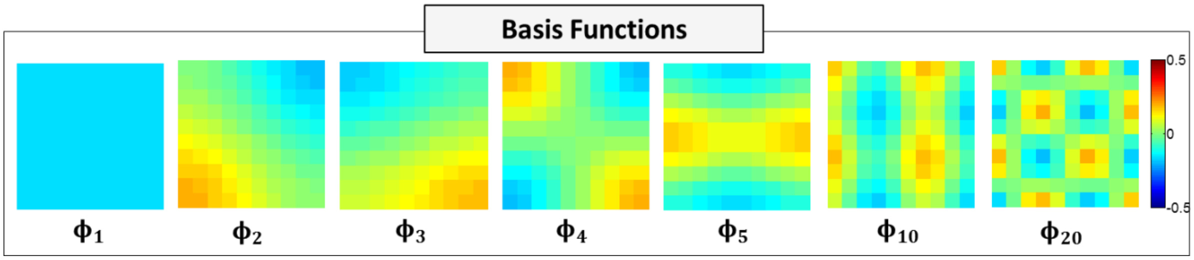

Figure 3.2: A set of basis orthonormal functions obtained from the eigen-decomposition of the grid Laplacian based on Normal GCT parameterization

## 3.3 Multi-Resolution Grid Connectivity Transform (M-GCT)

Although it is of interest to obtain a global update of reservoir properties, dynamic data are rarely acquired at similar spatial resolution throughout the entire reservoir domain. This can be seen in the Brugge benchmark model in which the wells are clustered around the anticline region of the formation above the oil-water contact **Fig. 3.3(a)**. As shown in **Fig. 3.3(b)**, the region of high well density is characterized by much higher flux magnitude than the other areas. We refer to the high flux region of the field as the Area of Interest (AOI) since more dynamic data are available in this region compared to other regions. It is natural to parameterize the reservoir properties such that AOI is better resolved during the model calibration procedure. This is the idea behind the M-GCT parameterization method.

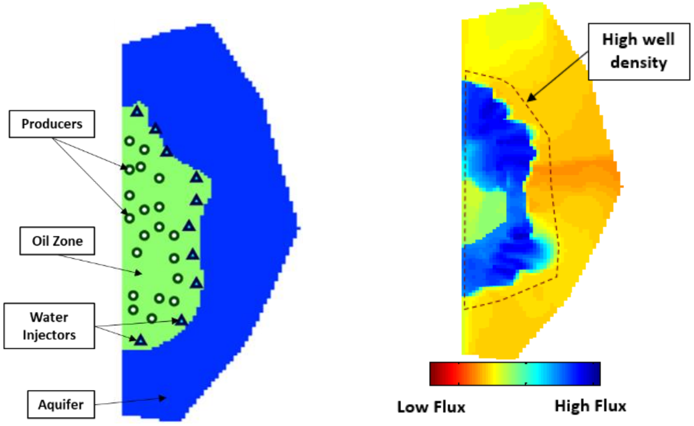

(a) (b)

Figure 3.3: Areal views of the Brugge model showing (a) Fluid contacts and well distribution and (b) Flux distribution in reservoir

In the M-GCT method, reservoir grid cells in regions outside the AOI are coarsened while the AOI is left at native fine grid resolution. This is illustrated in **Fig.** 3.4**(a)** which shows the same grid in **Fig.** 3.1**(a)**, coarsened in the area outside the AOI. Considering the connectivity information in the grid system, the grid Laplacian can be constructed as discussed in the last section. As shown in **Fig.** 3.4**(b),** the grid Laplacian is no longer banded as there are multiple fine grid cell connections to a single coarse grid cell at the boundary of the AOI. It is apparent that the grid Laplacian gets less banded with more aggressive coarsening of the grid cells outside the AOI.

The M-GCT leads to reduced computational cost for the eigen-decomposition of the grid Laplacian. The computational complexity of eigen-value problems scales by $O(N^{\varepsilon})$ where $N$ denotes the rank of the matrix and $2.0 < \varepsilon < 3.0$, depending the algorithmic efficiency (Trefethen and Bau III, 1997). The reduced rank of the grid Laplacian in **Fig.** 3.4**(b)** results in substantial reduction in computational cost for the eigenvalue problems.

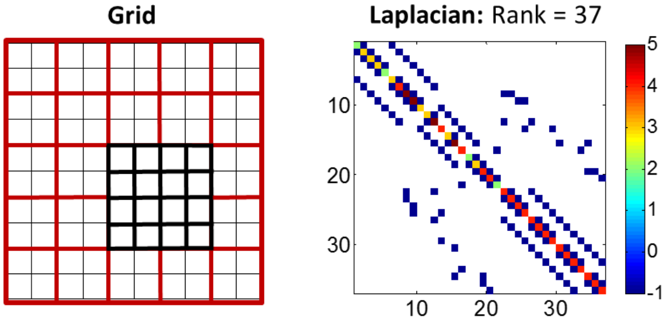

(a) (b)

Figure 3.4: An adaptively coarsened 10x10 grid with the corresponding connectivity Laplacian based on the Multi-Resolution Grid Connectivity Transformation (M-GCT). Grid Laplacian for the 2D model is less banded and has smaller rank compared to the full 10x10 grid problem

The basis functions derived from M-GCT, shown in **Fig.** 3.5, share similar properties with those obtained from the normal GCT method. In both methods, the first basis functions have constant values. This is an essential member of the set of basis functions since it allows for a bias correction or overall shift in the mean value of grid property. Also, the basis functions are orthonormal, allowing seamless spectral-real space transform of grid property field representation according to **Eq. 3.3**. Also, grid property field reconstruction with minimal number of basis functions is similar with both parameterization schemes, as described in **Eq. 3.4**. One unique feature of the set of basis functions derived from the M-GCT is their relatively higher frequency within the AOI. This feature enhances the image compression quality within the AOI, and hence, improved reservoir parameter resolution can be obtained by integrating localized dynamic data into the reservoir model.

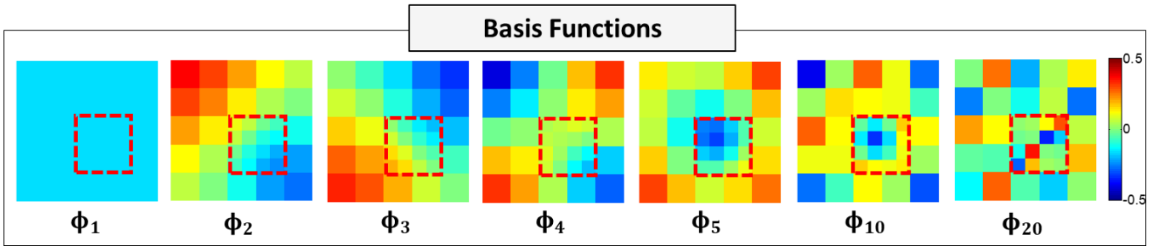

Figure 3.5: A set of basis orthonormal functions obtained from the eigen-decomposition of the grid Laplacian based on Multi-Resolution GCT parameterization

## 3.4 Comparative Compression Performance: GCT vs. M-GCT

We compare here the image compression capabilities of the normal GCT and M-GCT parameterization schemes. This is done by quantifying the error in the estimation of the grid property values. The property field is reconstructed with increasing number of basis functions using **Eq. 3.4** at each step. We carry out this exercise for two cases: (1) In a marine type depositional environment (relatively mild property heterogeneity) and (2) in a fluvial depositional environment (severe property heterogeneity). The average Root Mean Square (RMS) is computed as:

$$RMSE = \sqrt{\frac{\left(\ln(\mathbf{k}_{est}) - \ln(\mathbf{k})\right)^T \left(\ln(\mathbf{k}_{est}) - \ln(\mathbf{k})\right)}{N}} \tag{3.5}$$

Where $\mathbf{k}_{est}$ and $\mathbf{k}$ respectively denote the estimated and the reference property fields. For the first case involving mild contrast in property values, the relative performance of the normal GCT and M-GCT is visually compared using 100 leading basis functions in **Fig. 3.6** and quantitatively compared in **Fig. 3.7**. Note that we compared the M-GCT scheme at varying coarsening levels of the regions outside the AOI. It is clear from these figures the improvement in image compression achieved within the AOI using the M-GCT. However, the image compression quality deteriorates with more aggressive coarsening outside the AOI.

Similar trends can be identified in the second case involving sharp contrast in grid property values. Again, comparing the image reconstruction qualitatively in **Fig. 3.8** (with 100 leading basis functions) and quantitatively in **Fig. 3.9**, same conclusions can be drawn in terms of improvements in image compression quality within the AOI and reduction of the image compression quality outside the AOI with aggressive grid coarsening schemes. An interpretation of this trend is that while global uniformity in grid property resolution is ensured with the normal GCT, the M-GCT parameterization facilitates an improvement of grid property resolution within a defined AOI at the expense of the resolution outside the AOI. Of course, as shown from our analysis, the extent to which this is allowed depends on the level of grid coarsening outside the AOI during the Laplacian construction.

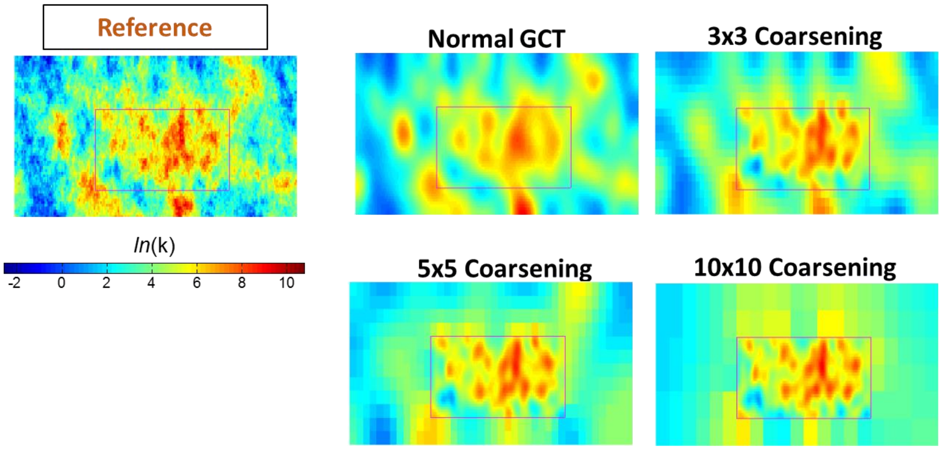

Figure 3.6: Picture compares image compression capabilities between Normal and Multi-Resolution GCT parameterization methods in a marine type depositional environment. M-GCT, compared at 3 different adaptive coarsening scales, clearly shows improved image compression over Normal GCT within the AOI

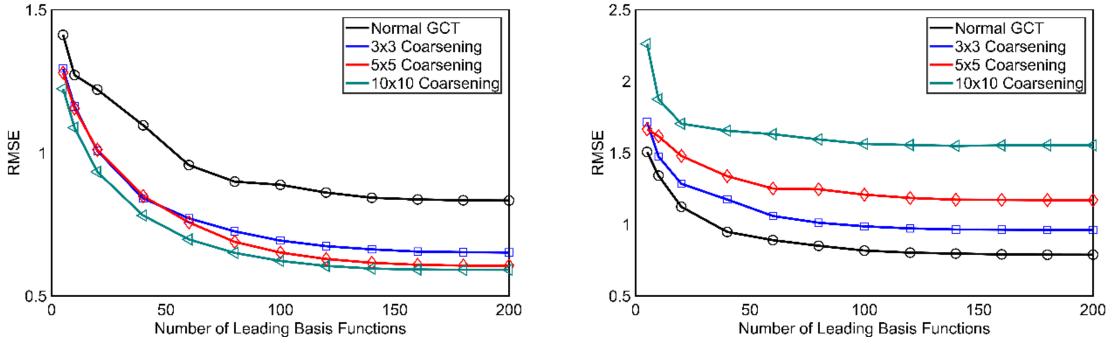

(a) (b)

Figure 3.7: Quantitative comparison of image compression performance between Normal and Multi-Resolution GCT parameterization methods in a marine type depositional environment (a) within the AOI and (b) outside the AOI. M-GCT, compared at 3 different adaptive coarsening scales, clearly shows increasing improvement in image compression with in the AOI and an associated deterioration of compression performance outside the AOI with more aggressive coarsening

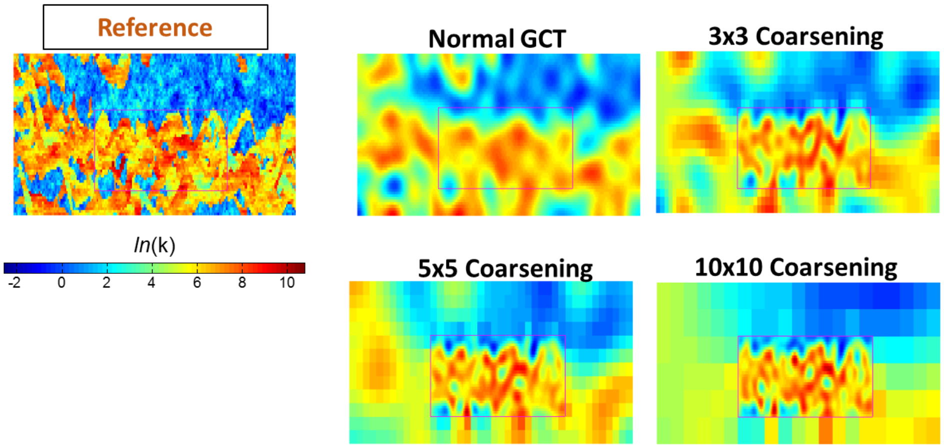

Figure 3.8: Picture compares image compression capabilities between Normal and Multi-Resolution GCT parameterization methods in a fluvial environment. M-GCT, compared at 3 different adaptive coarsening scales, clearly shows improved image compression over Normal GCT within the AOI

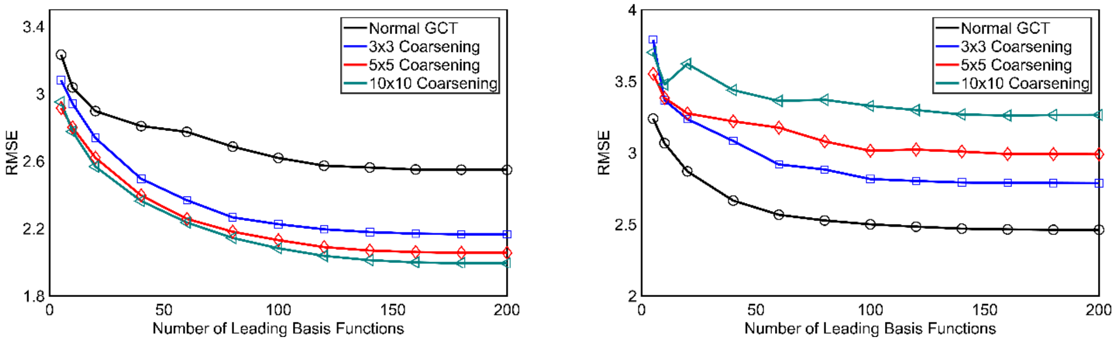

(a) (b)

Figure 3.9: Quantitative comparison of image compression performance between Normal and Multi-Resolution GCT parameterization methods in a fluvial depositional environment (a) within the AOI and (b) outside the AOI. M-GCT, compared at 3 different adaptive coarsening scales, clearly shows increasing improvement in image compression with in the AOI and an associated deterioration of compression performance outside the AOI with more aggressive coarsening

Regardless of the parameterization scheme adopted, the importance of the basis functions for image reconstruction diminish with increasing number of leading basis functions. This is evident in both cases considered as seen from the slower reduction in

RMSE shown in **Figs. 3.7, 3.9** and **3.10.** The observed trends can be attributed to the relatively higher frequency of basis functions within the AOI and relatively lower frequency of basis functions outside the AOI with the M-GCT scheme compared to the normal GCT scheme. In effect, the M-GCT parameterization can maximize the resolution available within the AOI and at the same time provide smooth estimate of the parameter values in regions outside the AOI. The benefit of this unique feature of the M-GCT will be demonstrated with numerical experiments pertaining to subsurface model calibration problems in the following sections.

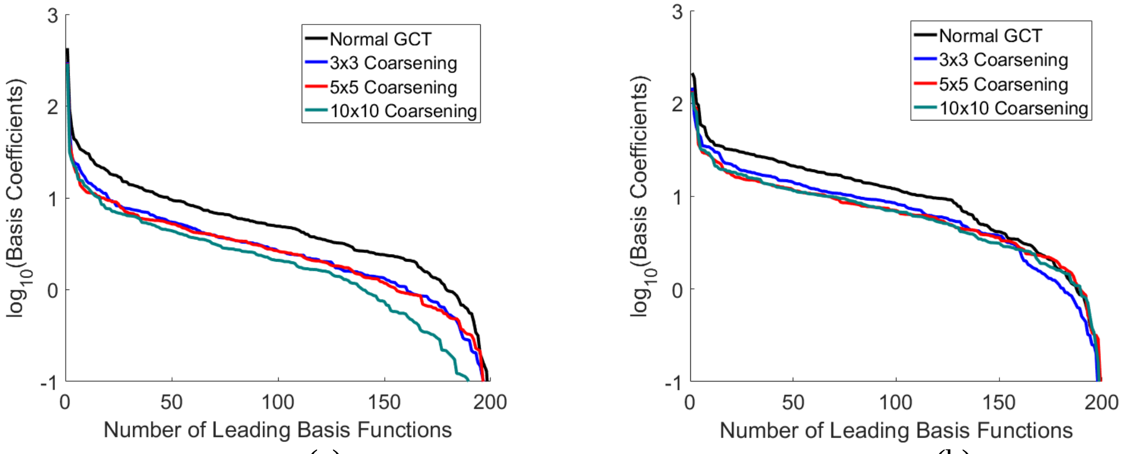

(a) (b)

Figure 3.10: Plots showing rapid drop in leading basis coefficients required for reconstructing the property fields in the (a) marine and (b) fluvial depositional environments. Plots show that smaller basis coefficients required to the property field reconstruction

## 3.5 Application to Model Calibration Problems

The key objective of the model reparameterization is to facilitate robust calibration of subsurface models through a low rank representation and update of property fields. In this manner large number of spatially correlated grid property values are reduced to a set of uncorrelated basis coefficients, $\mathbf{v}$ which are directly updated within the calibration workflow. Typical workflow involves evaluating each proposal of $\mathbf{v}$ using a reliable forward model and quantitatively comparing the model response with available dynamic data. Model calibration algorithms essentially seek to find an optimal set or multiple sets of $\mathbf{v}$ that reproduce the available dynamic data within a specified tolerance. We present the details of the forward model and inversion algorithm in the following sub-sections.

### *3.5.1 Forward Model*

Subsurface models are evaluated by solving a system of coupled partial differential equations to compute both pressure and fluid saturation distribution in the porous media and the production responses at wells. Forward models, regardless of the numerical scheme involved, seek to honor material balance within each grid cell by ensuring that mass is conserved at all locations and time (Aziz and Settari, 1979b):

$$\frac{\partial}{\partial t}\left(\frac{\phi s_\pi}{B_\pi}\right) = \nabla \bullet \left(\frac{\mathbf{k}\lambda_\pi}{B_\pi}\left(\nabla p_\pi - \gamma_\pi \nabla z\right)\right) + q_\pi \; ; \quad \pi \in \{w, n\} \tag{3.6}$$

Where the primary variables computed are the pressure $p_\pi$ and saturation $s_\pi$ distributions of both the wetting ($\pi = w$) and non-wetting ($\pi = n$) phases. Spatial distribution of porosity and permeability tensor, which are properties of the porous media, are denoted by $\phi$ and $\mathbf{k}$ respectively. The phase mobility $\lambda_\pi$ is the ratio of the phase relative permeability to the in-situ viscosity. The phase formation volume factor $B_\pi$ represents the ratio of the phase density at standard conditions to the phase density at subsurface conditions. Finally, well rates, either by reservoir injection or withdrawal are denoted by $q_\pi$. Additional physical constraints require the following:

$$\sum_\pi s_\pi = 1 \text{ and } p_w = p_n - P_C(s_w) \tag{3.7}$$

Where $P_C(s_w)$ is the capillary pressure. These systems of equations are either constrained by pressure or flux boundary conditions at the wells and/or at the outer boundaries of the solution domain. In all the examples reported here, we only update the field permeability distribution and assume all other parameters are known with reasonable level of certainty. We utilize ECLIPSE, a commercial finite difference flow simulator (Schlumberger, 2014) for all model evaluations in this study.

It is worth mentioning here that ECLIPSE provides a model grid coarsening functionality which allows model evaluations to be conducted more efficiently by reducing the effective cell count. This feature is particularly favorable for the M-GCT parameterization scheme in which regions outside the AOI can be adaptively coarsened during the basis construction. Computational cost required for each model evaluation, and overall for the entire model calibration workflow, is significantly reduced if the simulation model utilizes the same coarsening scheme used for the construction of the basis functions. With the transmissibility upscaling facility in ECLIPSE, the computational cost advantage generally comes with negligible loss of accuracy in model evaluations, more so that computational grids are only coarsened outside the AOI.

### *3.5.2 Inversion Workflow*

We adopt a gradient-based inversion workflow proposed by Bhark et al. (2011a) as shown in **Fig. 3.11**. The workflow starts with a fixed number of leading basis functions. Rather than directly altering the permeability field, a set of multiplier fields are updated during model calibration. The permeability field is updated by an elementwise Schur product of the logarithm of initial model permeability with the multiplier field. The multiplier field is constructed as a linear combination of the selected basis functions, $\Phi$ using a set of uncorrelated basis coefficient, $\mathbf{v}$. Mathematically,

$$\ln(\mathbf{k}(\mathbf{v})) = (\Phi\mathbf{v}) \circ \ln(\mathbf{k}_{init}) \tag{3.8}$$

Numerical simulations are conducted to obtain the model response based on the updated permeability field. In addition, adjoint gradients, which are essentially the multidimensional derivatives of the production data with respect to model permeability, are also obtained from each fully-implicit simulation run and associated adjoint solutions (Li et al., 2001). Objective function is computed as a weighted L2 norms of the mismatch between observed $\mathbf{d}_{obs}$ and simulation response $g(\mathbf{k}(\mathbf{v}))$ as follows:

$$J(\mathbf{v}) = \left\| \mathbf{d}_{obs} - g(\mathbf{k}(\mathbf{v})) \right\|_2^2 + \eta \left\| \ln(\mathbf{k}(\mathbf{v})) - \ln(\mathbf{k}_{init}) \right\|_2^2 \tag{3.9}$$

Where $\eta$ represents a regularization term to prevent large deviations between the updated and prior permeability model to maintain geologic realism during the model updates.

Large values of $\eta$ indicate high level of confidence in the initial geologic mode and only minor updates are allowed. As a result the inversion results can be sensitive to the value of $\eta$. Although the choice of values for $\eta$ can be subjective, there are guidelines for this in literature (Parker, 1994). In situations where good estimates exist for measurement error variance or covariance matrix, **Eq. 3.9** can be generalized accordingly (Bhark, 2011; Tarantola, 2005). From **Eqs. 3.8** and **3.9**, and by chain rule, the gradient of the objective function can be computed as:

$$\frac{\partial J(\mathbf{v})}{\partial \mathbf{v}} = 2\left[\left(\mathbf{d}_{obs} - g(\mathbf{k}(\mathbf{v}))\right)^T \frac{\partial g(\mathbf{k}(\mathbf{v}))}{\partial \mathbf{k}} diag(\mathbf{k}(\mathbf{v})) + \eta\left(\ln(\mathbf{k}(\mathbf{v})) - \ln(\mathbf{k}_{init})\right)^T\right] diag(\ln(\mathbf{k}_{init}))\Phi \tag{3.10}$$

Note that the gradient is computed by utilizing the chain rule, so that the quantity within the square parenthesis represent the first part of the objective function derivative, that is $(1/2)\partial J(\mathbf{v})/\partial \ln(\mathbf{k})$, while the expression on the right of the square brackets is simply $\partial \ln(\mathbf{k})/\partial \mathbf{v}$. The first part of the differential utilizes the adjoint sensitivities $\partial g(\mathbf{k}(\mathbf{v}))/\partial \mathbf{k}$ obtained from each numerical simulation run. The sensitivities, which are the derivatives of each simulated well responses at each time step with respect to model parameters, are obtained by solving a set of adjoint equations backwards in time. In each step, the computation utilizes already computed Jacobian of the linear system of flow equations in a fully-implicit numerical scheme (Li et al., 2001).

We adopt a quasi-Newton Broyden–Fletcher–Goldfarb–Shanno (BFGS) algorithm (Nocedal and Wright, 2006a) for the minimization of the objective function. The BFGS is an iterative algorithm used in solving unconstrained, non-linear optimization problems. This algorithm utilizes the supplied objective function gradient in approximating the system Hessian which facilitates accelerated convergence. At each BFGS iteration in our model calibration workflow, the permeability field is updated based on the set of updated calibration parameters $\mathbf{v}$, and the updated model is evaluated with a numerical simulation. This continues until a specified tolerance is reached in terms of the magnitude of successive objective function reduction. At this point, an iteration set is complete. If needed, additional set of basis function functions are added to improve the resolution of the updated permeability field to begin a fresh iteration set.

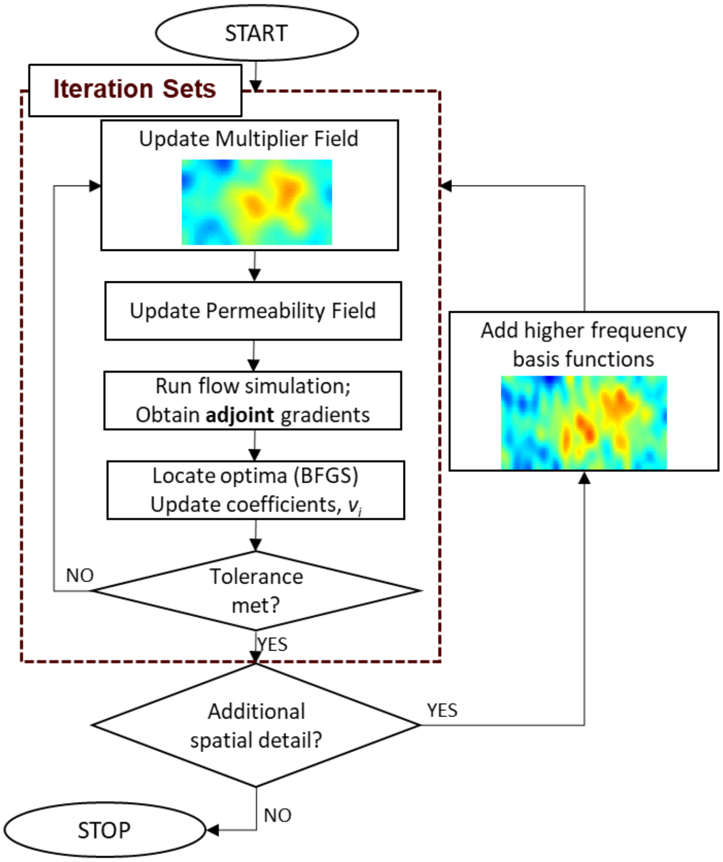

Figure 3.11: Gradient-based model calibration workflow

## 3.6 Illustrative Example

In this section we conduct a numerical experiment to compare the performance between the normal GCT and M-GCT parameterization schemes in terms of convergence and objective function reduction during subsurface model calibration. The example problem is a simple 9-spot pattern waterflood, comprising of 8 producers and one water injector in the center of the pattern. The initial and reference permeability fields, together with the well positions are shown in **Fig. 3.12**. The reservoir model was built with $60 \times 210$ grid cells, each of $40 \times 20 \times 40\,ft$ in dimensions. Reservoir porosity and connate water saturation were both assumed to be constant at $20\%$. For the M-GCT parameterization scheme, the Area of Interest (AOI) is demarcated with the broken red boxes as shown in **Fig. 3.12**. All producers are constrained at $2800\,psia$ bottomhole pressure (BHP) while a water injection rate of $800$ barrels/day is imposed on the injector well (INJ).

The well conditions are kept constant throughout the production history of 3years and over an additional forecast period of 5years. The observed data was generated as the response obtained from a numerical simulation using reference model. Production water cut (WCT) at all wells and the injection BHP acquired through the 3-year historical period are integrated into the initial reservoir model by updating the permeability field. Although the fluid system is three-phase, the reservoir pressure was maintained above the bubble pressure in this case to keep the gas in solution. The model calibration problem utilizes the workflow described in section 5.2 to obtain the best estimate of a set of basis coefficients that reproduce the 3-year long production history for the reference model. In this study, 10 leading basis coefficients are added at the beginning of each of the 4 iterations sets. The objective function was constructed based on well BHP as well as oil and water production rate residuals. Since adjoint sensitivities of well WCT response are not readily available from the simulator, the well WCT data is not included in the objective function definition but only used for results analysis purposes.

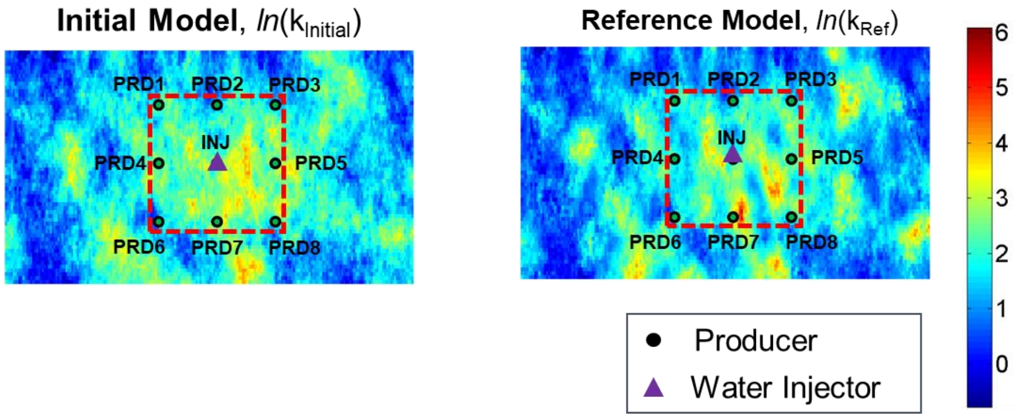

Figure 3.12: Illustrative model calibration problem setup, showing well configuration as well as initial and reference model permeability fields

The objective function decline (shown in natural logarithm values) with respect to iteration sets shown in **Fig. 3.13**. The superior performance of the M-GCT over the normal GCT parameterization schemes is quite apparent in terms of faster convergence speed. However, it is likewise interesting to see that the 3x3 coarsening scheme outperforms the 5x5 coarsening scheme. This appears counter-intuitive considering the trends in image compression improvements within the AOI with more aggressive coarsening, as discussed in section 4. However, it is important to realize that the overall subsurface flow dynamics are impacted by flow physics within and outside the AOI. Therefore, a higher property field resolution within the AOI (more inferior resolution outside the AOI) may not necessarily represent the best model parameterization scheme. The development of an effective approach to determine an optimal coarsening strategy will be a significant contribution toward the robustness of the M-GCT parameterization scheme.

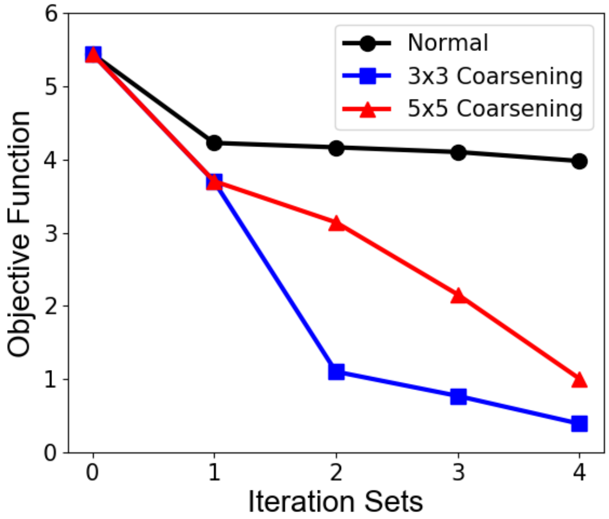

Figure 3.13: Comparison of objective function reduction among the 3 parameterization schemes. Clearly, faster convergence is achieved with M-GCT

Cumulative oil and water production volume matches are compared in **Fig. 3.14(a)** and **(b)** respectively for both history and forecast periods. The observations here clearly agree with the deductions from the objective function plot. Improved reproduction of production history and better production forecast are achieved using the M-GCT parameterization schemes. The calibration quality can also be compared on a well by well level for all parameterization schemes. **Fig. 3.15** shows the production WCT and injection BHP match comparisons over the historical and forecast periods. Note that this example is particularly difficult for any model calibration workflow as water breakthough is observed only in 3 of the 8 producer wells at the end of the 3-year historical period. The WCT breakthough and prediction beyond the historical period can be challenging for most history matching algorithms in such scenarios.

Visual comparison shows that production data matches in historically water producing wells (PRD5, PRD7 and PRD8). Again M-GCT is superior over the normal GCT scheme. Although the WCT prediction for PRD8 based on the 5x5 coarsening M-GCT scheme is slightly inconsistent with observed data, the WCT response of PRD5 based on the normal GCT scheme shows greater discrepancy with historical match. For historically non-water-producing wells, the predications based on the M-GCT scheme consistently provided superior estimates of water breakthrough times compared to the normal GCT scheme. An exception is for PRD2 where the predictions based on the 5x5 coarsening scheme were inaccurate, however the predictions based on the 3x3 coarsening scheme provided a reasonable estimate the same well. This also reflects the overall superior performance of the 3x3 coarsening scheme over the 5x5 coarsening for this problem. Finally, looking at the injection BHP matches and predictions, the results based on the M-GCT parameterization scheme were more precise. The reason for the superior performance of the M-GCT scheme becomes clear by visually comparing the required changes in the permeability field to condition the initial model to the production data shown in **Fig**. **3.16**.

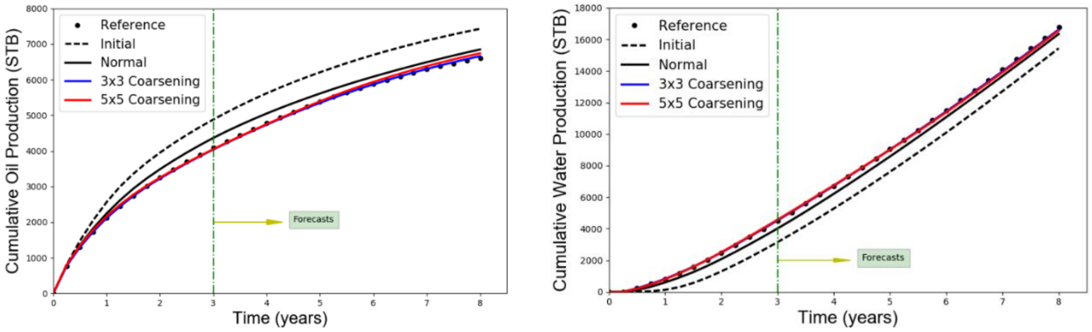

(a) (b)

Figure 3.14: Model calibration results for equally weighted objectives comparing field (a) oil and (b) water production matches and forecasts between Normal GCT and M-GCT parameterization methods. Significant reduction in production data misfit was achieved for all parameterization schemes, however M-GCT resulted in superior fit of the observed data.

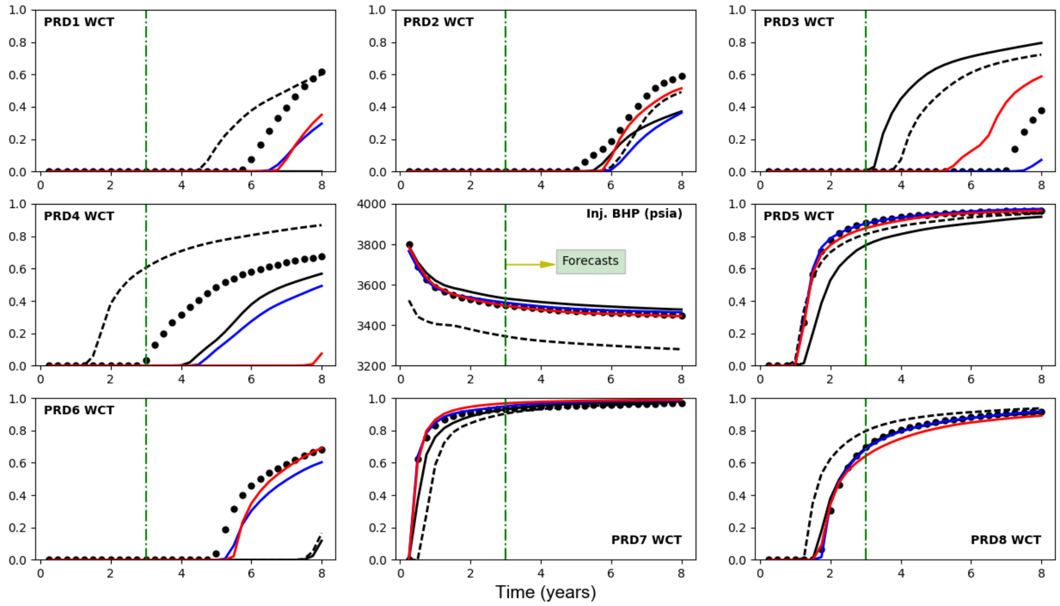

Figure 3.15: Model calibration results at the well level for equally weighted objectives. Picture compares injector BHP and oil and water production matches and forecasts between Normal GCT and M-GCT parameterization methods. Overall, then M-GCT scheme shows superiority in reproduction of production data and production forecasts

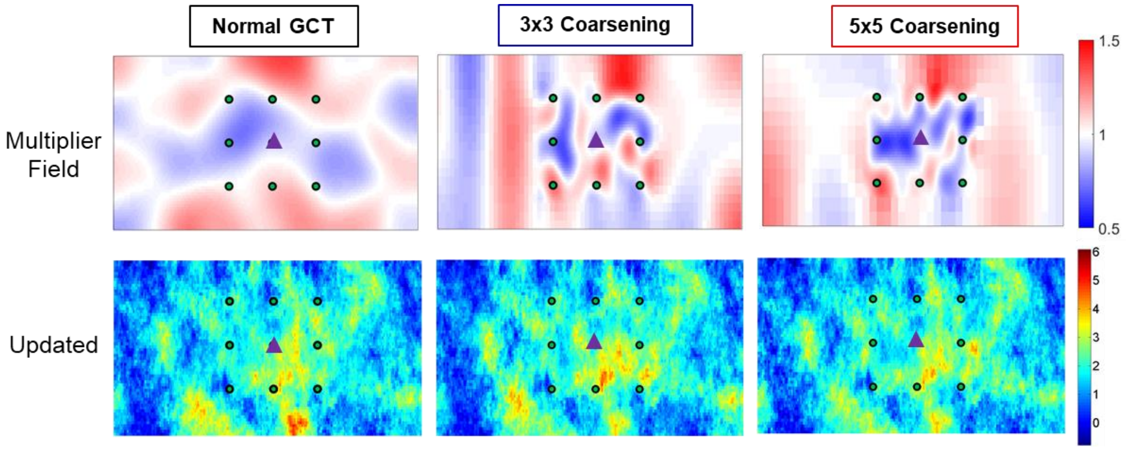

Figure 3.16: Picture comparing final calibrated multiplier fields required to update the permeability fields using the normal GCT scheme and the M-GCT scheme at both 3x3 and 5x5 coarsening levels

Although the overall trends on local increases and reductions in initial model permeability field are similar, the ability of the M-GCT scheme to effect high resolution spatial variations in property field results in the improved performance for this problem. The results obtained from the numerical experiment conducted with this illustrative example can be quantitatively summarized as follows. First, for each well data, we compute a relative residual $\kappa$ which is the ratio of the residual of updated model response to the residual of initial model response through the forecast period, as described in **Eq. 3.11**. The relative residuals are calculated based on the updated models from each parameterization method. compared with the initial model, while a value of $\kappa > 1$shows poorer performance. Second, at the field level, we compute relative errors in cumulative oil and water production at specific times $t$, as described in Eq. 3.12.

$$\kappa = \frac{\left\| \mathbf{d}_{obs} - g(\mathbf{k}_{updated}) \right\|_2^2}{\left\| \mathbf{d}_{obs} - g(\mathbf{k}_{initial}) \right\|_2^2} \tag{3.11}$$

$$Error(\%) = \frac{\left| d_{obs,t}^{FIeld} - g(\mathbf{k}_{updated})_t^{Field} \right|}{d_{obs,t}^{FIeld}} 100\% \tag{3.12}$$

Where $\mathbf{d}_{obs}$ and $g(\mathbf{k}_{updated})$ respectively represent observed well data and simulated well response based on the updated model. Whereas, $d_{obs,t}^{FIeld}$ and $g(\mathbf{k}_{updated})_t^{Field}$ are respectively the observed and simulated field cumulative volume at specific time $t$. The relative residuals are compared in a semi-log bar chart for each well and each parameterization method in **Fig. 3.17**. The dotted line drawn across the plot shows the unit base value of the initial model residuals. It can be observed from the plot that the M-GCT parameterization scheme resulted in improved model calibration, based on production response match at the well level. Exceptions include wells PRD2, PRD4 and PRD8 in which relative residuals obtained from the M-GCT-updated models are slightly higher than that of the normal GCT-updated model. However, the overall trend, as visually observed in **Fig. 3.15**, is a general improvement in model calibration using M-GCT parameterization method.

The relative errors in field-wide cumulative oil and water production for all the three parameterization methods are compared respectively in **Fig. 3.18(a)** and **(b),** showing the relative errors at the end of the 3-year historical and 8-year forecast periods. In the figures, for both historical and forecast periods, the overall superiority of the M-GCT parameterization method over the normal GCT scheme is confirmed. Although relative errors in predicted volumes increased slightly at the end of the forecast period with the M-GCT scheme, relative errors are still much larger with the normal GCT scheme.

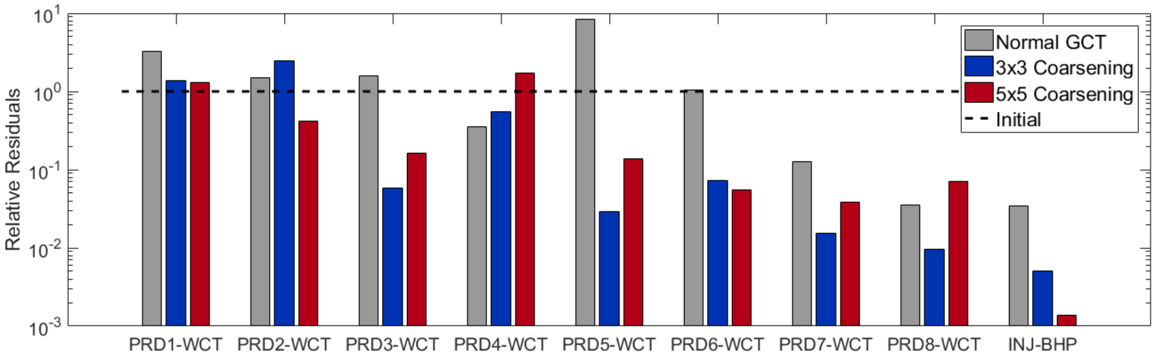

Figure 3.17: Relative error residuals of WCT for all producers and injector BHP data compared between normal GCT and M-GCT parameterization schemes. A value less than 1.0 indicate better match compared with the initial model. A value greater than 1.0 means the updated model performs worse than the initial model in reproducing the historical data.

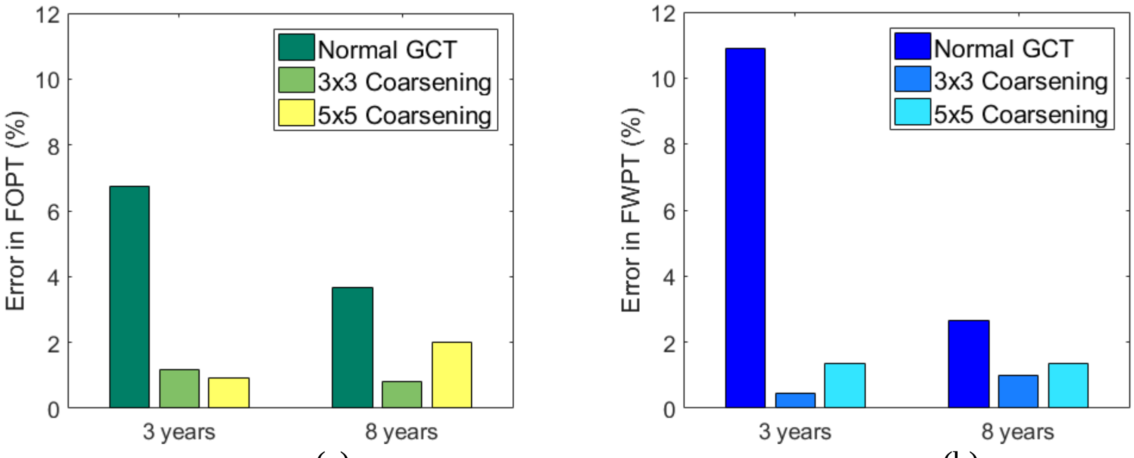

(a) (b)

Figure 3.18: Relative errors in (a) field oil production and (b) field water production responses between reference and calibrated models. Relative errors are compared both Normal and two M-GCT parameterization schemes. M-GCT resulted is smaller relative errors at the end of the 3-year historical period and at the end of the 8-year forecast period.

## 3.7 The Brugge Benchmark Case

We demonstrate the robustness and applicability of the M-GCT parameterization scheme to field scale problems using the Brugge benchmark model (Peters et al., 2010). The simulation model, which was built with realistic geologic features, was intended as a history matching and optimization benchmark case. The geologic model comprises of 7 distinct facies, a single major fault characterized by a significant throw as shown in **Fig. 3.19** and 4 geologic zones (from the top): Schelde, Waas, Maas and Schie. A total of 104 model realizations were generated, each upscaled to $139 \times 48 \times 9$ grid dimensions and approximately 45,000 active grid cells. For our application we have selected the 103rd realization as the initial model to test our parameterization schemes.

As shown in **Fig. 3.19**, hydrocarbons are trapped at the top of the reservoir anticline and consequently, all the wells are placed within and close to the hydrocarbon bearing regions of the formation. This scenario makes the application of the M-GCT parameterization scheme ideally suited for this model calibration problem. This also becomes quite apparent when the overall flux distribution in the reservoir as shown in **Fig. 3.3** is considered. For the M-GCT scheme, we have demarcated the AOI with the red dotted line shown in **Fig. 3.19**.

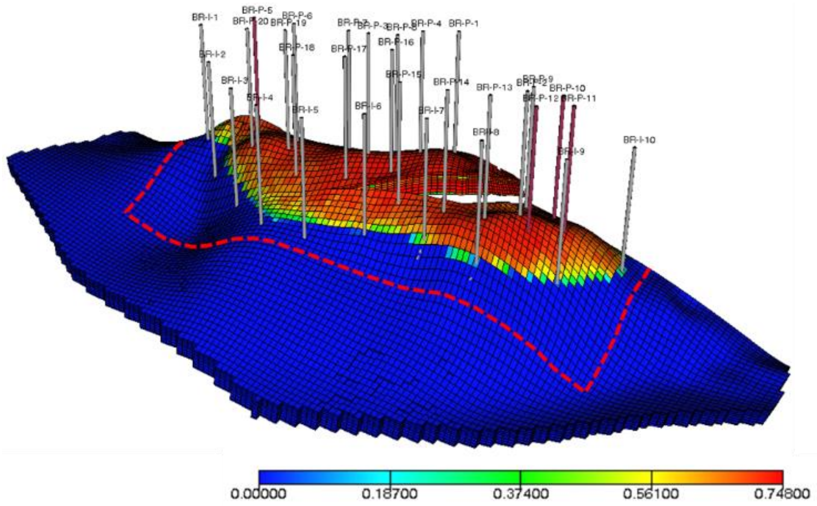

Figure 3.19: The Brugge model description showing reservoir structure, well distribution and initial oil saturation

The reservoir model calibration problem involves integrating 10-year production history from 20 oil producers and 10 peripheral injectors into the initial model by modifying the model permeability distribution. We applied a gradient-based model calibration algorithm with both the normal and M-GCT parameterization schemes. Again here, we compared the performances of both the 3x3 and 5x5 coarsening schemes. A total of 10 leading basis functions were added at each iteration set for a total of 4 iteration sets. To prevent an unwanted smearing of permeability updates across geological zones, the model was parameterized on a layer-by-layer basis. This implies that a total of 90 additional basis coefficients were included in the parameter set for every iteration. For cases ran in this application we selected large values of $\eta$ to preserve geologic realism in the updated permeability model. Again, just to reiterate, the large value of $\eta$ implies more confidence in the prior permeability model and ensures only minor changes will be made to update the permeability field.

Although the gradient-based search is susceptible to getting trapped in local extrema, we observed faster convergence using the M-GCT parameterization scheme. This is self-evident from **Fig. 3.20**. Two iterations using the M-GCT scheme already resulted in objective function values lower than the objective function value obtained at the end of the 4th iteration using the normal GCT scheme. Note that larger reductions in the objective function can be obtained if less emphasis is placed on preserving the prior permeability model. This was the case in the synthetic case discussed in the last section of this chapter. Production data matches of a few key wells are shown in **Figs. 3.21** and **3.22**. Note that we have presented oil and water production rates in terms of dimensionless WCT values.

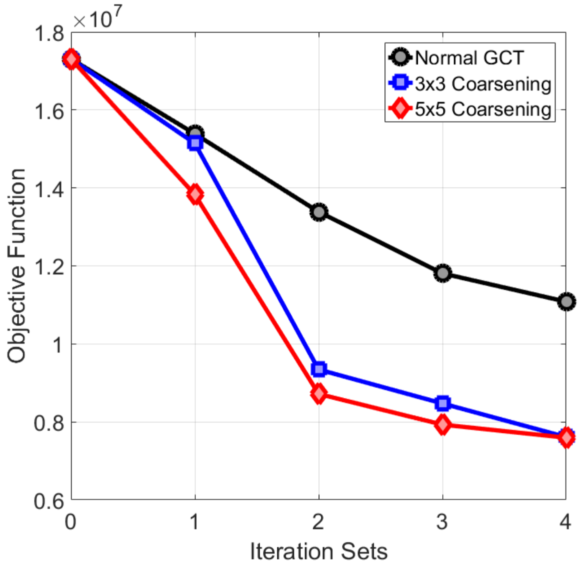

Figure 3.20: Comparison of objective function decline for all model parameterization schemes

It is obvious by first glance at these figures that the prior model only needed minor update to reasonably reproduce the observed production data, hence the choice of $\eta$. As shown in **Fig. 3.21,** although the WCT data matches are generally improved compared to the prior model response, the M-GCT parameterization schemes show clear superiority over the normal GCT method. For instance, in well BR-P-3 normal GCT-updated model resulted in early water breakthrough, whereas water breakthrough is delayed in the M-GCT-updated models, in agreement with the production data. Beyond improved water breakthough time match, amplitude values of WCT after breakthough shows significant improvement using the M-GCT over the normal GCT method. This is clearly depicted in the rest of the wells shown in **Fig. 3.21.** Overall improvement in BHP data match with respect to the prior model is also achieved as shown in **Fig. 3.22.** However, again the M-GCT parameterization scheme shows better performance compared to the normal GCT method. Although in BR-P-9 the BHP match deteriorated in both normal GCT and the 5x5 coarsening M-GCT parameterization scheme, the 3x3 coarsening M-GCT parameterization scheme resulted in improved match of the BHP. Other wells such as BR-P-10 and BR-P-15 also depict the superiority of the M-GCT over the normal GCT parameterization scheme.

Final updated permeability distributions based on the three parameterization schemes are shown in **Fig. 3.25**. Changes required in the initial permeability model are shown in **Fig. 3.26**. Note that these are the multiplier fields by which the initial permeability distribution is updated according to **Eq. 3.8**. For all cases, the results show that high updates are required for both Schelde and Mass geologic zones, but only modest updates in Wass. An interesting observation is that not changes were required for the layer-9 of the model. This is because of two reasons: first, no producer is completed in this layer and second, the small vertical permeability values in the model prevents vertical movement of fluid streams into the layer.

Again, just as was observed in the synthetic case presented in the last section, the overall trends in the permeability changes are roughly similar between the normal and M-GCT schemes. However, higher resolutions of the changes (relatively concentrated within the AOI) attained using the M-GCT scheme results in improved match of the production data.

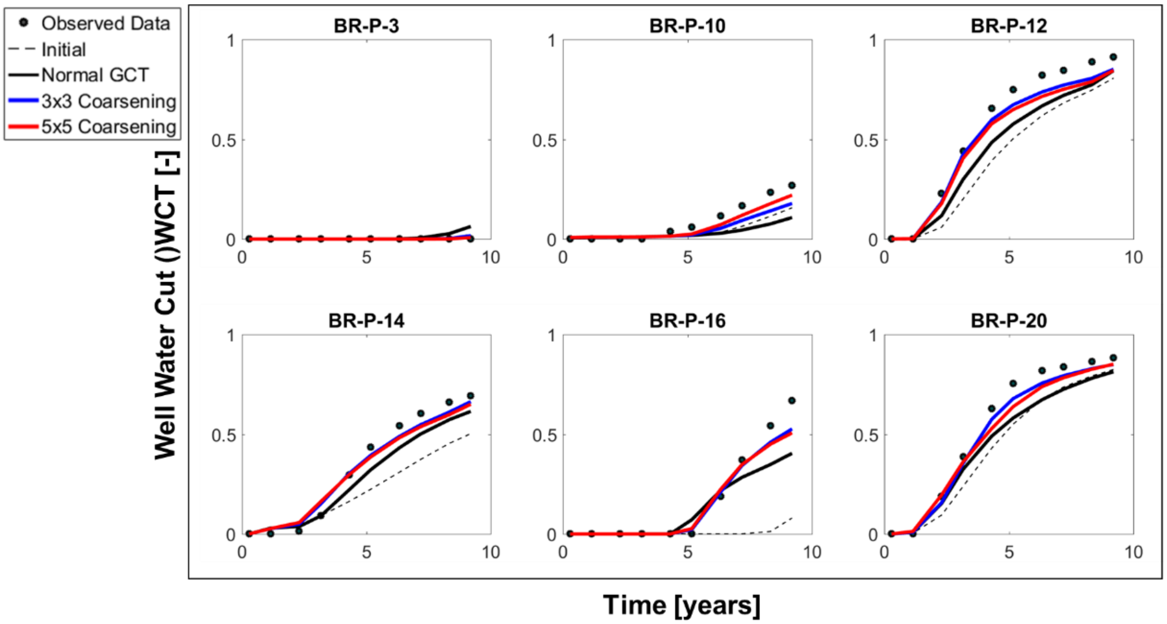

Figure 3.21: Performance comparison between normal and M-GCT schemes based on water cut matches at all producers

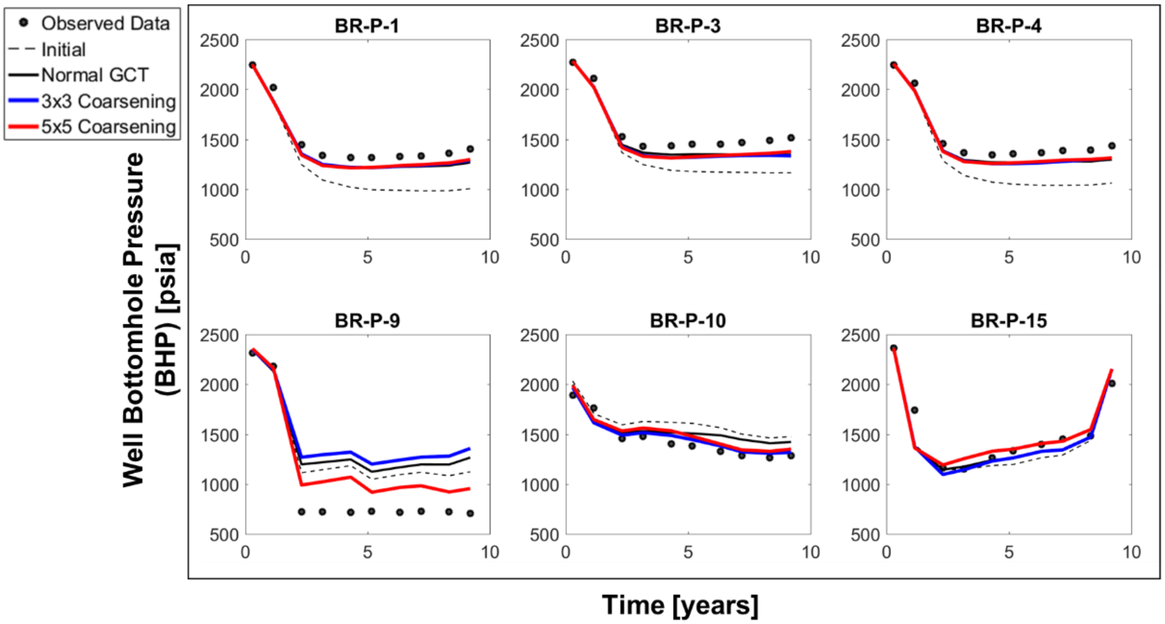

Figure: 3.22: Performance comparison between normal and DR GCT schemes based on bottomhole pressure matches at all producers

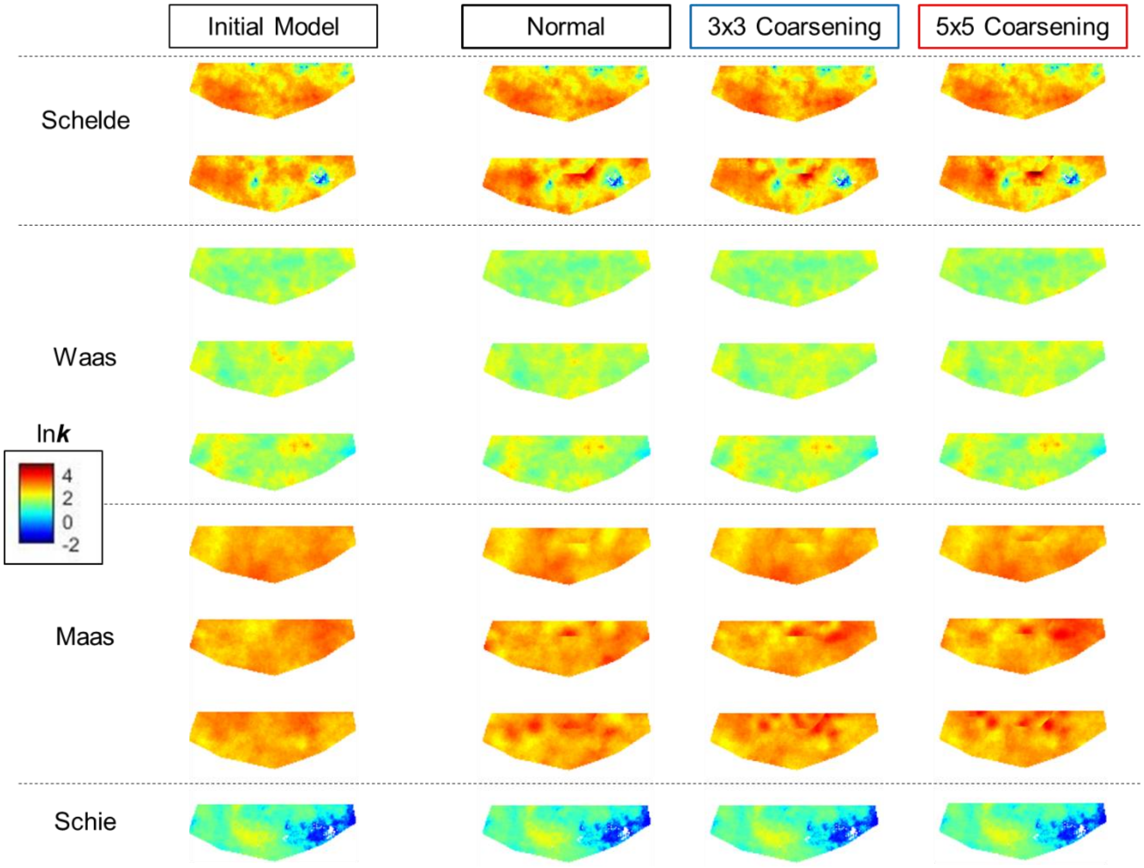

Figure 3.23: Model permeability field update comparison between normal and M-GCT parameterization schemes

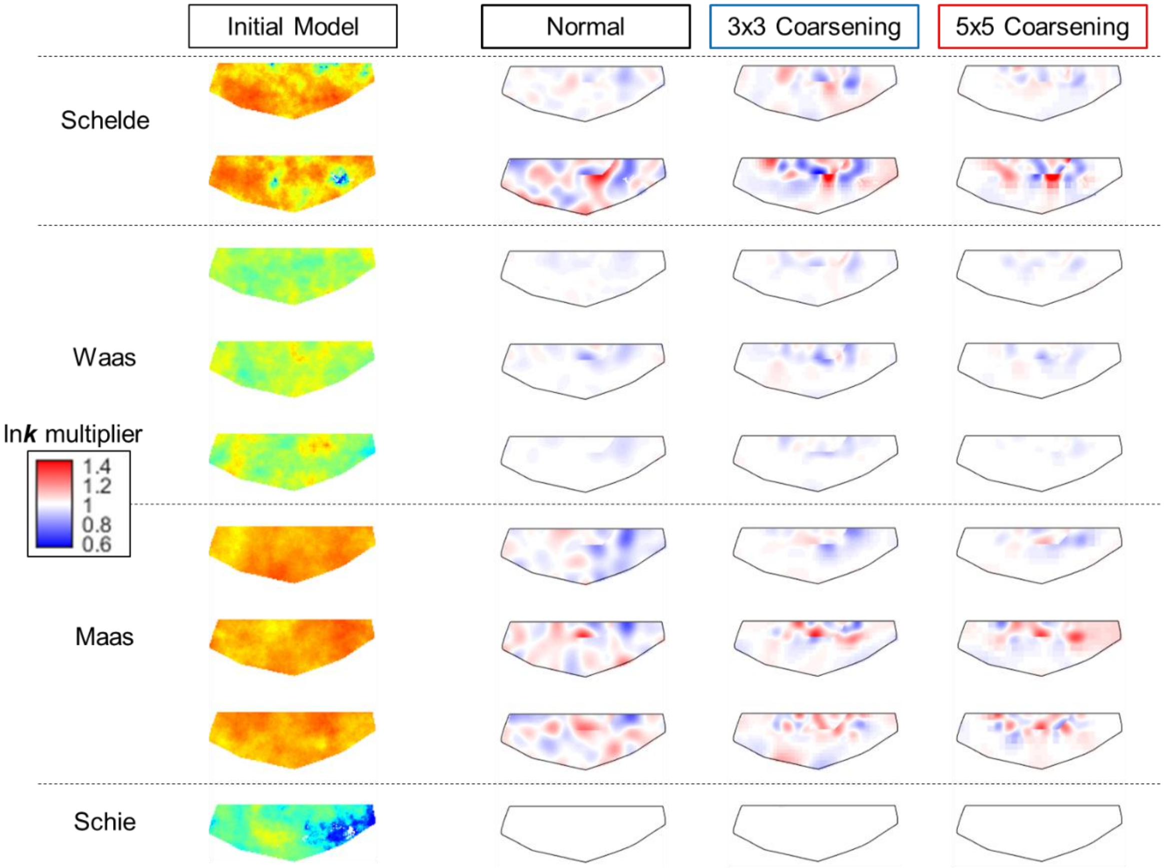

Figure 3.24: Comparison of required changes for model permeability field update between normal and M-GCT parameterization schemes

## 3.8 Field Application

### *3.8.1 Background*

Here we present a field application of our proposed M-GCT parameterization scheme for robust update of high resolution geologic models. We apply our model calibration workflow to the Petra Nova project involving large scale industrially sourced CO2 EOR. Petra Nova, a 50/50 joint venture between NRG and JX Nippon operates a commercial-scale post-combustion carbon capture facility at NRG's WA Parish generating station southwest of Houston, Texas. This facility captures more than 90 percent of the CO2 from a 240 MW equivalent slipstream of flue gas. This is the world's largest post-combustion carbon capture facility installed on an existing coal-fueled power plant. The captured CO2 is being utilized for Enhanced Oil Recovery to increase production at the West Ranch oil field, which is operated by Hilcorp Energy Company and owned by a partnership between Petra Nova and Hilcorp called Texas Coastal Ventures LLC. The field was discovered in 1938 and has been in continuous operation ever since. Since then, it has produced approximately 390 million barrels of oil. Facility construction was commenced after the investment decision in 2014. Pre-EOR water injection was initiated in mid-2016 for pressurizing the target reservoir and then CO2 injection was commenced at the end of 2016.

The reservoir under study has a fluvial geology with large permeability contrasts at varying length scales, ranging from 0.5 to 35,000mD. With a Dykstra-Parsons heterogeneity measure of over 0.9, the reservoir can be categorized as highly heterogeneous (Willhite, 1986). The 140-layer geologic model was discretized into 7 million grid cells of which about 3 million cells are active.  The intermittent stratigraphic shale barriers and baffles contribute to severe vertical permeability anisotropy in the formation. Grid petrophysical properties in the geologic model are shown **Fig. 3.25.**

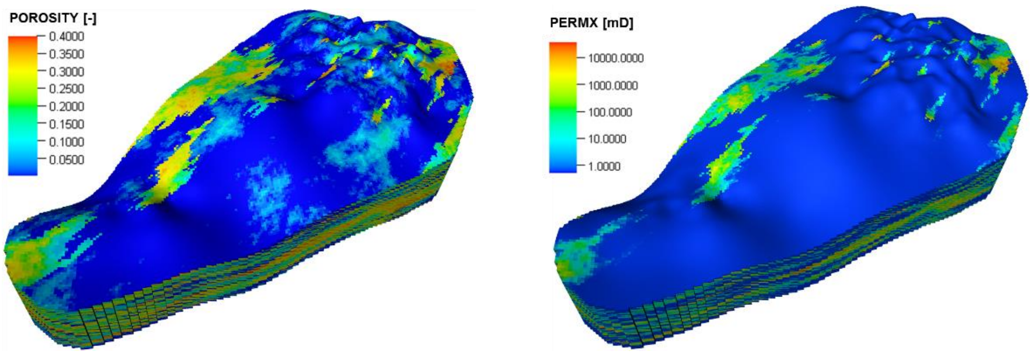

(a) (b)

Figure 3.25: Field geologic model with (a) porosity and (b) permeability distribution

### *3.8.2 Model Calibration Problem*

We integrate reservoir injection data into the reservoir model selected from the ensemble of calibrated models in the previous section. As shown in **Fig. 3.26(a)** the reservoir pressurization period lasted roughly 6 months, 4 of which was exclusively for water injection while the rest of the period featured a combination of water and CO2 injection. The reservoir pressurization involved a total of 38 wells, of which 10 wells were equipped with downhole pressure gauges to measure reservoir pressure over time. About half of these monitoring wells were later converted to CO2 injection wells, leaving 8 dedicated monitor wells. Downhole pressure data were obtained from two of these dedicated monitor wells (MW1 and MW2) at much higher temporal resolutions (daily basis), while the rest, henceforth referred to as observation wells, provided single or few intermittent downhole pressure readings which were all integrated into the geologic model. The locations of all the wells are shown in an aerial view of the model in **Fig.**

**3.26(b)**. In the figure, monitoring wells are shown in black, observation wells in cyan while the empty circles represent the injection wells.

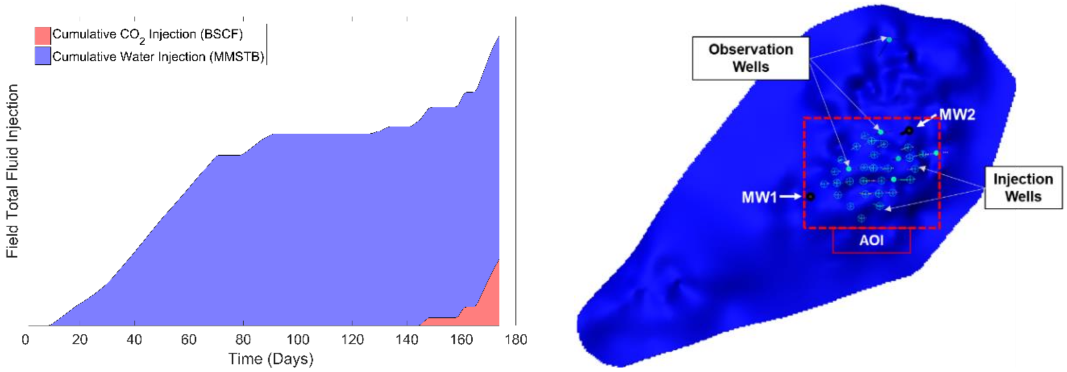

(a) (b)

Figure 3.26: (a) Area plot of cumulative injection of water and CO2 during reservoir re-pressurization campaign (b) Distribution of observation, monitor and injection wells in injection area indicated by the red AOI boundary line

### *3.8.3 Permeability Update*

Here adopt the 5x5 coarsening M-GCT parameterization scheme based on the AOI as defined in **Fig. 3.26(b)**. As discussed in previous sections, our M-GCT parameterization scheme is well suited for this problem due to the localized distribution of wells within the reservoir domain. The M-GCT parameterization scheme facilitates a high-resolution update of the permeability field within the AOI during the model calibration procedure. Some of the M-GCT basis functions used for our application are shown in **Fig. 3.27.** To reiterate, the first basis function is a constant field and therefore plays a vital role in resolving general biases in the property field. The rest of the basis functions show varying frequencies which are responsible for local changes at different length scales in property field during model calibration. In consonance with previous discussion on the M-GCT, the basis functions show larger frequencies within the AOI, compared to outside the AOI. This enhances the desired higher resolution permeability field update within the AOI.

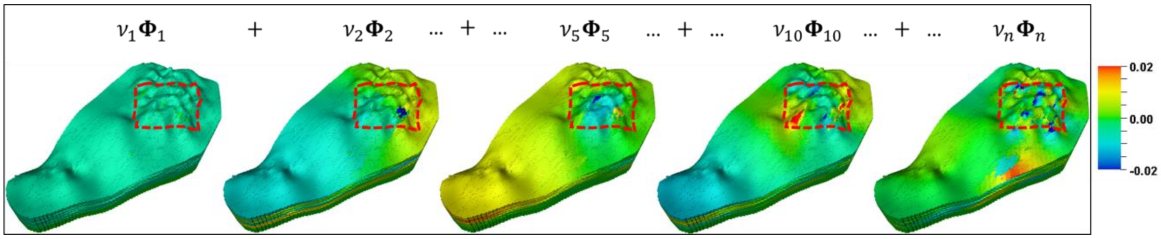

Figure 3.27: Multiresolution Grid Connectivity Transform (M-GCT) basis functions with the AOI indicated by dotted red line

For this problem, each of the 4 zones identified from the energy calibration step (Olalotiti-Lawal et al., 2017) were reparametrized separately. The permeability field is updated using a multiplier field obtained from a linear combination of a small number of basis functions, according to **Eq. 3.2**. Uncorrelated basis coefficients $v_i$, which are generally much fewer in number compared to the model cell count, therefore become the calibration parameters. For this application, 30 basis coefficients were calibrated per zone to update the model permeability. Here as well, the logarithm of the prior permeability field is updated according to **Eq. 3.8.**

Since the reservoir pressure was already above the measured minimum miscibility pressure, we adopted the Todd-Longstaff model (Todd and Longstaff, 1972) for miscible CO2 flood. Based on a series of sensitivity studies (not reported here), a mixing parameter value of 0.6 was selected. Parameters for the selected model from the global energy calibration step (Olalotiti-Lawal et al., 2017) were retained for all simulations in this step. For this application, we adopt an evolutionary approach in the model calibration workflow. The Genetic Algorithm (GA) with a proxy filter (Lophaven et al., 2002) was applied for the search of the best combination of basis coefficients that minimize the objective function. The objective function is defined by the logarithm of the L2 norm of misfits of all observed downhole pressure data, scaled by the standard deviation $\sigma_d$:

$$J = \ln\left(\frac{\left\|\mathbf{d}_{obs} - g(\mathbf{k})\right\|_2^2}{\sigma_d}\right) \tag{3.13}$$

The GA was run with a population size of 100 and over 40 generations. The kriged response surface proxy model applied facilitated an accelerated convergence to a global minimum. **Figs. 3.28(a) and (b)** compare calibrated model responses with observed downhole pressure data for monitoring wells MW1 and MW2 respectively. Compared to the initial model response, an improvement in the pressure data match in the updated models is clear. **Fig. 3.29** compares the initial and updated model permeability distribution. Here, in the interest of brevity, we compare with only the updated model with the lowest objective function. Visually comparing the models and the statistical distribution of the permeability field, it can be observed that only modest changes have been applied in the model update to preserve the geologic realism in the model. More quantitively, the required permeability changes shown in Fig. **3.30(a)** shows that location and magnitude of the permeability changes in the reservoir model. Static pressure data matches are also compared in **Figs**. **3.30(b)** and **(c).** A general improvement in the static pressure match can be observed by comparing the two figures. An exception is one of

ObsWell4 static pressure measurements which was taken earlier during the reservoir pressurization campaign. Assuming measurement errors can be completely ruled out, this inadequacy in the updated model could be resolved by integrating other sources of data, such multiphase production data.

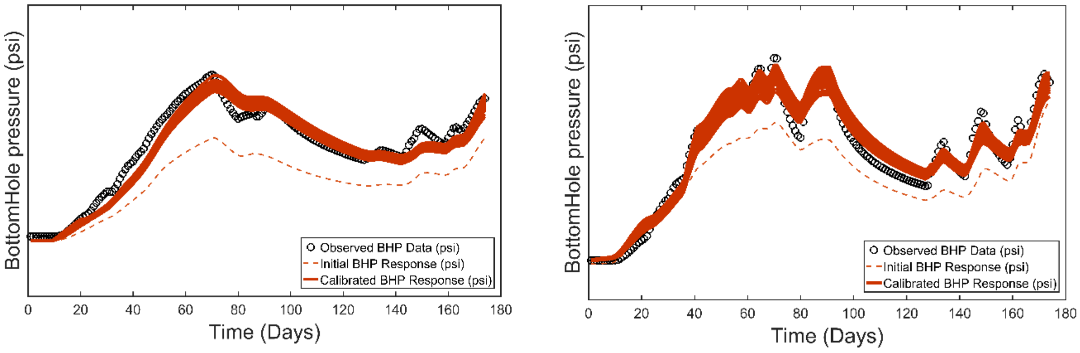

(a) (b)

Figure 3.28: Ensemble of calibraed models compared with observed dowmhole pressure data from monitor wells (a) MW1 and (b) MW2

## 3.9 Conclusions

In this chapter, we have proposed the Multi-Resolution Grid Connectivity Transform (M-GCT) parameterization scheme for subsurface model calibration purposes. The approach generalizes the previously proposed normal Grid Connectivity Transform (Bhark et al., 2011a) to account for spatially varying resolution depending on well or overall flux distribution within the reservoir model. We have compared the compression performances between the two algorithms using series of numerical experiments with a 2D illustrative case and a field scale model. The results demonstrate the superiority of the

M-GCT over the normal GCT parameterization schemes in terms of improved local resolution and faster

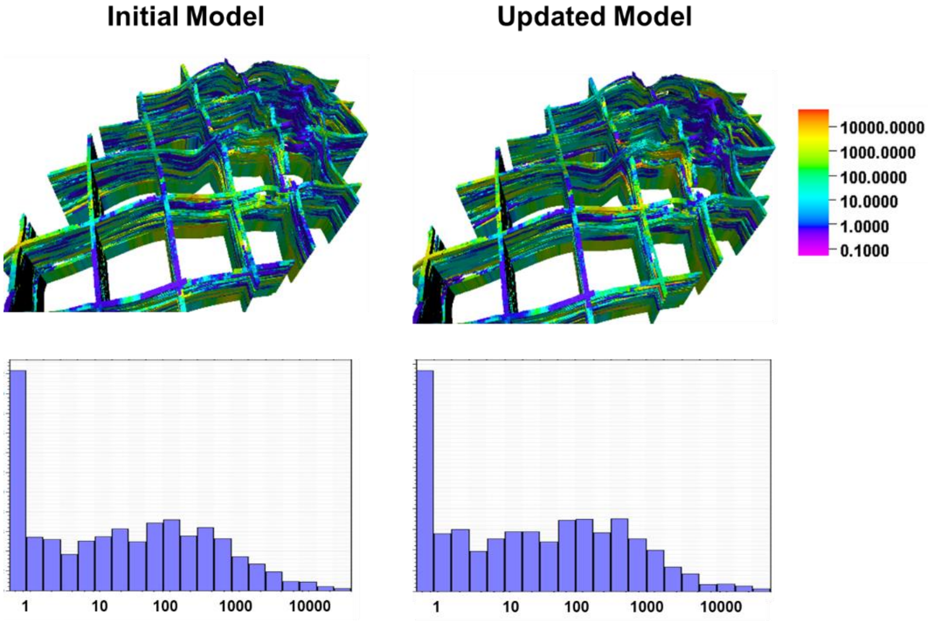

Figure 3.29: Comparison of model permeability distributions in initial and updated models, showing modest changes in prior geologic mode

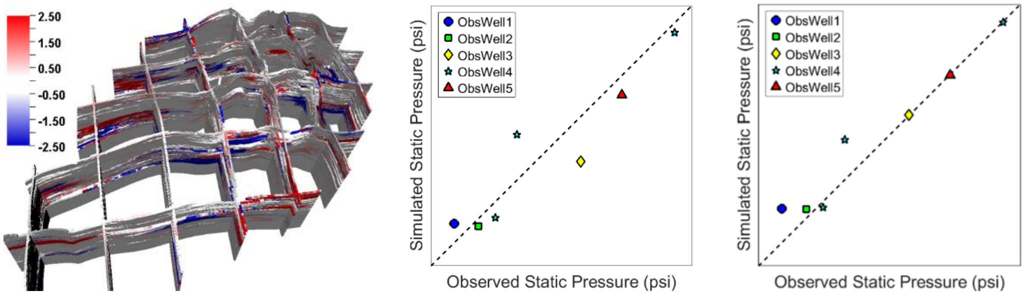

Figure 3.30: (a) Changes required in initial permeability models (b) static pressure response in the prior model compared with observed data (c) ) static pressure response in the updated model compared with observed data

convergence during model calibration. The M-GCT parameterization scheme was successfully applied to update the permeability field of a multimillion high resolution geologic model using a population-based evolutionary algorithm. Based on our observations, the following conclusions can be reached:

1. With the same level of problem dimensionality in the spectral domain (similar number of basis functions), the M-GCT scheme provides higher compression power within the AOI and less compression performance outside the AOI compared to the normal GCT scheme.
2. Compression performance with the AOI improves (and deteriorates outside the AOI) with more aggressive coarsening schemes. This feature of the M-GCT parameterization scheme is shown and quantified in **Figs. 3.6** to **3.9** for both mildly heterogeneous and high contrast systems. The 5x5 coarsening scheme resulted in high compression within the AOI compared to the 3x3 coarsening scheme, which in turn showed better compression compared to the normal GCT. A direct opposite trend is observed outside the AOI. In a nutshell, the M-GCT facilitates higher grid property resolution within the AOI at the expense of the resolution outside the AOI. The right coarsening scheme to apply will somewhat depend on the model calibration problem, in terms of certain features reservoir model and production data. This area is worth exploring.
3. Subsurface model calibration problems can be accelerated using the M-GCT parameterization schemes. This was shown in both the 2D illustrative and field scale

experiments. Although we have applied the M-GCT parameterization scheme using an evolutionary algorithm, the comparison of convergence speeds between M-GCT and normal GCT parametrization schemes we conducted with gradient-based model calibration workflows. Although, we expect a similar conclusion to be reached, an experimental validation of the superiority of the M-GCT parameterization shame to normal GCT could also be explored.

# CHAPTER IV

# OPTIMIZATION OF CO2 EOR AND STORAGE VIA RATE CONTROL IN INTELLIGENT WELLS

Effects of gravity and heterogeneity can significantly impact the performance of CO2 injection for EOR and/or sequestration purposes. Designing optimal injection and production schemes to maximize the sweep efficiency of the injected CO2 and minimize gravity override is a non-trivial exercise. We present an efficient streamline-based approach for optimal injection and withdrawal rate schedules along smart wells with inflow control valves (ICVs) to simultaneously maximize oil recovery and CO2 storage during CO2 WAG process.

Our CO2 flood optimization is based on maximizing sweep efficiency while increasing the viscous to gravity (VGR) ratio to minimize gravity override. The optimization problem is defined with arrival time equalization to maximize CO2 sweep and injection/production acceleration subject to equality and inequality constraints at the well and field levels. First, streamlines are traced and arrival time computed based on flow fluxes are generated using a commercial reservoir simulator. Next, analytical sensitivities are obtained which are used for calculating an approximate Hessian applied in a sequential quadratic programming algorithm for constrained optimization.

The optimization workflow is illustrated with a CO2 WAG flood of a heterogeneous 2D cross-section model where we considered incremental oil recovery, CO2 storage and CO2 utilization factor as the decision variables. We further prove the robustness of our approach with the Norne field application. We consistently show overall improvement in all decision variables using our optimization workflow.

## 4.1 Introduction

One attractive enhanced oil recovery technique is the Carbon Dioxide Enhanced Oil Recovery (CO2 EOR) technology. It is a proven and mature technology that has been profitably adopted in rejuvenating and sustaining productive lives of mature fields for almost half a century (Wallace and Kuuskraa, 2014). In general, CO2 is injected into an oil bearing formation during which it contacts, mixes with and mobilizes in situ residual oil. Typically, a fraction of the injected CO2 is trapped in the subsurface due to capillary and relative permeability hysteresis effects (Krevor et al., 2012; Kumar et al., 2005; Saadatpoor et al., 2010). This phenomenon facilitates permanent underground storage of CO2, which aligns with the goal of global reduction of CO2 concertation in the atmosphere (IPCC, 2005). In fact, a major justification for Carbon Utilization and Storage (CCUS) projects is to rely on the economic benefits of CO2 EOR as a means to offsetting the high cost of Carbon Capture and Storage (CCS) projects (Gozalpour et al., 2005; Melzer, 2012).

Beginning from early 1972 when the CO2 EOR technology was first commercially deployed in the SACROC unit in the Scurry county of Texas (Crameik and Plassey, 1972), the oil and gas industry has witnessed a widespread adoption of the technology for enhancing the value of mature assets especially in North America. In 2012, an average of 282,000 bbl/D of oil was produced by CO2 EOR in the United States and the number is projected to rise over 600,000 bbb/D by the year 2020 (Wallace and Kuuskraa, 2014). The reason is not far-fetched. Although most applications have been in depleted oil reservoirs the onshore environment including sandstone, carbonate (Wilson and Monea, 2004) and recently in unconventional tight formations (Ghaderi et al., 2012; Han and Gu, 2014), offshore application of the technology has started drawing attention (Pham and Halland, 2017). Also, Residual Oil Zones (ROZs) are beginning to generate interests due to its potentially substantial value creation through CO2 EOR (Melzer, 2006). Meanwhile, there have been accounts of deployment of the technology in the Middle East region, including Saudi Arabia (Kokal et al., 2016).

Over the years, the CO2 EOR technology have been applied in different forms, targeted to the specific requirement of the oil-bearing formations for optimal oil recovery. These forms include continuous CO2 injection, Water-Alternating-Gas (WAG) Injection, gravity drainage, huff-and-puff, and so on. Here, we focus on the WAG process which is regarded to be most effective for residual trapping of CO2 in the subsurface (Qi et al., 2009; Spiteri et al., 2005). Regardless of the process employed for CO2 EOR however, quality reservoir management still plays a key role in maximizing the value of the asset through this technology (Wallace and Kuuskraa, 2014). This includes reservoir characterization to understand the features and subsurface flow properties, followed by generation of optimal strategies to be adopted for improved conformance.

Measures to combat flow conformance problems becomes particularly vital for gas injection processes like CO2 WAG. This because of both viscous fingering and gravity override effects, due to differences in multiphase fluid properties including viscosity and density (Orr, 2007). Mitigating associated conformance issues is typically achieved through precautionary screening of potential reservoirs (Taber et al., 1997a; Taber et al., 1997b) as well as effective field development optimization procedures and workflows to optimize well placements as well as fluid rates, taking into cognizance subsurface geological features and existing flow dynamics (Møyner et al., 2015; Onwunalu and Durlofsky, 2011; Passone and McRae, 2007; Sarma et al., 2005; Zhou et al., 2012).

Several field optimization methods for CCUS applications, covering simple analytical, simplified physics and full-physics-based techniques, have been proposed in the literature. Leach et al. (2011) proposed an analytical optimization technique that sought to optimize the fraction of CO2 in the injection stream for maximum economic benefit of any CCUS project. Their conclusion that the economics is insensitive to Carbon tax incentives but solely depends on the economic value of the CO2 EOR component supports the whole preference of CCUS or CCS processes. Utilizing the fractional flow theory that incorporates the crucial gravity override effects, Rossen et al. (2010) was able to estimate the distance to the point of segregation of water and gas fronts from an injection well. According to the authors, through certain injection strategies it is possible to maximize this distance into the formation for improved sweep efficiency. Analytical techniques like these, although generally capture the main trends, tend to address simplified and idealistic versions of the problem.

Other authors have approached the optimization problem more practically. A data-driven approach was adopted by Azzolina et al. (2015) in their work in which a logistic regression was performed on existing datasets from many CO2 EOR sites. Based on the regression model, performance of potential CCUS sites can be probabilistically evaluated and optimized based on oil recovery and CO2 utilization and storage metrics. Like most data-driven techniques however, the reliability of such regressions models are more likely to be restricted by the quality and quantity of training data. Song et al. (2014), on the other hand developed a sensitivity-based optimization workflow, employing reservoir simulation techniques in all scenario evaluations. Essential dimensionless parameters such as WAG ratio, slug size and Voidage Replacement Ratio (VRR) were considered in the optimization problem. Ampomah et al. (2017) applied the Genetic Algorithm (GA) in combination with a proxy construction in optimizing a CCUS project in the Anadarko basin. Ettehadtavakkol et al. (2014) developed field optimization workflows for maximizing the NPV of CCUS projects by considering several parameters including WAG ratio, well placement and well spacing. However, while optimal well placement is important in any field development strategy, operators often find development strategies that require no additional drilling campaigns more economically viable.

Optimizing rates of existing wells helps to meet this requirement. Chen and Reynolds (2017) applied an ensemble-based method in the optimization of the Net Present Value (NPV) of a CO2 WAG process by controlling the rates of the Inflow Control Valves (ICVs) of the intelligent wells. Like all ensemble-based methods however, a large amount of computational power is required to solve the problem. This may be impractical for large field cases. A very successful method which has been applied for rate allocation and optimization in waterflood applications is the streamline-based method (Alhuthali et al., 2010; Park and Datta-Gupta, 2013; Thiele and Batycky, 2006). The superior advantage of the streamline-based technique comes from the unique capability of identifying and quantifying the strength of each source-sink connections based on the flux field in the subsurface. This information is then utilized to modify well or ICV rates to meet certain objectives such as optimizing injection efficiency (Thiele and Batycky, 2003; Thiele and Batycky, 2006), improving sweep efficiency and/or accelerating production (Alhuthali et al., 2006; Alhuthali et al., 2010; Taware et al., 2010). Due to its robustness, the streamline-based optimization method has found applications in other Improved Oil Recovery (IOR) problems such as polymer flood (Ekkawong et al., 2017; Sharma et al., 2011). Recently, Tanaka et al. (2017) proposed a gradient-free streamline-based rate allocation algorithm for maximizing the NPV of an asset. The algorithm was applied to a CO2 EOR problem. However, since the illustrative model was in areal 2-Dimensions, the impact of associated physics such as gravity override was not addressed in the method.

In this chapter, we build upon a streamline-based algorithm proposed by Alhuthali et al. (2010) for the optimization of CCUS projects using smart wells. In our applications, we assume all wells are equipped with ICVs to better mitigate conformance problems (Brnak et al., 2006). We utilize the previous work by Sharma et al. (2016) and, in addition to optimizing cumulative oil recovery, we seek best injection and production rate schedules that result in optimal CO2 storage efficiency and net utilization factor. The co-optimization idea is based on the premise that improved volumetric sweep efficiency during a WAG scheme will not only result in improved oil recovery but also maximize CO2 retention in the subsurface. First, we illustrate the technique with a 2D-cross-section heterogeneous model. We show that with equal cumulative volumetric injection, optimal flow allocation for all ICVs can result in higher oil recovery and CO2 storage efficiency than with a naïve injection strategy. The power and utility of this methodology is demonstrated with the Norne field – a faulted reservoir in the North Sea with similar deductions. This chapter is organized as follows: First, we present the mathematical formulations, define the objective function and pose the optimization problem. Second, we discuss the forward model and the assumptions made in all model evaluations. Then we provide a 2D cross-section illustrative example, and finally the field example to demonstrate the robustness of the optimization workflow for CCUS applications.

## 4.1 Optimization Strategy

### *4.1.1 Mathematical Formulation*

Here we pose the optimization problem we intend to solve. Our overall goal is to maximize volumetric sweep efficiency which in turn results in improved oil recovery, CO2 utilization and storage. For this purpose, we adopt a streamline-based rate optimization technique (Alhuthali et al., 2010) which seeks optimal producer and injector voidage rates that maximizes sweep efficiency while accelerating production.

Given a field with $n_P$ number of producer wells or ICVs, the objective function is defined as follows:

$$f(\mathbf{q}) = \mathbf{e}^T\mathbf{e} + \eta\mathbf{t}^T\mathbf{t}\,;\ \{\mathbf{e},\mathbf{t}\} \in \mathbb{R}^{n_P} \tag{4.1}$$

Where **t** denotes the vector of arrival times at each producer well or ICV, while **e** represents the deviation of each arrival time from the desired equalized arrival time. Essentially, the approach attempts to minimize the variance of arrival times at the producers or ICVs. The objective function can be re-written in more detail as follows:

$$f(\mathbf{q}) = \sum_{m}^{n_{groups}} \sum_{i}^{n_{prod,m}} \left(t_{d,m}(\mathbf{q}) - t_{i,m}(\mathbf{q})\right)^2 + \eta \sum_{m}^{n_{groups}} \sum_{i}^{n_{prod,m}} \left(t_{i,m}(\mathbf{q})\right)^2 \; ; \; \{\mathbf{q}\} \in \Re^{n_W} \tag{4.2}$$

Where $n_{groups}$ denotes the number of well groups in the field. The partitioning of wells and/or ICVs, and the resulting $n_{groups}$ is typically guided by reservoir connectivity, geological information and operator's economic and operational constraints. The number of producer wells or ICVs in the $m^{th}$ group is denoted by $n_{prod,m}$. The constant user-specified parameter $\eta$ denotes the norm weight, the significance of which will be discussed later in this section. The control variable for the optimization problem is a vector of $n_W$ rates at each well or ICV, denoted by $\mathbf{q}$.

To define the arrival times $t_{i,m}$ at each producer, we recall the concept of streamline time-of-flight $\tau$ which is the transit time of a neutral tracer in defined flow field (Datta-Gupta and King, 2007). The time-of-flight at a certain position $\mathbf{x}$ in the domain is mathematically described as follows:

$$\tau(\mathbf{x}) = \int_{\xi} \frac{\phi(\mathbf{x}) A(\mathbf{x}) d\xi}{q} \tag{4.3}$$

Where $q$ is a constant flux along the streamline $\xi$, $A$ represents the streamtube flow area while $\phi$ represents the porosity at position $\mathbf{x}$ along the streamline $\xi$. In other words, $\tau$ is simply the line integral of the inverse of the interstitial velocity along the streamline. The arrival time at a producer $i$ is computed as the average of the arrival times computed on the $n_{FastSL,i}$ fastest streamlines arriving at the producer:

$$\hat{t}_{i,m}(\mathbf{q}) = \frac{1}{n_{FastSL,i}} \left( \sum_{k=1}^{n_{FastSL,i}} \frac{\tau_{k,i}}{\left(df_g / ds_g\right)_{s_g @ BT}} \right) \tag{4.4}$$

In our application $n_{FastSL,i}$ is taken as the fastest 20% of all streamlines arriving at the producer. Note that the gas arrival times at each producer is approximated as the ratio of the time-of-flight to the shock speed at breakthrough which relies solely on the fractional flow function (Lake, 1989). Furthermore, to improve CO2 retention, we penalize the calculated arrival time after gas breakthrough as follows (Taware et al., 2010):

$$t_{i,m}(\mathbf{q}) = \hat{t}_{i,m}(\mathbf{q}) \left( 1 - \frac{WGOR_i}{WGOR_{i,MAX}} \right)^{\alpha} \tag{4.5}$$

Where $WGOR_i$ and $WGOR_{i,\max}$ respectively represent the current and maximum allowable Gas-Oil Ratio at producer $i$. The exponent $\alpha > 0$ measures the importance of the penalty. While the penalty is completely ignored when $\alpha = 0$, large values of $\alpha$ heavily penalizes producers experiencing gas breakthroughs. Depending on the value of $\alpha$ and the relative GOR values, the arrival time is penalized by forcing a reduction in $\hat{t}_{i,m}(\mathbf{q})$, which eventually results in the reduction of rates along any injector-producer pair involving producer $i$.

The desired arrival time for the $m^{th}$ group is them computed as an arithmetic average of the arrival times computed as each producer:

$$t_{d,m}(\mathbf{q}) = \frac{1}{n_{prod,m}} \sum_{i=1}^{n_{prod,m}} t_{i,m}(\mathbf{q}) \tag{4.6}$$

In essence, the objective function involves two terms which individually seek to achieve different goals. The first term of **Eq. 4.1** alone seeks to equalize arrival times at all producers by minimizing arrival time residuals. The second term alone, on the other hand, seeks to accelerate production by minimizing the magnitude of arrival times at all producers. The specified norm weight $\eta$ indicates the relative importance of the production acceleration objective over the arrival time equalization objective. The implication of this pertaining to our CO2 EOR and storage optimization is that both objectives are expected to combine to optimize volumetric sweep efficiency. The arrival time equalization objective optimizes the areal sweep while the production acceleration objective enhances the Viscous-to-Gravity ratio (VGR) (Sharma et al., 2016; Tchelepi and Orr Jr, 1993) to improve the vertical sweep efficiency. Concisely, the optimization problem is therefore posed as:

$$\min_{\mathbf{q}} \; f(\mathbf{q}) \tag{4.7}$$

Subject to: $g(\mathbf{q}) = 0$; $h(\mathbf{q}) \le 0$

for some $g : \mathbb{R}^{N_{Wells}} \to \mathbb{R}^{N_{EQ}}$ and $h : \mathbb{R}^{N_{Wells}} \to \mathbb{R}^{N_{IEQ}}$

In other words, we minimize the objective function subject to $N_{EQ}$ equality constraints $g(\mathbf{q})$ and $N_{IEQ}$ inequality constraints $h(\mathbf{q})$ using on the control variable $\mathbf{q}$ which, again, is a vector of all injection and production rates. The constraints include field injection and production/processing capacity, voidage and bottomhole pressure constraints. The formulation for these is provided in detail by Alhuthali (2009). In solving our optimization problem, we apply the Sequential Quadratic Programming (SQP) algorithm (Nocedal and Wright, 2006a) by utilizing the SQP module in-built in MATLAB (Mathworks, 2016). The required function gradient and hessian are analytically computed.

First, a multivariate differential of **Eq. 4.1** with respect to $\mathbf{q}$ gives the gradient of the objective function and can be written as follows:

$$\nabla f(\mathbf{q}) = 2\nabla \mathbf{e}^T \mathbf{e} + 2\eta \nabla \mathbf{t}^T \mathbf{t} = 2\left(\mathbf{J}^T \mathbf{e} + \eta \mathbf{S}^T \mathbf{t}\right) \tag{4.8}$$

Here, we refer to the gradient of $\mathbf{t}$ as the sensitivity $\mathbf{S}$, and the gradient of the arrival time residuals $\mathbf{e}$ as the Jacobian $\mathbf{J}$. By combining **Eqs 4.1** and **4.6**, $\mathbf{S}$ and $\mathbf{J}$ will be given by:

$$\mathbf{J} = \left[J_{ij}\right] = \left[\left(\frac{1}{n_{prod,m}} \sum_{i=1}^{n_{prod,m}} S_{ij}\right) - S_{ij}\right] \tag{4.9}$$

$$\mathbf{S} = \left[S_{ij}\right] = \left[\frac{\partial t_{i,m}}{\partial q_j}\right] \tag{4.10}$$

Note that in both matrices defined above, the $i, j$ indices respectively point to the $i^{th}$ producer and the $j^{th}$ well or ICV. The overall computational efficiency of our optimization workflow comes directly from the streamline-based sensitivity calculation method which requires a single numerical simulation run. Secondly, we obtain the hessian of the objective function by taking the second derivative of **Eq. 4.1**. This can be approximately obtained as:

$$\nabla^2 f(\mathbf{q}) \cong 2\left(\mathbf{J}^T\mathbf{J} + \eta\mathbf{S}^T\mathbf{S}\right) \tag{4.11}$$

The hessian computed here is a reasonable approximation since truncated terms are by and large negligible (Duijndam, 1987).

### *4.1.2 Optimization Workflow*

Our adopted optimization workflow follows Alhuthali et al. (2010). The workflow, graphically presented in **Fig. 4.1**, iteratively optimizes rates at each time step by utilizing streamline-based analytical gradient and hessian computed from a single simulation run. The steps involved are outlined as follows:

1. Carry out a numerical simulation for the current time step by restating from a time step directly preceding it. Restarting simulation runs is a common feature provided by standard reservoir simulation software packages such as ECLIPSE (Schlumberger, 2014). The simulation restart feature affords the assurance that the current time step is initialized with the optimized state of the previous time step.
2. Trace streamlines based on underlying flux field and obtain arrival times at each producer (Jimenez et al., 2010). As mentioned earlier, in the calculation of the arrival times at the producer, only the 20% fastest streamlines are taken into consideration.
3. Compute sensitivities, gradient and hessian of the objective function. Again, the beauty and elegance of our workflow is that the gradient and hessian can be calculated

based on a single numerical simulation run, which significantly improves the computational efficiency of the optimization workflow.

4. Construct and solve the SQP problem by incorporating desired equality and inequality constraints. Then update the well and/or ICV rates.
5. Repeat steps 1 through 4 over user-specified $n\_itr$ iterations for the current time step. In all applications reported in the work, $n\_itr$ was kept at 10
6. Finally, repeat for all desired time steps.

In other words, the entire workflow entails conducting numerical simulations for each individual time steps for $n\_itr$ times. Therefore, the cost obtaining optimal injection and production rate schedules is by and large equivalent to conducting only $n\_itr$ full simulations on the model. This in itself clearly validates the superiority of the streamline-based optimization workflow compared to evolutionary, population-based and ensemble-based algorithms in terms of computational overhead.

## 4.2 Forward Model

For all applications reported here, reservoir simulation was conducted using the ECLIPSE reservoir simulator (Schlumberger, 2014). For simplicity purposes, we assume a first contact miscible system and estimated fluid density, viscosity and relative permeability using the Todd-Longstaff empirical approach (Todd and Longstaff, 1972). Also, in our CO2 WAG evaluations, gas phase hysteresis was simulated using the Land trapping empirical functions.

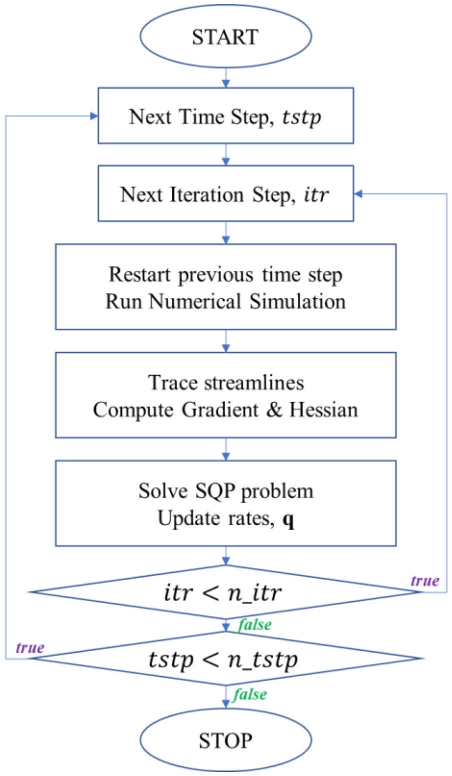

Figure 4.1: Streamline-based rate optimization workflow

### *4.2.1 Fluid Miscibility Model*

Miscibility of CO2 is generally known to be critical for overall oil recovery efficiency (Blunt et al., 1993; Kovscek, 2002). The assumption of first contact miscibility in our CO2 flood simulations requires the estimation of the effective fluid properties for both oil and gas (CO2) phases at all location in the domain and all times. For this we adopt the Todd-Lonstaff  empirical treatment of physical dispersion effects in the miscible mixture (Todd and Longstaff, 1972). The treatment models a two-phase system, with oil and gas component in the miscible phase and water representing the other phase. It requires the specification of the mixing parameter $\omega$ which ranges between 0 (indicating negligible mixing) and 1 (indicating perfect mixing). The effective oil and gas component viscosities, $\mu_{o,eff}$ and $\mu_{g,eff}$ are thus respectively computed as:

$$\mu_{o,eff} = \mu_o^{1-\omega}\mu_m^{\omega} \tag{4.12}$$

$$\mu_{g,eff} = \mu_g^{1-\omega}\mu_m^{\omega} \tag{4.13}$$

Where $\mu_{m,eff}$ represents the mixture viscosity given as:

$$\left(\frac{1}{\mu_m}\right)^{\frac{1}{4}} = \frac{\tilde{s}_g}{\tilde{s}_o + \tilde{s}_g}\left(\frac{1}{\mu_g}\right)^{\frac{1}{4}} + \frac{\tilde{s}_o}{\tilde{s}_o + \tilde{s}_g}\left(\frac{1}{\mu_o}\right)^{\frac{1}{4}} \tag{4.14}$$

Where $\tilde{s}_o = s_o - s_{or}$ and $\tilde{s}_g = s_g - s_{gc}$

Effective oil and gas relative permeabilities in the mixture are computed by scaling the relative permeability of the miscible phase $k_{rn}(s_n)$ with the saturation fractions of either phase, mathematically written as:

$$k_{rg} = \left(\frac{\tilde{s}_g}{\tilde{s}_o + \tilde{s}_g}\right)k_{rn}(s_n) \tag{4.15}$$

$$k_{ro} = \left(\frac{\tilde{s}_o}{\tilde{s}_o + \tilde{s}_g}\right)k_{rn}(s_n) \tag{4.16}$$

The effective oil and gas densities are calculated using the effective viscosities computed in **Eqs. 4.12** and **4.13** as well as the nominal densities and viscosities of the unmixed phases:

$$\rho_{o,eff} = \left( \frac{\mu_o^{1/4}\left(\mu_{o,eff}^{1/4} - \mu_g^{1/4}\right)}{\mu_{o,eff}^{1/4}\left(\mu_o^{1/4} - \mu_g^{1/4}\right)} \right)\rho_o + \left( 1 - \frac{\mu_o^{1/4}\left(\mu_{o,eff}^{1/4} - \mu_g^{1/4}\right)}{\mu_{o,eff}^{1/4}\left(\mu_o^{1/4} - \mu_g^{1/4}\right)} \right)\rho_g \qquad (4.17)$$

$$\rho_{g,eff} = \left( \frac{\mu_o^{1/4}\left(\mu_{g,eff}^{1/4} - \mu_g^{1/4}\right)}{\mu_{g,eff}^{1/4}\left(\mu_o^{1/4} - \mu_g^{1/4}\right)} \right)\rho_o + \left( 1 - \frac{\mu_o^{1/4}\left(\mu_{g,eff}^{1/4} - \mu_g^{1/4}\right)}{\mu_{g,eff}^{1/4}\left(\mu_o^{1/4} - \mu_g^{1/4}\right)} \right)\rho_g \qquad (4.18)$$

Note that the value of the mixing parameter $\omega$ dictates the resultant values for both effective (mixed) oil and gas densities and viscosities. It is easy to show that when $\omega = 0$ effective component densities and viscosities identically yield their respective pure (unmixed) values.

### *4.2.2 Trapping Model*

To quantify CO2 retention by residual trapping, it was necessary to model gas phase hysteresis during our CO2 WAG simulations using a trapping model. Similar to common simulation approaches for incorporating this important pore scale physics (Krevor et al., 2015; Qi et al., 2009), we make use of a trapping model proposed by Land (1968) whereby the gas phase relative permeability during imbibition is estimated from the drainage relative permeability:

$$k_{rg}^{imb}(s_g) = k_{rg}^{drain}(s_{g,f}) \qquad (4.19)$$

Where $s_{g,f}$ is given as a function of the trapped gas saturation $s_{g,trap}$ and the Land parameter $C$:

$$s_{g,f} = s_{g,cr} + \frac{1}{2}\left[ \left(s_g - s_{g,trap}\right) + \sqrt{\left(s_g - s_{g,trap}\right)^2 + \frac{4}{C}\left(s_g - s_{g,trap}\right)} \right] \qquad (4.20)$$

The trapped gas saturation $s_{g,trap}$ is calculated as a function of the Land parameter $C$, the maximum gas saturation during drainage process $s_{g,m}$ and critical gas saturation $s_{g,cr}$:

$$s_{g,trap} = s_{g,cr} + \frac{s_{g,m} - s_{g,cr}}{1 + C\left(s_{g,m} - s_{g,cr}\right)} \tag{4.21}$$

The Land parameter $C$ measures the relative strength of residual trapping in the porous media. Smaller values result in more trapping (larger $s_{g,trap}$ values) and vice versa.

## 4.3 Performance Metrics

With respect to CCUS objectives, we adopt three performance metrics to evaluate and compare models for optimality (Hovorka and Tinker, 2010; Leach et al., 2011; Melzer, 2012). These metrics are both computed as functions of physical time and pore volume (of both water and CO2) injected $(PVI)$. These field-wide metrics are defined as follows:

(1) Oil Recovery Efficiency, $E_{rec}$: This is the cumulative oil $(V_{Oil\,\mathrm{Prod}}^{SC})$ produced at the end of the project as a percentage (or fraction) of oil in place $(OIP)$. That is:

$$Oil\,\mathrm{Re}\,cvoery(\%) = \frac{V_{Oil\,\mathrm{Prod}}^{SC}}{OIP} \times 100 \tag{4.22}$$

Here, both $V_{Oil\,\mathrm{Prod}}^{SC}$ and $OIP$ are computed at standard conditions and $E_{rec}$ is only incremental, in that $OIP$ is the amount of oil in place at the initiation of the CO2 WAG scheme.

(2) Net CO2 Utilization Factor: This is the amount of CO2 retained in the formation per incremental standard barrel of oil produced. It is calculated as the ratio of the difference in

cumulative CO2 injected $(V_{CO2Inj}^{SC})$ and produced $(V_{CO2\mathrm{Prod}}^{SC})$ to cumulative oil production $(V_{Oil\,\mathrm{Prod}}^{SC})$ at standard conditions, mathematically described as:

$$CO2UF(MSCF/STB)=\frac{V_{CO2Inj}^{SC}-V_{CO2\mathrm{Prod}}^{SC}}{V_{Oil\,\mathrm{Prod}}^{SC}} \tag{4.23}$$

(3) CO2 Storage Efficiency, $E_{store}$: We compute this as a product of the CO2 trapping efficiency, $E_{trap}$ and the placement efficiency, $E_{plac}$ (Vitoonkijvanich et al., 2015). Where the CO2 placement efficiency is the volume of CO2 retained the reservoir as a fraction of reservoir pore volume while CO2 trapping efficiency is the volume of immobilized CO2 as a fraction of the volume CO2 in place, both at reservoir conditions. Mathematically we have:

$$E_{store}=E_{trap}\times E_{plac} \tag{4.24}$$

Where

$$E_{plac}=\frac{V_{CO2Inj}^{RC}-V_{CO2\mathrm{Prod}}^{RC}}{PV}\text{ and }E_{trap}=\frac{V_{CO2Trapped}^{RC}}{V_{CO2Inj}^{RC}-V_{CO2\mathrm{Prod}}^{RC}} \tag{4.25}$$

In all computations of CO2 utilization factor, we assumed with negligible CO2 losses (Melzer, 2012). We also compared the classical injection efficiency which is the volume of oil production as a percentage of fluid volume injected at reservoir conditions. Finally, we compared WAG ratios in each cycle, computed as the water injection to CO2 injection rate at reservoir conditions.

## 4.4 Illustrative Example

We begin with a demonstration of the optimization workflow with a with a 2D cross-section reservoir model shown in **Fig. 4.2**. The model is discretized into $100\times 60$

grid cells, each with dimensions $50 \times 100 \times 3 ft$. Absolute permeability in the reservoir model ranges between $10mD$ and $30{,}000mD$ with vertical anisotropy ratio $kvkh = 0.3$ and porosity assumed constant at $\phi = 0.2$. An injector and a producer re placed at the two ends of the model, with each having 30 ICVs installed. The problem was initialized to mimic a typical candidate for CO2 EOR in the field. We assumed a water-wet system with relative permeability functions shown in **Fig. 4.3**. Initial oil saturation was set to residual conditions at $0.4$ with no free gas initially present. A $4000 psia$ initial reservoir pressure was specified and a Todd-Longstaff mixing parameter $\omega = 0.67$ was assumed. While residual gas saturation in the drainage process was set at $0.0$, we assumed a Land parameter $C = 2.0$ for residual CO2 trapping in the imbibition process.

A list of the production and operational constraints imposed on the optimization problem is provided in **Table 4.1**. Note that we have imposed a unit Voidage Replacement Ratio $(VRR)$ to prevent decline in reservoir pressure, which is undesirable for CO2 flood applications. Also the constraint helps to avoid unfavorable increase in pressure above fracture limits. We compared the optimized cases with a base case which is set up to inject the maximum possible fluid volume, approximately $3PV$, over the 20-year life of the project. Through the life of the project, a WAG cycle of 1 year was maintained, with CO2 and water injection periods lasting 6 months in each cycle for all cases. Concretely, the optimization workflow routine shown in **Fig. 4.1** was repeated through $40$ time steps for this problem. We ran the optimization algorithm on the problem with norm weight $\eta = 0$ and $\eta = 1000$ in each case. To reiterate, a zero value of $\eta$ indicates an emphasis on areal sweep efficiency optimization whereby streamline arrival times are equalized at the producer ICVs. A positive value of $\eta$ on the other hand seeks an optimal combination of rates that maximizes both areal and vertical sweep efficiency through production acceleration.

Table 4.1: Inequality and equality constraints for the 2D cross-section optimization problem

| **Constraint Type** | **Constrained Parameter** | **Value** |
|---|---|---|
| Inequality Constraints | Field-wide production rate | $\leq 2250 RB/D$ |
| | Field-wide injection rate | $\leq 2250 RB/D$ |
| | Producer well ICV rate | $\leq 400 RB/D$ |
| | Injector well ICV rate | $\leq 400 RB/D$ |
| | Production bottomhole pressure | $\leq 5000\, psi$ |
| | Production bottomhole pressure | $\geq 3000\, psi$ |
| | Production GOR at ICVs | $\leq 1000 MSCF/STB$ |
| Equality Constraint | Voidage Replacement Ratio $(VRR)$ | 1.0 |

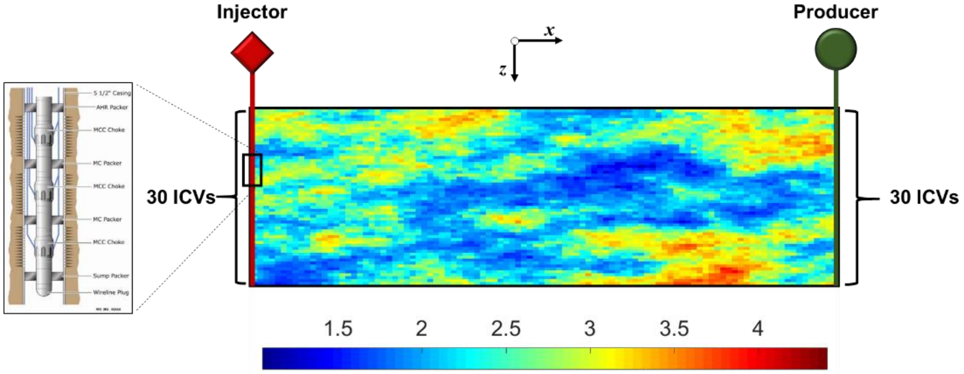

Figure 4.2: Reservoir model showing permeability distribution (with values ranging from 10 to 30,000mD), producer and injector wells each with 30 ICVs installed. Inset shows a typical ICV design (Brnak et al., 2006)

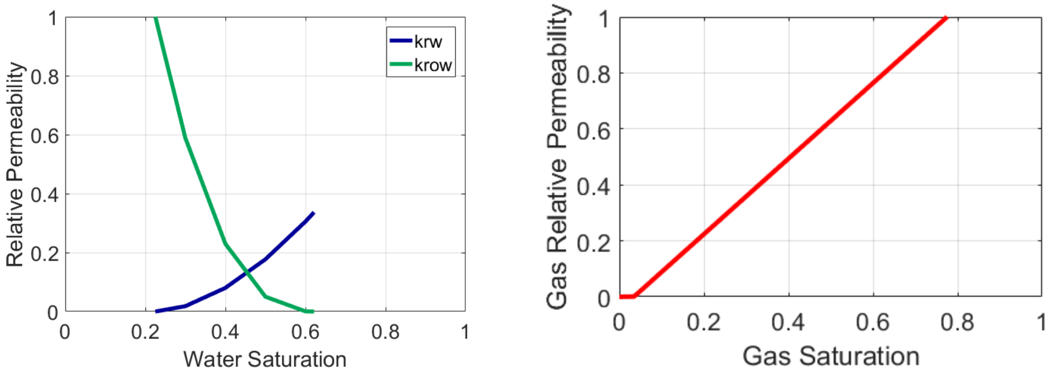

(a) (b)

Figure 4.3: (a) Oil-water relative permeabilities indicating a water-wet formation (b) Gas relative permeability

A comparison between the results obtained based on the optimization algorithm and the base case is provided in **Fig. 4.4**. From this figure, the impact of the rate optimization procedure is apparent. It can be observed that oil saturation is reduced and trapped CO2 is increased by the sweep efficiency optimization $(\eta = 0)$. Further improvements in these can also be noticed as more emphasis is placed on volumetric sweep efficiency, that is $\eta = 1000$. As shown in the figure, while rates are uniformly distributed for all ICVs in the naive (base) case, improved sweep was achieved in the optimized cases by adjusting rates according to the underlying heterogeneity and gravity forces. In response to gravity forces, higher injection and production rates were maintained through ICVs located towards the bottom part of the two wells.

The results of this example are quantitatively presented in terms of the previously discussed metrics. The incremental oil recovery efficiencies are compared with respect to both physical time and $PVI$ in **Figs. 4.5(a)** and **(b)** respectively. An additional $5\%$ and $10\%$ incremental oil recovery over the base case were achieved with $\eta = 0$ and $\eta = 1000$ in the optimized cases respectively. As can be observed in the dimensionless recovery plot in **Fig. 4.5(b)**, although with less $PVI$, more oil was recovered in the case with $\eta = 0$ due to improvement in areal sweep efficiency. With $\eta = 1000$ however, improved areal and vertical sweep efficiencies were combined to result in higher incremental oil recovery.

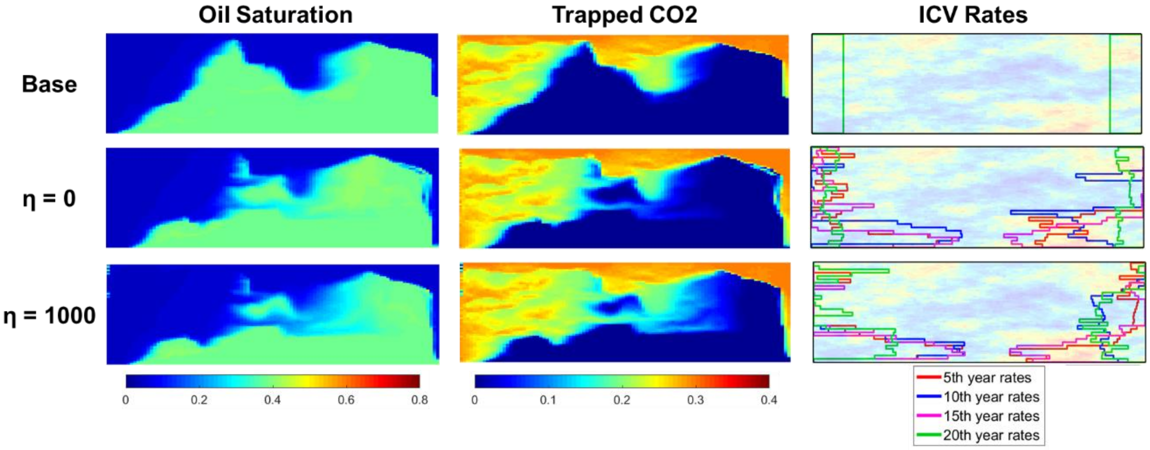

Figure 4.4: Visual comparison of flood performance for base case (on top) and optimized cases. First and second columns respectively compare oil and trapped gas saturation profiles at the end of the 20-year period. Third column overlays injector and producer profiles on the formation permeability distribution.

Similar trend can be observed in the CO2 storage efficiencies, $E_{store}$ compared in **Figs. 4.8(a)** and **(b)**. This should be expected because higher incremental oil recovery can be attributed to improved CO2 sweep which also results in more residual trapping of CO2 in the formation. However, the trapping efficiencies $E_{trap}$ were observed be similar for all cases as shown in **Fig. 4.7(a)**, while placement efficiencies $E_{plac}$ have the major contribution to $E_{store}$ as shown in **Fig. 4.7(b)**. Less monotonicity can be noticed in $E_{plac}$ profile the case with $\eta = 0$. This is because of more frequent changes rates and WAG ratio as a function of time compare the other cases. The reduction $E_{plac}$ for the case with $\eta = 0$ is due to the overall decline in injection rates and increase in WAG ratio at later time. These can be observed from the 20th year rate plots in **Fig. 4.4** and in **Fig. 4.9(b)** respectively.

The $CO2UF$ profile follows a typical trend of sharp decline to a stable value with time for all cases as shown in **Figs. 4.6(a)** and **(b)**. Clearly form these figures, the improvement in incremental oil recovery and CO2 storage efficiency achieved with the optimization workflow comes with the same net CO2 utilization factor, $CO2UF$ as the base case. This observation is in fact consistent with the results recorded for both incremental oil recovery and CO2 storage efficiencies. Based on **Eq. 4.23**, higher incremental oil recovery indicates larger CO2 retention and thus, higher CO2 storage efficiency.

The areal sweep efficiency optimization ($\eta = 0$) case turns out have the highest injection efficiency as shown in **Fig. 4.9(a)**. This observation is consistent with the incremental oil recovery plots in Figs. **4.5(a)** and **(b)** where the dimensionless plot shows an incremental oil recovery efficiency close to the case where $\eta = 1000$.

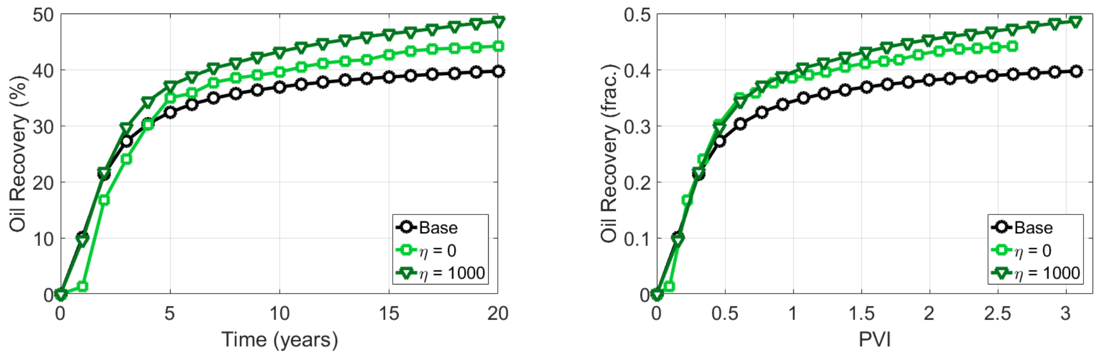

(a) (b)

Figure 4.5: Incremental Oil recovery efficiency as a function of (a) time in years and (b) reservoir pore volume injected

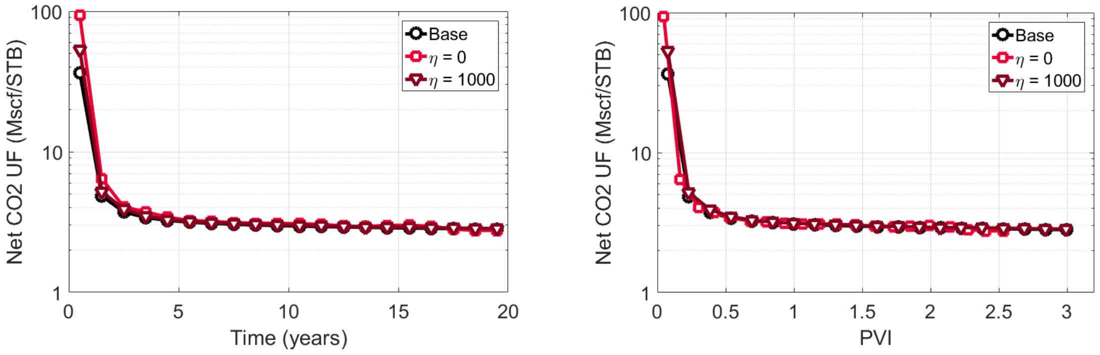

(a) (b)

Figure 4.6: Net CO2 utilization factor as a function of (a) time in years and (b) reservoir pore volume injected

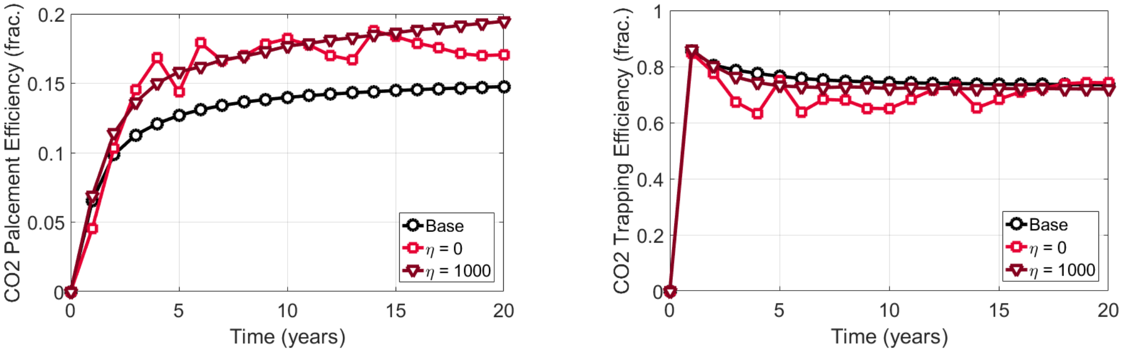

(a) (b)

Figure 4.7: (a) CO2 placement efficiency and (b) CO2 trapping efficiency as a function of time

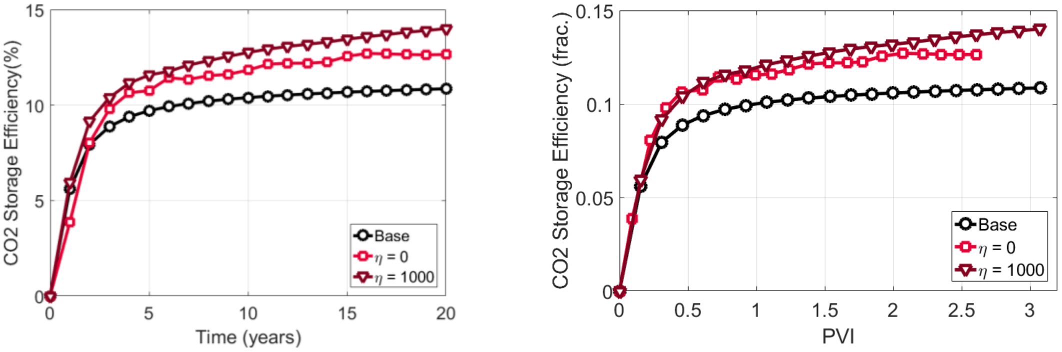

(a) (b)

Figure 4.8: CO2 storage efficiency as a function of (a) time in years and (b) reservoir pore volume injected

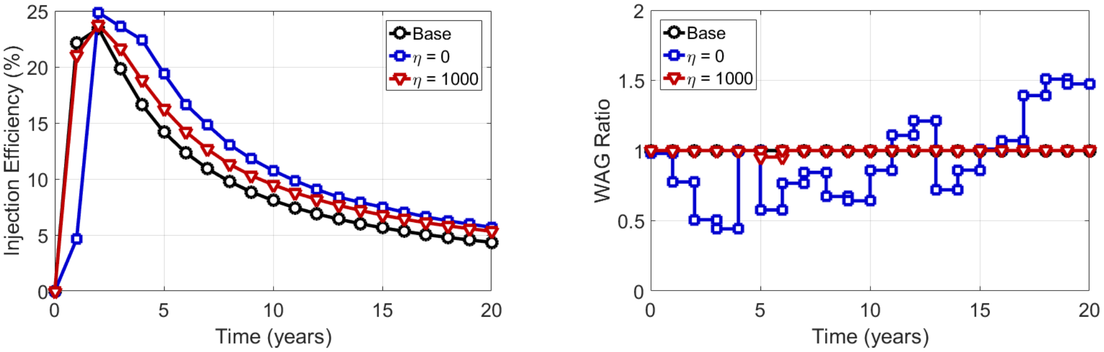

(a) (b)

Figure 4.9: (a) Injection efficiencies comparison (b) WAG ratios comparison

## 4.5 Norne Field Application

### *4.5.1 Background*

Discovered in late 1991, the Norne field is situated in blocks 6608/10 and 6508/10, 80km north of the Heidrun oil field in the North Sea. The sandstone reservoir consists of five main geological zones namely Garn, Not, Ile, Tofte and Tilje buried between 2500 – 2700m below sea level with 110m column of oil and 25m of gas (Morais, 2012; Rwechungura et al., 2010). Gas is predominantly found in the Garn sands while Ile is the oil bearing formation. The Tofte and Tilje sands contained mostly water. The reservoir fluids distribution is shown in **Fig. 4.10(a)**. The Not formation forms a stratigraphic barrier preventing vertical communication between Garn and the rest of the sands (Rwechungura et al., 2010). Formation porosity ranges between 0.25 to 0.3 while permeability lies between 20 and 2500mD (Steffensen and Karstadt, 1996). The reservoir structure is features a complex fault network, shown in **Fig. 4.10(b)** by which the reservoir is compartmentalized into four segments – C, D, E, and G exhibiting varying strengths in communication, resulting in 6 equilibrium regions.

The reservoir simulation model was constructed with $46 \times 112 \times 22$ grid cells of which $44431$ grid cells are active. Through a period of oil production lasting between 1997 and 2006, about 50% of the original Oil Initially in Place (OIIP) has been recovered with only 50 wells (33 producers and 17 injectors). Field development operations included both classical water injection and a short period of natural gas injection. Previous work by Morais (2012) investigated the added value of gas injection on the field through Water-

Alternating-Gas (WAG) and Simultaneous Water-Alternating-Gas (SWAG) schemes. In their work, using the active wells (13 producers and 8 injectors) control variables for sensitivity studies and optimization include well configurations, injection rate, WAG ratio and slug size. In our application here, we evaluate the value of a CO2 WAG scheme on the Norne field, specifically applying our optimization algorithm.

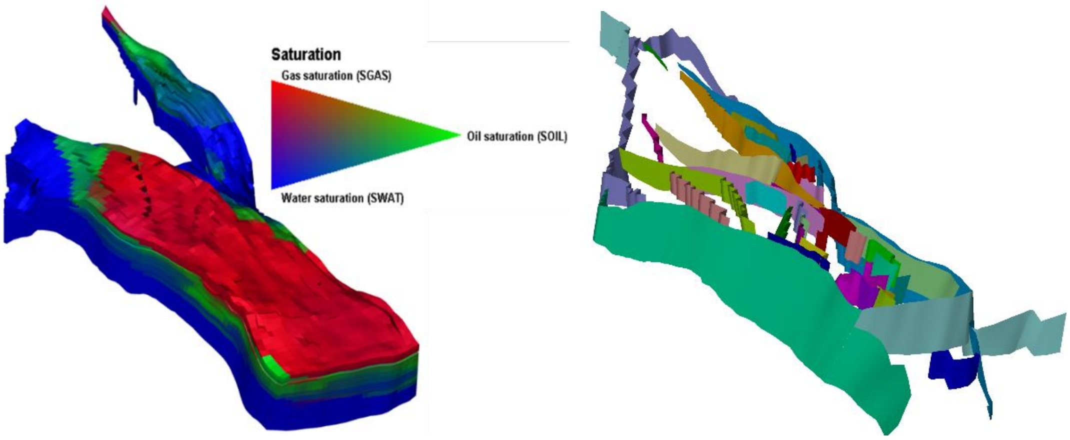

(a) (b)

Figure 4.10: Norne field reservoir model showing (a) initial fluids distribution and contacts and (b) fault network

### *4.5.2 Problem Description*

We utilize the median realization of previously calibrated models which were updated by integrating available 4D seismic data and 10 years of production history into the prior reservoir model (Watanabe et al., 2017). **Figs. 4.11(a), (b)** and **(c)** respectively show the spatial distribution of the model porosity, Net-to-Gross (NTG) and permeability, as well as the distribution of wells utilized in the rate optimization workflow. Vertical permeability anisotropy, $kvkh$ ratio varies between $0.01$ and $1.0$ through geological zones, with an average value of $0.3$. The CO2 WAG development plan involves of 8 injectors (shown in black) and 13 producer wells (shown in white). The three-phase relative permeability and capillary pressure functions, shown in **Figs. 4.12(a), (b)** and **(c)** are scaled according to the connate fluid saturations characterizing each rock type in the formation. With an average reservoir pressure of $250 bars$ at the initiation of the CO2 WAG scheme, we assumed a miscible CO2 with a Todd-Longstaff mixing parameter $\omega = 0.67$. In this application we assumed a Land trapping parameter $C = 2.0$.

An average of 5 ICVs were installed in each well in the optimization problem. The CO2 WAG scheme was run for 10 years, alternating between CO2 and water injection every year. The operational constraints imposed are summarized in **Table 4.2**. Here as well, as in the synthetic case, the $VRR = 1.0$ was imposed to keep reservoir pressure within safe operational limits. The maximum field injection/production value was set so that a unit value of Hydrocarbon Pore Volume $(HCPV)$ would be injected at the end 10-year CO2 WAG development program in the base case. The base case was set up such that all ICVs produce and inject at fixed reservoir rates of $1000 SM^3 / D$ throughout the 10-year period. The movement of CO2 in the formation was tracked using the concentration of a numerical tracer activated in the injected CO2.

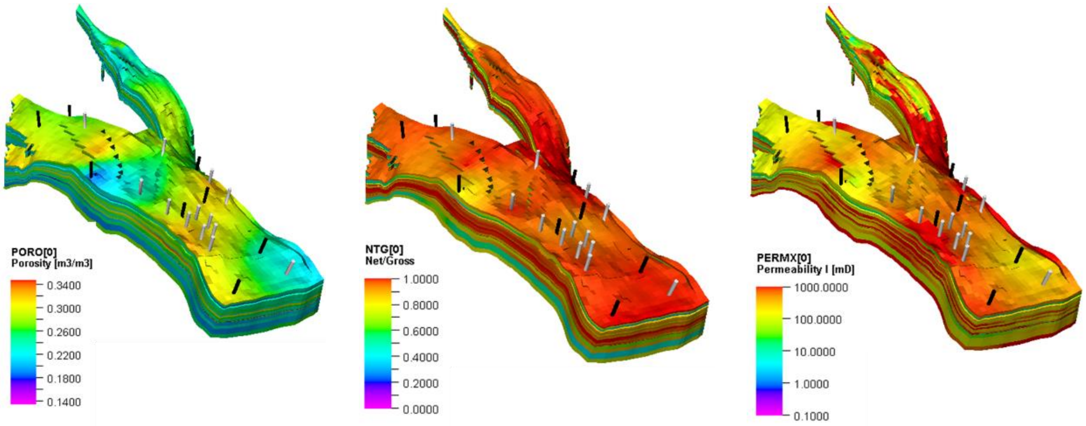

(a) (b) (c)

Figure 4.11: Calibrated reservoir model grid property distribution: (a) porosity (b) Net-to-Gross (NTG) and (c) permeability field. Also shown are well locations with injectors shown in black and producers in white

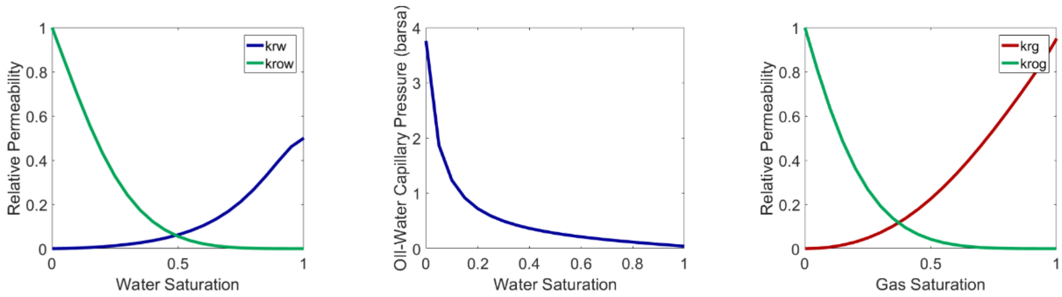

(a) (b) (c)

Figure 4.12: Three-phase relative permeability can capillary pressure curves: (a) Oil-water relative permeability function (b) Oil-water capillary pressure function and (c) Oil-gas relative permeability function

Table 4.2: Inequality and equality constraints for the Norne field application

| **Constraint Type** | **Constrained Parameter** | **Value** |
|---|---|---|
| Inequality Constraints | Field-wide production rate | $\leq 50000 SM^3 / D$ |
| | Field-wide injection rate | $\leq 50000 SM^3 / D$ |
| | Producer well ICV rate | $\leq 3000 SM^3 / D$ |
| | Injector well ICV rate | $\leq 3000 SM^3 / D$ |
| | Production bottomhole pressure | $\leq 500 bars$ |
| | Production bottomhole pressure | $\geq 150 bars$ |
| | Production GOR at ICVs | $\leq 1000 SM^3 / SM^3$ |
| Equality Constraint | Voidage Replacement Ratio $(VRR)$ | 1.0 |

### *4.5.3 Results and Discussion*

Similar to the synthetic case, the optimization algorithm was run in two scenarios: $\eta = 0$ and $\eta = 1000$ to evaluate the effect of considering gravity forces in the optimization problems. The concentration of CO2 in all the three cases run are compared in **Figs. 4.13** through **4.15**. The field-wide sweep of CO2 in the formation is clearly at maximum in the base case and the lowest in the case with $\eta = 1000$. The seeming contradiction of this result with the synthetic case can be explained by considering the structure of the objective function. As more emphasis is placed on production acceleration (as $\eta$ increases), larger is weight is placed in minimizing arrival time at each of the producer ICVs. As a result, since producers are predominantly completed within the oil rim, arrival times are minimized by keep injections within this zone. Therefore, in the case with $\eta = 1000$, the injected CO2 is concentrated within the oil rim with little injection above and below the zone. This can also be validated with a plot of average CO2 concertation within each zone at the end of the 10-year WAG scheme, as shown in **Fig. 4.16**. The figure clearly shows high CO2 concentrations within the oil rim and lower CO2 concentrations outside the oil rim in the case with $\eta = 1000$, compared to the base case. The case with $\eta = 0$ consistently showed intermediate values. Based on this, it is therefore expected that the optimized cases result in higher incremental oil production but with lower CO2 storage capacity compared with the base case.

The conflicting behavior of the oil recovery efficiency and CO2 storage efficiency objectives can be clearly observed in **Figs. 4.17** and **4.20**. Although incremental oil recovery efficiency was improved by the rate optimization algorithm, a reduction in CO2 storage efficiency $E_{store}$compared can be directly noticed compared to the base case. Again, as shown in **Fig. 4.19(b)**, the CO2 trapping efficiencies, $E_{trap}$ are essentially similar because of consistent trapping mechanism in all cases. The CO2 placement efficiency $E_{plac}$which, according to **Fig. 4.19(a)** varies in each of the cases, solely determines the value of $E_{store}$. In this application however, due less variation in rates and WAG ratios compared in **Fig. 4.21(b)**, $E_{plac}$showed the expected monotonic increase for the case with $\eta = 0$, unlike in the synthetic case.

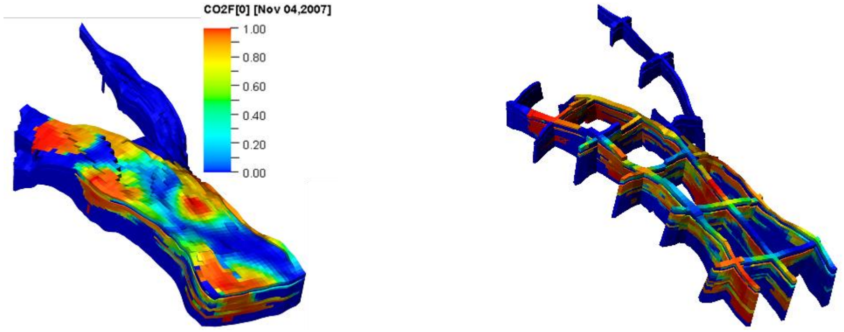

(a) (b)

Figure 4.13: CO2 concentration for base case (a) in full-field view and (b) in cross-sectional view for the Norne field case

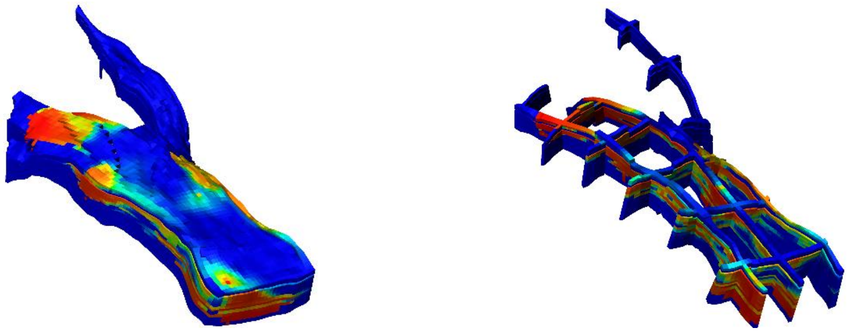

(a) (b)

Figure 4.14: CO2 concentration for optimized case ( $\eta = 0$ ) (a) in full-field view and (b) in cross-sectional view for the Norne field case

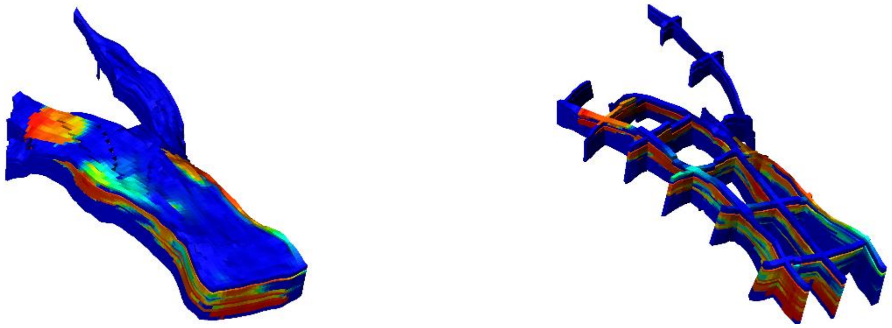

(a) (b)

Figure 4.15: CO2 concentration for optimized case ( $\eta = 1000$ ) (a) in full-field view and (b) in cross-sectional view for the Norne field case

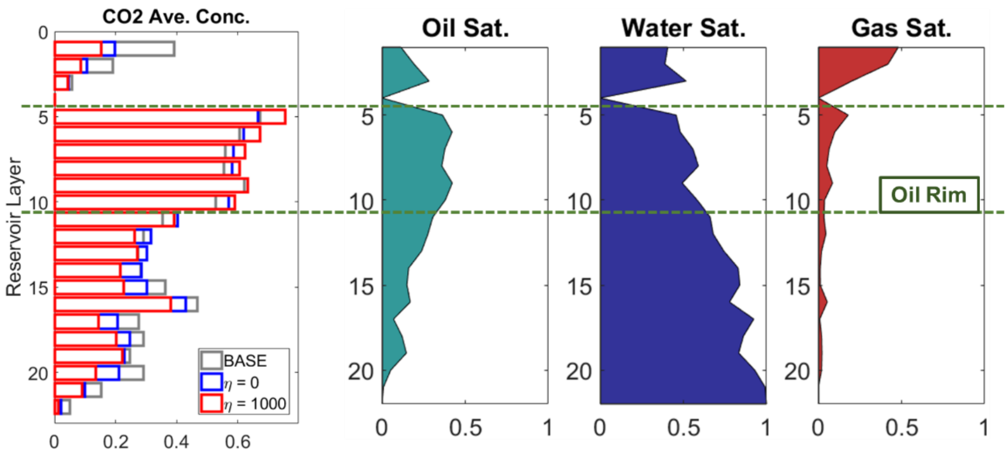

Figure 4.16: Comparison of CO2 injection conformance between base and optimized cases. Optimized cases show more CO2 invasion within the oil rim and less outside the oil rim

The injection efficiencies show a trend similar to the observation in the synthetic case. As shown in **Fig. 4.21(a)**, the injection efficiency is consistently at maximum with $\eta = 0$ and minimum with the base case. The impact of the injection efficiency can be observed directly in the dimension plots of incremental oil recovery andCO2 storage efficiency $E_{store}$ respectively in **Figs. 4.17(b)** and **4.20(b)**. While $E_{store}$ for the case where $\eta = 0$ became close to that of the base case, the incremental oil recovery with $\eta = 0$ became slightly higher than the case with $\eta = 1000$. Poor injection efficiency in the base case, although came with improved $E_{store}$ values, it resulted in poor CO2 utilization factor $CO2UF$, as shown in **Figs. 4.18(a)** and **(b)**. The computed $CO2UF$ for the base case is approximately twice the value of the optimized cases at the end of the 10-year project life. Note that CO2UF is computed in field units so that a $CO2UF$ of $400$ recorded for the optimized cases is equivalent to $2.25 MSCF / STB$, which falls within range of the values obtained in the synthetic case.

In this application, the $E_{store}$ was observed to show some conflict with other objectives in that higher $E_{store}$ values were computed for the base case compared to the optimized cases, while the base case was inferior in other objectives including incremental oil recovery, $CO2UF$ and injection efficiency. Based on the analyses presented above, the optimal trade-off for this problem is with the case where $\eta = 0$. The norm weight $\eta > 0$ tends improve the volumetric sweep efficiency indirectly by accelerating production, this application shows that this might lead to inferior solutions in certain geologic scenarios.

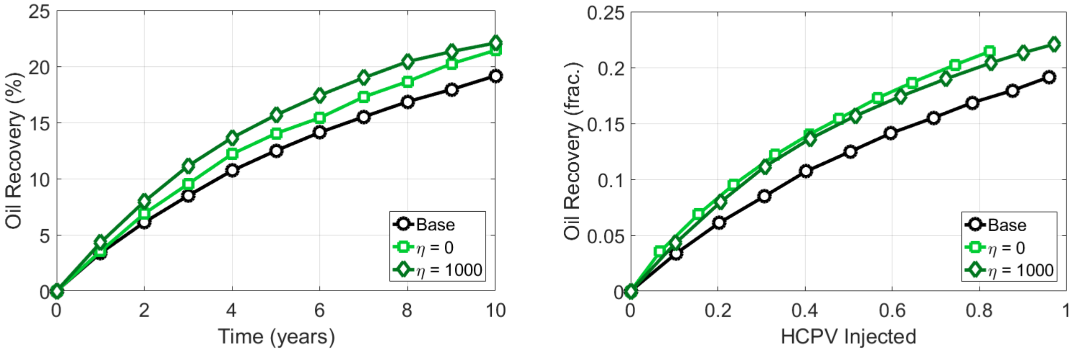

(a) (b)

Figure 4.17: Incremental Oil recovery efficiency as a function of (a) time in years and (b) reservoir pore volume injected in the Norne field case

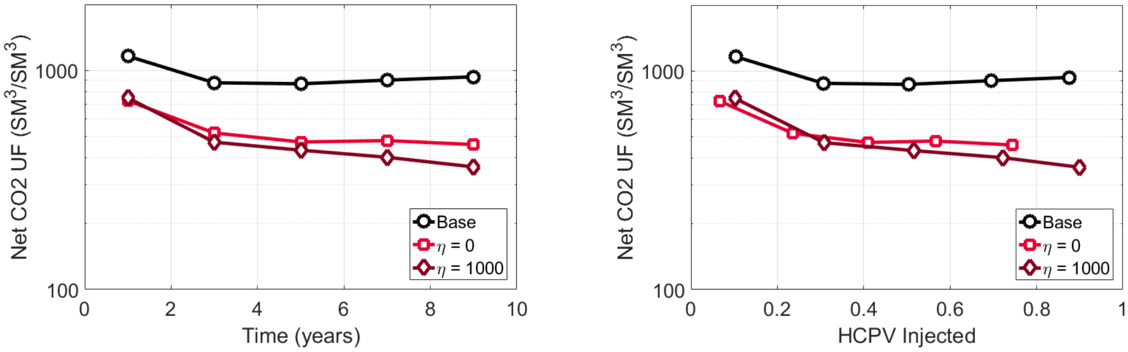

(a) (b)

Figure 4.18: Net CO2 utilization factor as a function of (a) time in years and (b) reservoir pore volume injected in the Norne field case

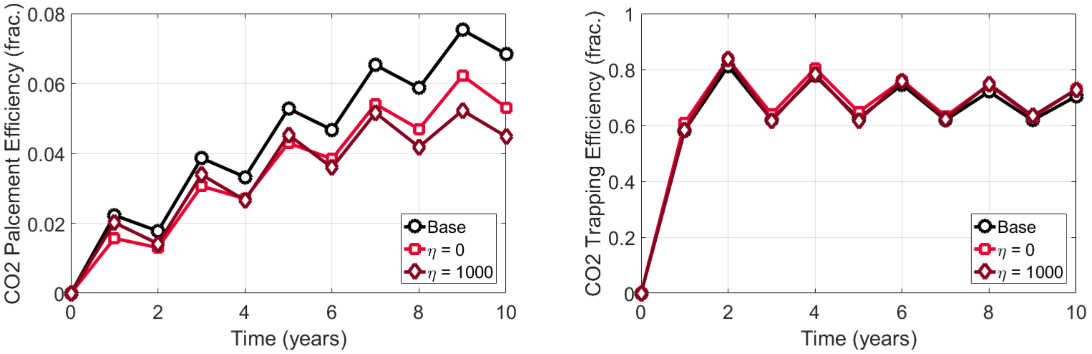

(a) (b)

Figure 4.19: (a) CO2 placement efficiency and (b) CO2 trapping efficiency as a function of time for Norne field case

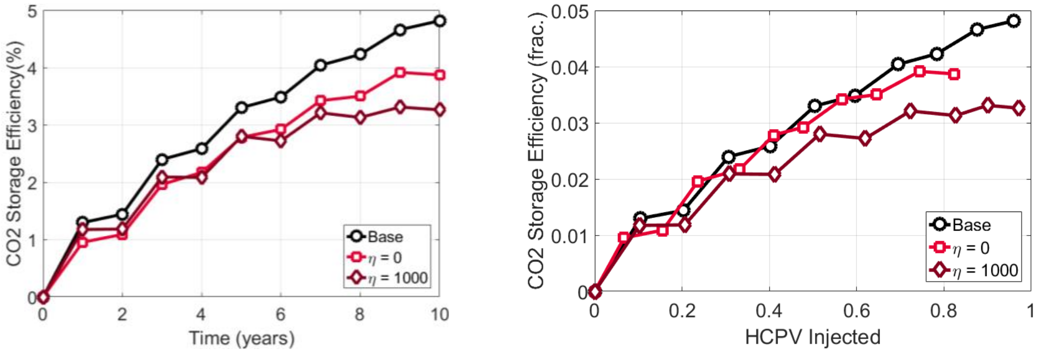

(a) (b)

Figure 4.20: CO2 storage efficiency as a function of (a) time in years and (b) reservoir pore volume injected in the Norne field case

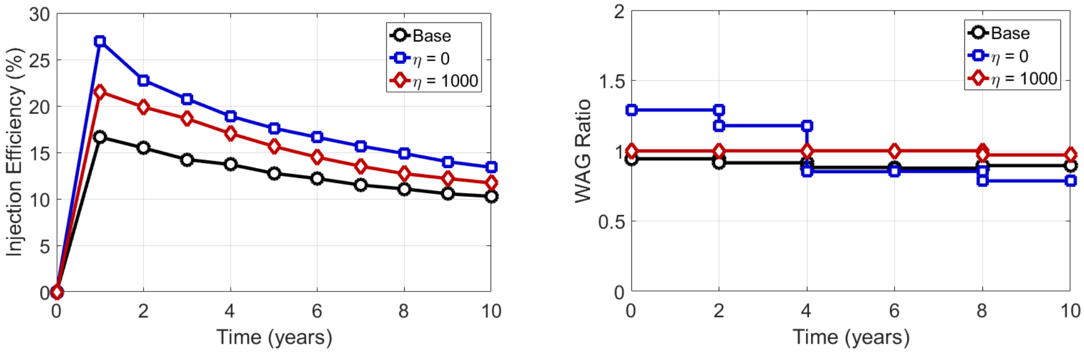

(a) (b)

Figure 4.21: (a) Injection efficiencies comparison (b) WAG ratios comparison in the Norne field case

## 4.6 Conclusion

In this work, we have proposed a streamline-based co-optimization method for CCUS applications with the aid of smart wells. The use of smart wells helps to mitigate the challenges associated with conformance in CO2 injection applications (Brnak et al., 2006). We specifically optimized CO2 WAG processes, considering the incremental oil recovery, CO2 storage and CO2 Utilization Factor as the decision variables, while individual ICV rates represent the design variables. Compared to other proposed methods of approaching the same problem, our approach provides robustness in terms of accounting gravity effects, as well as superior computational efficiency. This computational advantage comes from reduced number of full-scale simulations to arrive at optimal solutions, as required objective function gradient and hessian are computed in a single simulation run via our streamline-based technique. We presented an example with a 2D cross-section model to illustrate the algorithm, and then we applied to the Norne field to demonstrate the value and utility of the approach. The following conclusions can be reached:

(1) Using our streamline-based rate optimization approach in CO2 WAG schemes improves both incremental oil recovery, CO2 storage efficiency and CO2 Utilization Factor. This is achieved by obtaining optimal rate schedules that maximize both areal and vertical sweep efficiency during the process.

(2) Typically, higher values of the norm weight $\eta$ result in more optimal solutions in terms of the three decision variables. Injection efficiencies are however always optimal when only areal sweep efficiency maximization is the focus, that is $\eta = 0$. In such case, fluids are injected and produced at rates just enough to minimize the arrival time residuals at the producers.

(3) In certain scenarios based on the underlying geology, reservoir structure and/or well configuration, a potential trade-off might exist among the three decision variables, just as was observed with the Norne field application. In such scenarios, a careful choice of $\eta$ becomes crucial for a good optimal trade-off solution to the problem.

It is however, recommended that the choice of $\eta$ be dynamic through the optimization workflow using a multi-start feature. In such framework, multiple runs, each assigned varying values of $\eta$, are initiated at each time step and the best compromise solution is selected to mode to the next time step. This generalizes the entire optimization workflow to handle multiple scenarios in a more robust manner.

# CHAPTER V

# CONCLUSIONS AND RECOMMENDATIONS

It is expected that the world will continue to rely on hydrocarbons for its energy needs for the foreseeable future. However, the impact of fossil fuel combustion of the environment sue to CO2 emissions is believed not to be in the best interest of the planet's future. The Carbon Capture, Utilization and Storage (CCUS) technology has been accepted as a promising approach to unifying the two objectives. A common form of CCUS is the injection of anthropogenic CO2 in geologic formations for Enhanced Oil Recovery (CO2 EOR) in the process of which CO2 is permanently stored in the subsurface.

Like subsurface flow problems, CCUS in geological media requires a good understanding of the subsurface so as to effectively manage system pressure and the migration of the CO2 in a view to achieving both objectives of responsible energy production and successful containment of CO2 in the subsurface. A structured approach to effective reservoir management requires the following:

(1) Proper representation of the underlying physics that effectively captures the complex interactions between reservoir fluids and geologic properties. This representation, often in a mathematical framework refers to the forward model.

(2) A methodology for integrating data into an existing geologic model, in a view to improving the level of understanding of the subsurface. This step, often referred to as model calibration should be able to integrate multiple sources of data including

production and seismic data to update a prior subsurface model in a robust manner, while honoring relevant physics.

(3) A field development optimization procedure, which relies on the improved understanding of the subsurface to search for optimal set of configurations that improves overall performance of the process as it pertains to the essential CCUS objectives.

This dissertation features three contributions is each of the aspect outline above. In this chapter, we discuss the conclusions reached and provide recommendations for future research directions.

## 5.1 Conclusions

A streamline-based simulation of CO2 sequestration in saline aquifer has been proposed. Based on the results obtained, the following conclusions are drawn:

(1) The simulation methodology was benchmarked with a commercial compositional model with good agreement for both synthetic and field cases, at varying scales of permeability heterogeneity.

(2) Neglecting compressibility effects in streamline simulation of CO2 in saline aquifers under-estimates CO2 storage capacity by 15%. This number was arrived at based on both synthetic and field models.

(3) Ignoring formation dry-out effects in streamline simulation of CO2 in saline aquifers over-estimates CO2 infectivity. The effect, which is in agreement with previous studies, tend to be more severe with highly water-wet systems.

(4) Streamline-based simulation method provides an effective framework for resolving geologic heterogeneities during the injection of CO2 in saline aquifers.

The multiresolution grid connectivity-based (M-GCT) was presented in which high resolution reservoir description is retain with a specified area of interest (AOI). The set of conclusions drawn from the parameterization scheme for model calibration are as follows:

(1) The M-GCT scheme provides higher compression power within the AOI and less compression performance outside the AOI compared to the normal GCT scheme.
(2) Compression performance with the AOI improves (and deteriorates outside the AOI) with more aggressive coarsening schemes.
(3) Subsurface model calibration problems can be accelerated using the M-GCT parameterization schemes.

Finally, a streamline-based methodology for optimizing intelligent wells in CCUS application was presented. Decision variables such as incremental oil recovery efficiency, CO2 storage efficiency and CO2 utilization factor were considered. The following are the conclusions from this work:

(1) Using our streamline-based rate optimization approach in CO2 WAG schemes improves both incremental oil recovery, CO2 storage efficiency and CO2 Utilization Factor.
(2) Typically, higher values of the norm weight $\eta$ result in more optimal solutions in terms of the three decision variables.

## 5.2 Recommendations

For future contributions for the streamline-based simulation methodology are as follows:

(1) Application of the simulation methodology to high contrast systems and naturally fractured reservoirs.

(2) An investigation of the approach using vertical equilibration (VE) models (Gasda et al., 2009). This simplification, which relies on large aspect ratios of typical saline aquifers, reduces the need for gravity corrections during streamline simulation.

For grid connectivity-based parameterization in general, conditioning parameter update to available hard data at well or completion locations still remain unresolved. A possible solution is proposed in which a constrained eigenvalue problem is solved in the generation of the basis functions (Gander et al., 1989; Porcelli et al., 2015).

For a reservoir model with $N$ grid cells and $N_w < N$ hard data locations, a constrained eigenvalue problem can be expressed as follows:

$$\tilde{\mathbf{L}}\tilde{\mathbf{u}} = \lambda \mathbf{B}\tilde{\mathbf{u}} \tag{5.1}$$

Where $\lambda$ is the eigenvector while $\tilde{\mathbf{L}}$ an augmented Laplacian given as:

$$\tilde{\mathbf{L}} = \begin{pmatrix} \mathbf{L} & \mathbf{C} \\ \mathbf{C}^T & \mathbf{0} \end{pmatrix}; \text{ and } \mathbf{B} = \begin{pmatrix} \mathbf{I} & \mathbf{0} \\ \mathbf{0} & \mathbf{0} \end{pmatrix} \tag{5.2}$$

Note that $\mathbf{L}$ is the regular Laplacian. $\mathbf{C} = \left[ C_{ij} \right] \in \{0,1\}^{N \times N_w}$ is the constraint matrix which is computed as follows:

$$C_{ij} = \begin{cases} 1 & i = well_j \\ 0 & i \neq well_j \end{cases} \tag{5.3}$$

Where $well_j$ refers to the grid index of location of the $j^{th}$ well or completion. And finally, the augmented eigenvector, obtained by the singular value decomposition of $\tilde{\mathbf{L}}$ becomes:

$$\tilde{\mathbf{u}} = \begin{pmatrix} \mathbf{u} \\ \mathbf{0} \end{pmatrix} \tag{5.4}$$

The eigenvectors (basis functions) obtained from the regular and conditioned GCT schemes are compared in **Figs. 5.1** and **5.2**. Note that for both schemes the basis functions are orthogonal, however the all basis functions are constrained to zero values at each well or completion in the conditioned GCT scheme. Proposed parameter update using the conditioned GCT basis functions is as follows:

$$\mathbf{k} = \mathbf{k}_{prior} \exp(\Phi \mathbf{v}) \tag{5.5}$$

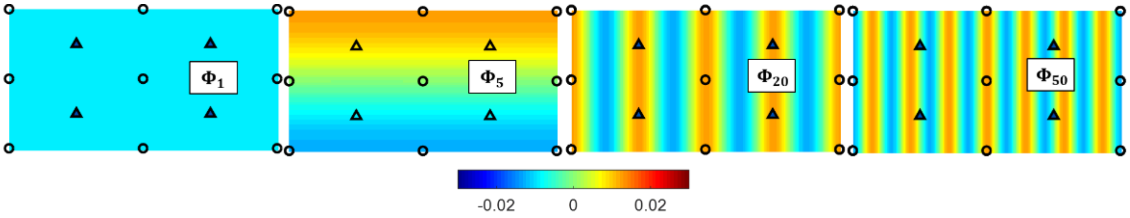

Figure 5.1: Unconstrained eigenvalue problem – Regular GCT basis functions

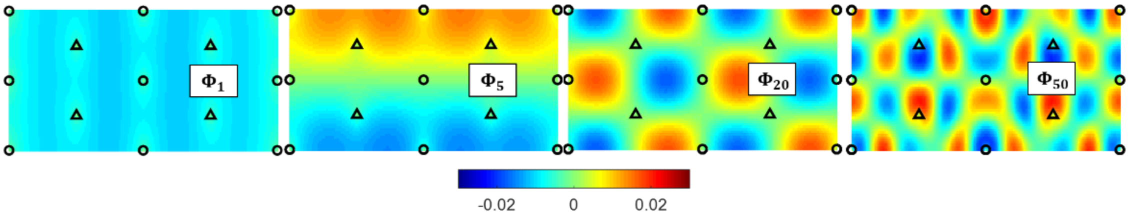

Figure 5.2: Constrained eigenvalue problem – Conditioned GCT basis functions

Finally, for the streamline-based optimization methodology proposed, the following research directions are recommended:

(1) A multi-start approach whereby multiple instances of the algorithm are run in parallel but with different values of $\eta$. At each time step best solution among the runs is retained. Keeping $\eta$ dynamic enhances the robustness of the optimization procedure.

(2) A multiobjective optimization framework for the streamline-based method, by which multiple trade-off solutions can be obtained in situations where certain decision objectives conflict.

# REFERENCES

Aanonsen, S.I., Nævdal, G., Oliver, D.S. et al. 2009. The ensemble Kalman filter in reservoir engineering--a review. *Spe Journal* **14** (03): 393-412.

Aarnes, J.E., Kippe, V., and Lie, K.-A. 2005. Mixed multiscale finite elements and streamline methods for reservoir simulation of large geomodels. *Advances in Water Resources* **28** (3): 257-271.

Albertoni, A. and Lake, L.W. 2003. Inferring interwell connectivity only from well-rate fluctuations in waterfloods. *SPE Reservoir Evaluation & Engineering* **6** (01): 6-16.

Alhuthali, A., Oyerinde, A., and Datta-Gupta, A. 2006. Optimal waterflood management using rate control. In *Proc.*, SPE Annual Technical Conference and Exhibition Society of Petroleum Engineers.

Alhuthali, A.H., Datta-Gupta, A., Yuen, B. et al. 2010. Optimizing smart well controls under geologic uncertainty. *Journal of Petroleum Science and Engineering* **73** (1): 107-121.

Alhuthali, A.H.H. 2009. *Optimal waterflood management under geologic uncertainty using rate control: Theory and field applications*. Texas A&M University.

Ampomah, W., Balch, R.S., Grigg, R.B. et al. 2017. Co-optimization of CO2-EOR and storage processes in mature oil reservoirs. *Greenhouse Gases: Science and Technology* **7** (1): 128-142.

Apps, J., Zheng, L., Zhang, Y. et al. 2010. Evaluation of potential changes in groundwater quality in response to CO2 leakage from deep geologic storage. *Transport in porous media* **82** (1): 215-246.

Arps, J.J. 1945. Analysis of decline curves. *Transactions of the AIME* **160** (01): 228-247.

Arts, R., Chadwick, A., Eiken, O. et al. 2008. Ten years' experience of monitoring CO2 injection in the Utsira Sand at Sleipner, offshore Norway. *First break* **26** (1).

Aziz, K. and Settari, A. 1979a. Petroleum reservoir simulation. *Applied Science Publ. Ltd., London, UK*.

Aziz, K. and Settari, A. 1979b. Petroleum reservoir simulation. *Applied Science Publ. Ltd., London, UK*.

Azzolina, N.A., Nakles, D.V., Gorecki, C.D. et al. 2015. CO 2 storage associated with CO 2 enhanced oil recovery: a statistical analysis of historical operations. *International Journal of Greenhouse Gas Control* **37**: 384-397.

Bachu, S., Bonijoly, D., Bradshaw, J. et al. 2007. CO 2 storage capacity estimation: methodology and gaps. *international journal of Greenhouse Gas Control* **1** (4): 430-443.

Bachu, S., Gunter, W., and Perkins, E. 1994. Aquifer disposal of CO 2: hydrodynamic and mineral trapping. *Energy Conversion and Management* **35** (4): 269-279.

Badru, O. and Kabir, C. 2003. Well placement optimization in field development. In *Proc.,* SPE Annual Technical Conference and Exhibition Society of Petroleum Engineers.

Batycky, R.P. 1997. A three-dimensional two-phase field scale streamline simulator, Stanford university Stanford, CA 94305.

Berenblyum, R.A., Shapiro, A.A., Jessen, K. et al. 2003. Black oil streamline simulator with capillary effects. In *Proc.,* SPE Annual Technical Conference and Exhibition Society of Petroleum Engineers.

Bhark, E., Jafarpour, B., and Datta-Gupta, A. 2011a. A generalized grid connectivity–based parameterization for subsurface flow model calibration. *Water Resources Research* **47** (6).

Bhark, E.W. 2011. Multiscale Spectral-Domain Parameterization for History Matching in Structured and Unstructured Grid Geometries, Texas A&M University.

Bhark, E.W., Jafarpour, B., and Datta-Gupta, A. 2011b. A generalized grid connectivity–based parameterization for subsurface flow model calibration. *Water Resources Research* **47** (6).

Blunt, M., Fayers, F.J., and Orr, F.M. 1993. Carbon dioxide in enhanced oil recovery. *Energy Conversion and Management* **34** (9): 1197-1204.

Bouzarkouna, Z., Ding, D.Y., and Auger, A. 2012. Well placement optimization with the covariance matrix adaptation evolution strategy and meta-models. *Computational Geosciences* **16** (1): 75-92.

Bratvedt, F., Gimse, T., and Tegnander, C. 1996. Streamline computations for porous media flow including gravity. *Transport in Porous Media* **25** (1): 63-78.

Brnak, J.J., Petrich, B., and Konopczynski, M.R. 2006. Application of SmartWell technology to the SACROC CO2 EOR project: A case study. In *Proc.*, SPE/DOE Symposium on Improved Oil Recovery  Society of Petroleum Engineers.

Chaban Habib, F.R. 2005. A numerical sensitivity analysis of streamline simulation, Texas A&M University.

Chen, B. and Reynolds, A.C. 2015. Ensemble-Based Optimization of the WAG Injection Process. In *Proc.*, SPE Reservoir Simulation Symposium  Society of Petroleum Engineers.

Chen, B. and Reynolds, A.C. 2017. Optimal control of ICV's and well operating conditions for the water-alternating-gas injection process. *Journal of Petroleum Science and Engineering* **149**: 623-640.

Chen, Y., Oliver, D.S., and Zhang, D. 2009. Efficient ensemble-based closed-loop production optimization. *SPE Journal* **14** (04): 634-645.

Cheng, H., Datta-Gupta, A., and He, Z. 2005. A comparison of travel-time and amplitude matching for field-scale production-data integration: Sensitivity, nonlinearity, and practical implications. *SPE Journal* **10** (01): 75-90.

Cheng, H., Osako, I., Datta-Gupta, A. et al. 2006. A Rigorous Compressible Streamline Formulation for Two and Three-Phase Black-Oil Simulation. *SPE Journal* **11** (04): 407-417.

Cheng, H., Oyerinde, A.S., Datta-Gupta, A. et al. 2007. Compressible streamlines and three-phase history matching. *SPE Journal* **12** (04): 475-485.

Cheng, H., Wen, X.-H., Milliken, W.J. et al. 2004. Field experiences with assisted and automatic history matching using streamline models. In *Proc.,* SPE Annual Technical Conference and Exhibition Society of Petroleum Engineers.

Christie, M. and Blunt, M. 2001. Tenth SPE comparative solution project: A comparison of upscaling techniques. In *Proc.,* SPE Reservoir Simulation Symposium Society of Petroleum Engineers.

Crameik, T. and Plassey, J. 1972. Carbon Dioxide Injection Project SACROC Unit, Scurry County, Texas. In *Proc.,* Annual Meeting Papers, Division of Production American Petroleum Institute.

Das, I. and Dennis, J.E. 1997. A closer look at drawbacks of minimizing weighted sums of objectives for Pareto set generation in multicriteria optimization problems. *Structural optimization* **14** (1): 63-69.

Datta-Gupta, A. and King, M.J. 2007. *Streamline simulation: theory and practice*. Society of Petroleum Engineers.

Davidson, J.E. and Beckner, B.L. 2003. Integrated optimization for rate allocation in reservoir simulation. In *Proc.,* SPE Reservoir Simulation Symposium Society of Petroleum Engineers.

De Natale, F.G., Desoli, G.S., Giusto, D.D. et al. 1992. Adaptive DCT for image-data compression. *European Transactions on Telecommunications* **3** (4): 359-366.

Deb, K., Pratap, A., Agarwal, S. et al. 2002. A fast and elitist multiobjective genetic algorithm: NSGA-II. *Evolutionary Computation, IEEE Transactions on* **6** (2): 182-197.

Deutsch, C.V. and Journel, A.G. 1992. Geostatistical software library and user's guide. *New York* **119**: 147.

Di Donato, G. and Blunt, M.J. 2004. Streamline-based dual-porosity simulation of reactive transport and flow in fractured reservoirs. *Water Resources Research* **40** (4).

DiPietro, P. 2013. Next generation CO2 enhanced oil recovery. In *Proc.*, Carbon Dioxide Utilization Congress, San Diego, California

Dittman, G.L. 1977. *Calculation of brine properties*. Lawrence Livermore Laboratory.

Duijndam, A.J.W. 1987. Detailed Bayesian inversion of seismic data. PhD Thesis PhD Thesis, Delft University of Technology.

EIA. 2014. Annual energy outlook 2014 with projections to 2040. *US Energy Information Administration, Washington, DC*.

Eigestad, G.T., Dahle, H.K., Hellevang, B. et al. 2009. Geological modeling and simulation of CO2 injection in the Johansen formation. *Computational Geosciences* **13** (4): 435-450.

Ekkawong, P., Han, J., Olalotiti-Lawal, F. et al. 2017. Multiobjective design and optimization of polymer flood performance. *Journal of Petroleum Science and Engineering* **153**: 47-58.

Emerick, A.A. and Reynolds, A.C. 2013. Ensemble smoother with multiple data assimilation. *Computers & Geosciences* **55**: 3-15.

Emerick, A.A., Silva, E., Messer, B. et al. 2009. Well placement optimization using a genetic algorithm with nonlinear constraints. In *Proc.*, SPE reservoir simulation symposium Society of Petroleum Engineers.

Ennis-King, J. and Paterson, L. 2003. Role of convective mixing in the long-term storage of carbon dioxide in deep saline formations. In *Proc.*, SPE annual technical conference and exhibition Society of Petroleum Engineers.

Ertekin, T., Abou-Kassen, J.H., and King, G.R. 2001. *Basic Applied Reservoir Simulations*. Society of Petroleum Engineers.

Ettehadtavakkol, A., Lake, L.W., and Bryant, S.L. 2014. CO 2-EOR and storage design optimization. *International Journal of Greenhouse Gas Control* **25**: 79-92.

Evensen, G. 2003. The ensemble Kalman filter: Theoretical formulation and practical implementation. *Ocean dynamics* **53** (4): 343-367.

Fenghour, A., Wakeham, W.A., and Vesovic, V. 1998. The viscosity of carbon dioxide. *Journal of Physical and Chemical Reference Data* **27** (1): 31-44.

Gander, W., Golub, G.H., and von Matt, U. 1989. A constrained eigenvalue problem. *Linear Algebra and its applications* **114**: 815-839.

Garcia, J.E. 2001. Density of aqueous solutions of CO2. *Lawrence Berkeley National Laboratory*.

Gasda, S.E., Nordbotten, J.M., and Celia, M.A. 2009. Vertical equilibrium with sub-scale analytical methods for geological CO2 sequestration. *Computational Geosciences* **13** (4): 469-481.

Gautier, Y., Blunt, M.J., and Christie, M.A. 1999. Nested gridding and streamline-based simulation for fast reservoir performance prediction. *Computational Geosciences* **3** (3-4): 295-320.

Ghaderi, S.M., Clarkson, C.R., and Chen, Y. 2012. Optimization of WAG process for coupled CO2 EOR-storage in tight oil formations: an experimental Design approach. In *Proc.,* SPE Canadian Unconventional Resources Conference Society of Petroleum Engineers.

Giorgis, T., Carpita, M., and Battistelli, A. 2007. 2D modeling of salt precipitation during the injection of dry CO 2 in a depleted gas reservoir. *Energy Conversion and Management* **48** (6): 1816-1826.

Global CCS Institute. 2017. The Global Status of CCS 2017: summary report. In *Global CCS Institute. See https://www.globalccsinstitute.com*

Gozalpour, F., Ren, S., and Tohidi, B. 2005. CO2 EOR and storage in oil reservoir. *Oil & gas science and technology* **60** (3): 537-546.

Griggs, D., Stafford-Smith, M., Gaffney, O. et al. 2013. Policy: Sustainable development goals for people and planet. *Nature* **495** (7441): 305-307.

Guyaguler, B. and Horne, R.N. 2001. Uncertainty assessment of well placement optimization. In *Proc.,* SPE annual technical conference and exhibition Society of Petroleum Engineers.

Hajizadeh, Y., Christie, M.A., and Demyanov, V. 2011. Towards multiobjective history matching: faster convergence and uncertainty quantification. In *Proc.,* SPE Reservoir Simulation Symposium Society of Petroleum Engineers.

Han, L. and Gu, Y. 2014. Optimization of miscible CO2 water-alternating-gas injection in the Bakken formation. *Energy & Fuels* **28** (11): 6811-6819.

Havlena, D. and Odeh, A. 1963. The material balance as an equation of a straight line. *Journal of Petroleum Technology* **15** (08): 896-900.

He, Z., Datta-Gupta, A., and Yoon, S. 2002. Streamline-Based Production Data Integration with Gravity and Changing Field Conditions. SPEJ 7 (4): 423-436. SPE-81208-PA.

Heidug, W. 2013. Methods to assess geologic CO 2 storage capacity: Status and best practice. In *Proc.,*

Hesse, M., Orr, F., and Tchelepi, H. 2008. Gravity currents with residual trapping. *Journal of Fluid Mechanics* **611** (1): 35-60.

Hidalgo, J.J. and Carrera, J. 2009. Effect of dispersion on the onset of convection during CO2 sequestration. *Journal of Fluid Mechanics* **640**: 441-452.

Honorio, J., Chen, C., Gao, G. et al. 2015. Integration of PCA with a novel machine learning method for reparameterization and assisted history matching geologically complex reservoirs. In *Proc.,* SPE Annual Technical Conference and Exhibition Society of Petroleum Engineers.

Hovorka, S. and Tinker, S. 2010. EOR as sequestration: Geoscience perspective. In *Proc.,* Symposium on the role of EOR in accelerating the deployment of CCS, an MIT Energy Initiative and Bureau of Economic Geology at UT Austin Symposium

Ibrahima, F., Maqui, A., Negreira, A.S. et al. 2017. Reduced-Physics Modeling and Optimization of Mature Waterfloods. In *Proc.,* SPE Abu Dhabi International Petroleum Exhibition & Conference Society of Petroleum Engineers.

IPCC. 2005. IPCC special report on carbon dioxide capture and storage. Prepared by Working Group III of the Intergovernmental Panel on Climate Change. IPCC, Cambridge University Press: Cambridge, United Kingdom and New York, USA.

IPCC. 2013. IPCC, 2013: climate change 2013: the physical science basis. Contribution of working group I to the fifth assessment report of the intergovernmental panel on climate change. Cambridge University Press.

IPCC. 2014. *Climate change 2014: synthesis report. Contribution of Working Groups I, II and III to the fifth assessment report of the Intergovernmental Panel on Climate Change*. eds. Pachauri, R.K.Allen, M.R.Barros, V.R.et al. IPCC.

Isebor, O.J., Echeverría Ciaurri, D., and Durlofsky, L.J. 2014. Generalized field-development optimization with derivative-free procedures. *SPE Journal* **19** (05): 891-908.

Jafarpour, B. and McLaughlin, D.B. 2008. History matching with an ensemble Kalman filter and discrete cosine parameterization. *Computational Geosciences* **12** (2): 227-244.

Jafarpour, B. and McLaughlin, D.B. 2009. Reservoir characterization with the discrete cosine transform. *SPE Journal* **14** (01): 182-201.

Jansen, J.-D., Brouwer, R., and Douma, S.G. 2009. Closed loop reservoir management. In *Proc.,* SPE Reservoir Simulation Symposium Society of Petroleum Engineers.

Jenny, P., Lee, S., and Tchelepi, H. 2003. Multi-scale finite-volume method for elliptic problems in subsurface flow simulation. *Journal of Computational Physics* **187** (1): 47-67.

Jimenez, E., Datta-Gupta, A., and King, M.J. 2010. Full-field streamline tracing in complex faulted systems with non-neighbor connections. *SPE Journal* **15** (01): 7-17.

Journel, A.G. and Alabert, F.G. 1990. New method for reservoir mapping. *Journal of Petroleum technology* **42** (02): 212-218.

Juanes, R., MacMinn, C.W., and Szulczewski, M.L. 2010. The footprint of the CO 2 plume during carbon dioxide storage in saline aquifers: storage efficiency for capillary trapping at the basin scale. *Transport in porous media* **82** (1): 19-30.

Karhunen, K. 1947. *Über lineare Methoden in der Wahrscheinlichkeitsrechnung*. Universitat Helsinki.

Karimi-Fard, M., Durlofsky, L.J., and Aziz, K. 2003. An efficient discrete fracture model applicable for general purpose reservoir simulators. In *Proc.,* SPE Reservoir Simulation Symposium Society of Petroleum Engineers.

Kestin, J., Khalifa, H.E., and Correia, R.J. 1981. Tables of the dynamic and kinematic viscosity of aqueous KCl solutions in the temperature range 25–150 C and the pressure range 0.1–35 MPa. *Journal of Physical and Chemical Reference Data* **10** (1): 57-70.

Khaninezhad, M.M., Jafarpour, B., and Li, L. 2012. Sparse geologic dictionaries for subsurface flow model calibration: Part I. Inversion formulation. *Advances in Water Resources* **39**: 106-121.

King, M. and Dunayevsky, V. 1989. Why waterflood works: a linearized stability analysis. In *Proc.,* SPE Annual Technical Conference and Exhibition Society of Petroleum Engineers.

King, M.J., Osako, I., and Datta-Gupta, A. 2005. A predictor–corrector formulation for rigorous streamline simulation. *International journal for numerical methods in fluids* **47** (8-9): 739-758.

Kleinitz, W., Dietzsch, G., and Köhler, M. 2003. Halite scale formation in gas-producing wells. *Chemical Engineering Research and Design* **81** (3): 352-358.

Kokal, S., Sanni, M., and Alhashboul, A. 2016. Design and Implementation of the First CO2-EOR Demonstration Project in Saudi Arabia. In *Proc.,* SPE Annual Technical Conference and Exhibition Society of Petroleum Engineers.

Kovscek, A. 2002. Screening criteria for CO2 storage in oil reservoirs. *Petroleum Science and Technology* **20** (7-8): 841-866.

Krevor, S., Blunt, M.J., Benson, S.M. et al. 2015. Capillary trapping for geologic carbon dioxide storage–From pore scale physics to field scale implications. *International Journal of Greenhouse Gas Control* **40**: 221-237.

Krevor, S., Pini, R., Zuo, L. et al. 2012. Relative permeability and trapping of CO2 and water in sandstone rocks at reservoir conditions. *Water Resources Research* **48** (2).

Kulkarni, K.N., Datta-Gupta, A., and Vasco, D.W. 2000. A streamline approach for integrating transient pressure data into high resolution reservoir models. In *Proc.,* SPE European Petroleum Conference Society of Petroleum Engineers.

Kumar, A., Noh, M.H., Ozah, R.C. et al. 2005. Reservoir simulation of CO 2 storage in aquifers. *SPE journal* **10** (03): 336-348.

Lake, L.W. 1989. *Enhanced oil recovery*. Prentice Hall.

Land, C.S. 1968. Calculation of imbibition relative permeability for two-and three-phase flow from rock properties. *Society of Petroleum Engineers Journal* **8** (02): 149-156.

Leach, A., Mason, C.F., and van‘t Veld, K. 2011. Co-optimization of enhanced oil recovery and carbon sequestration. *Resource and Energy Economics* **33** (4): 893-912.

Lehoucq, R.B., Sorensen, D.C., and Yang, C. 1998. *ARPACK users' guide: solution of large-scale eigenvalue problems with implicitly restarted Arnoldi methods*. SIAM.

Li, R., Reynolds, A.C., and Oliver, D.S. 2001. History matching of three-phase flow production data. In *Proc.,* SPE Reservoir Simulation Symposium Society of Petroleum Engineers.

Lie, K.-A. and Juanes, R. 2005. A front-tracking method for the simulation of three-phase flow in porous media. *Computational Geosciences* **9** (1): 29-59.

Loeve, M. 1978. Probability theory.

Lophaven, S.N., Nielsen, H.B., Søndergaard, J. et al. 2002. *DACE: a Matlab kriging toolbox, version 2.0*. IMM, Informatics and Mathematical Modelling, The Technical University of Denmark.

Ma, X., Al-Harbi, M., Datta-Gupta, A. et al. 2008. An efficient two-stage sampling method for uncertainty quantification in history matching geological models. *SPE Journal* **13** (01): 77-87.

MacMinn, C.W., Szulczewski, M.L., and Juanes, R. 2010. CO 2 migration in saline aquifers. Part 1. Capillary trapping under slope and groundwater flow. *Journal of Fluid Mechanics* **662**: 329-351.

Mathias, S.A., Hardisty, P.E., Trudell, M.R. et al. 2009a. Approximate solutions for pressure buildup during CO2 injection in brine aquifers. *Transport in porous media* **79** (2): 265-284.

Mathias, S.A., Hardisty, P.E., Trudell, M.R. et al. 2009b. Screening and selection of sites for CO 2 sequestration based on pressure buildup. *international journal of Greenhouse Gas Control* **3** (5): 577-585.

Mathworks. MATLAB Product Documentation. https://www.mathworks.com/help/.

Matringe, S. and Gerritsen, M. 2004. On accurate tracing of streamlines. In *Proc.,* SPE Annual Technical Conference and Exhibition Society of Petroleum Engineers.

Maucec, M., Douma, S.G., Hohl, D. et al. 2007. Streamline-Based History Matching and Uncertainty--Markov-Chain Monte Carlo Study of an Offshore Turbidite Oil Field. In *Proc.,* SPE Annual Technical Conference and Exhibition Society of Petroleum Engineers.

Melzer, L.S. 2006. Stranded Oil in the Residual Oil Zone. *Melzer Consulting prepared for Advanced Resources International and the US Department of Energy: Office of Fossil Energy0 Office of Oil and Natural Gas*.

Melzer, L.S. 2012. Carbon dioxide enhanced oil recovery (CO2 EOR): Factors involved in adding carbon capture, utilization and storage (CCUS) to enhanced oil recovery. *Center for Climate and Energy Solutions*.

Mijic, A., LaForce, T.C., and Muggeridge, A.H. 2014. CO2 injectivity in saline aquifers: The impact of non-Darcy flow, phase miscibility, and gas compressibility. *Water Resources Research* **50** (5): 4163-4185.

Mohamed, L., Christie, M.A., Demyanov, V. et al. 2010. Application of particle swarms for history matching in the Brugge reservoir. In *Proc.*, SPE Annual Technical Conference and Exhibition  Society of Petroleum Engineers.

Morais, H.L. 2012. Application of WAG and SWAG injection Techniques in Norne E-Segment. *Norwegian University of Science and Technology*.

Møyner, O., Krogstad, S., and Lie, K.-A. 2015. The application of flow diagnostics for reservoir management. *SPE Journal* **20** (02): 306-323.

Møyner, O. and Lie, K.-A. 2014. The multiscale finite-volume method on stratigraphic grids. *SPE Journal* **19** (05): 816-831.

Neufeld, J.A., Hesse, M.A., Riaz, A. et al. 2010. Convective dissolution of carbon dioxide in saline aquifers. *Geophysical research letters* **37** (22).

Nghiem, L., Sammon, P., Grabenstetter, J. et al. 2004. Modeling CO2 storage in aquifers with a fully-coupled geochemical EOS compositional simulator. In *Proc.*, SPE/DOE symposium on improved oil recovery  Society of Petroleum Engineers.

Nilsen, H.M. and Lie, K.-A. 2009. Front Tracking Methods for Use in Streamline Simulation of Compressible Flow. In *Proc.*, SPE Reservoir Simulation Symposium  Society of Petroleum Engineers.

Nilsen, H.M., Lie, K.-A., Møyner, O. et al. 2015. Spill-point analysis and structural trapping capacity in saline aquifers using MRST-co2lab. *Computers & Geosciences* **75**: 33-43.

Nocedal, J. and Wright, S. 2006a. *Numerical optimization*. Springer Science & Business Media.

Nocedal, J. and Wright, S.J. 2006b. *Sequential quadratic programming*. Springer.

Nordbotten, J.M., Celia, M.A., and Bachu, S. 2005. Injection and storage of CO2 in deep saline aquifers: Analytical solution for CO2 plume evolution during injection. *Transport in porous media* **58** (3): 339-360.

Obi, E.O.I. and Blunt, M.J. 2006. Streamline-based simulation of carbon dioxide storage in a north sea aquifer. *Water Resources Research* **42** (3).

Olalotiti-Lawal, F. 2013. Application of Fast Marching Methods for Rapid Reservoir Forecast and Uncertainty Quantification. Masters Thesis, Texas A&M Univeristy.

Olalotiti-Lawal, F. and Datta-Gupta, A. 2015. A Multi-Objective Markov Chain Monte Carlo Approach for History Matching and Uncertainty Quantification. In *Proc.,* SPE Annual Technical Conference and Exhibition Society of Petroleum Engineers.

Olalotiti-Lawal, F., Onishi, T., Datta-Gupta, A. et al. 2017. Post-Combustion CO2 EOR Development in a Mature Oil Field: Model Calibration Using a Hierarchical Approach. In *Proc.,* SPE Annual Technical Conference and Exhibition Society of Petroleum Engineers.

Oliver, D.S. and Chen, Y. 2011. Recent progress on reservoir history matching: a review. *Computational Geosciences* **15** (1): 185-221.

Oliver, D.S., Reynolds, A.C., and Liu, N. 2008. *Inverse theory for petroleum reservoir characterization and history matching*. Cambridge University Press.

Onwunalu, J.E. and Durlofsky, L. 2011. A new well-pattern-optimization procedure for large-scale field development. *SPE Journal* **16** (03): 594-607.

Orr, F.M. 2007. *Theory of gas injection processes*. Tie-Line Publications.

Osako, I. and Datta-Gupta, A. 2007. A compositional streamline formulation with compressibility effects. In *Proc.,* SPE Reservoir Simulation Symposium Society of Petroleum Engineers.

Ott, H., Roels, S., and De Kloe, K. 2015. Salt precipitation due to supercritical gas injection: I. Capillary-driven flow in unimodal sandstone. *international journal of Greenhouse Gas Control* **43**: 247-255.

Pacala, S. and Socolow, R. 2004. Stabilization wedges: solving the climate problem for the next 50 years with current technologies. *science* **305** (5686): 968-972.

Paige, C.C. and Saunders, M.A. 1982. LSQR: An algorithm for sparse linear equations and sparse least squares. *ACM transactions on mathematical software* **8** (1): 43-71.

Park, H.-Y. and Datta-Gupta, A. 2013. Reservoir management using streamline-based flood efficiency maps and application to rate optimization. *Journal of Petroleum Science and Engineering* **109**: 312-326.

Park, H.-Y., Datta-Gupta, A., and King, M.J. 2015. Handling conflicting multiple objectives using Pareto-based evolutionary algorithm during history matching of reservoir performance. *Journal of Petroleum Science and Engineering* **125**: 48-66.

Parker, R.L. 1994. *Geophysical inverse theory*. Princeton university press.

Passone, S. and McRae, G.J. 2007. Probabilistic Field Development in Presence of Uncertainty. In *Proc.,* International Petroleum Technology Conference International Petroleum Technology Conference.

Pau, G.S., Bell, J.B., Pruess, K. et al. 2010. High-resolution simulation and characterization of density-driven flow in CO 2 storage in saline aquifers. *Advances in Water Resources* **33** (4): 443-455.

Peters, L., Arts, R., Brouwer, G. et al. 2010. Results of the Brugge benchmark study for flooding optimization and history matching. *SPE Reservoir Evaluation & Engineering* **13** (03): 391-405.

Peysson, Y., Andre, L., and Azaroual, M. 2014. Well injectivity during CO2 storage operations in deep saline aquifers—Part 1: Experimental investigation of drying effects, salt precipitation and capillary forces. *international journal of Greenhouse Gas Control* **22**: 291-300.

Pham, V. and Halland, E. 2017. Perspective of CO2 for Storage and Enhanced Oil Recovery (EOR) in Norwegian North Sea.

Pollock, D.W. 1988. Semianalytical computation of path lines for finite-difference models. *Ground water* **26** (6): 743-750.

Porcelli, M., Binante, V., Girardi, M. et al. 2015. A solution procedure for constrained eigenvalue problems and its application within the structural finite-element code NOSA-ITACA. *Calcolo* **52** (2): 167-186.

Potter, R., Babcock, R., and Brown, D. 1977. New method for determining the solubility of salts in aqueous solutions at elevated temperatures. *J. Res. US Geol. Surv.;(United States)* **5** (3).

Pruess, K. 2005. *ECO2N: A TOUGH2 fluid property module for mixtures of water, NaCl, and CO2*. Lawrence Berkeley National Laboratory Berkeley.

Pruess, K. and Müller, N. 2009. Formation dry-out from CO2 injection into saline aquifers: 1. Effects of solids precipitation and their mitigation. *Water Resources Research* **45** (3).

Qi, R., LaForce, T.C., and Blunt, M.J. 2009. A three-phase four-component streamline-based simulator to study carbon dioxide storage. *Computational Geosciences* **13** (4): 493-509.

Ramos, M.G. and Hemami, S.S. 1996. Edge-adaptive JPEG image compression. In *Proc.*, Visual Communications and Image Processing'96 International Society for Optics and Photonics. 1082-1093.

Redlich, O. and Kwong, J.N. 1949. On the thermodynamics of solutions. V. An equation of state. Fugacities of gaseous solutions. *Chemical reviews* **44** (1): 233-244.

Riaz, A., Hesse, M., Tchelepi, H. et al. 2006. Onset of convection in a gravitationally unstable diffusive boundary layer in porous media. *Journal of Fluid Mechanics* **548**: 87-111.

Rossen, W.R., Van Duijn, C., Nguyen, Q.P. et al. 2010. Injection strategies to overcome gravity segregation in simultaneous gas and water injection into homogeneous reservoirs. *SPE Journal* **15** (01): 76-90.

Rwechungura, R.W., Suwartadi, E., Dadashpour, M. et al. 2010. The norne field case-a unique comparative case study. In *Proc.*, SPE Intelligent Energy Conference and Exhibition Society of Petroleum Engineers.

Saadatpoor, E., Bryant, S.L., and Sepehrnoori, K. 2010. New trapping mechanism in carbon sequestration. *Transport in porous media* **82** (1): 3-17.

Samet, H. 1984. The quadtree and related hierarchical data structures. *ACM Computing Surveys (CSUR)* **16** (2): 187-260.

Sarma, P. and Chen, W.H. 2008. Efficient well placement optimization with gradient-based algorithms and adjoint models. In *Proc.,* Intelligent energy conference and exhibition Society of Petroleum Engineers.

Sarma, P., Durlofsky, L., and Aziz, K. 2008a. Computational techniques for closed–loop reservoir modeling with application to a realistic reservoir. *Petroleum Science and Technology* **26** (10-11): 1120-1140.

Sarma, P., Durlofsky, L.J., and Aziz, K. 2005. Efficient closed-loop production optimization under uncertainty (spe94241). In *Proc.,* 67th EAGE Conference & Exhibition

Sarma, P., Durlofsky, L.J., and Aziz, K. 2008b. Kernel principal component analysis for efficient, differentiable parameterization of multipoint geostatistics. *Mathematical Geosciences* **40** (1): 3-32.

Sayarpour, M., Zuluaga, E., Kabir, C.S. et al. 2009. The use of capacitance–resistance models for rapid estimation of waterflood performance and optimization. *Journal of Petroleum Science and Engineering* **69** (3): 227-238.

Schlumberger. 2014. *Technical Description*. ECLIPSE Industry-Reference Reservoir Simulator. Schlumberger.

Schulze-Riegert, R., Axmann, J., Haase, O. et al. 2002. Evolutionary algorithms applied to history matching of complex reservoirs. *SPE Reservoir Evaluation & Engineering* **5** (02): 163-173.

Seto, C. and Orr, F. 2009. Analytical solutions for multicomponent, two-phase flow in porous media with double contact discontinuities. *Transport in porous media* **78** (2): 161-183.

Seto, C.J., Jessen, K., and Orr, F.M. 2007. Using analytical solutions in compositional streamline simulation of a field-scale CO2-injection project in a condensate reservoir. *SPE Reservoir Evaluation & Engineering* **10** (04): 393-405.

Sharma, M., Taware, S., and Datta-Gupta, A. 2016. Optimizing CO2 Floods Using Rate Control with Smart Wells Under Geologic Uncertainty. In *Proc.*, Abu Dhabi International Petroleum Exhibition & Conference Society of Petroleum Engineers.

Sharma, M., Taware, S.V., and Datta-Gupta, A. 2011. Optimizing polymerflood via rate control. In *Proc.*, SPE Enhanced Oil Recovery Conference Society of Petroleum Engineers.

Siirila, E.R., Navarre-Sitchler, A.K., Maxwell, R.M. et al. 2012. A quantitative methodology to assess the risks to human health from CO 2 leakage into groundwater. *Advances in Water Resources* **36**: 146-164.

Song, Z., Li, Z., Wei, M. et al. 2014. Sensitivity analysis of water-alternating-CO 2 flooding for enhanced oil recovery in high water cut oil reservoirs. *Computers & Fluids* **99**: 93-103.

Span, R. and Wagner, W. 1996. A new equation of state for carbon dioxide covering the fluid region from the triple-point temperature to 1100 K at pressures up to 800 MPa. *Journal of Physical and Chemical Reference Data* **25** (6): 1509-1596.

Spiteri, E., Juanes, R., Blunt, M.J. et al. 2005. Relative-permeability hysteresis: trapping models and application to geological CO2 sequestration. In *Proc.*, SPE Annual Technical Conference and Exhibition Society of Petroleum Engineers.

Spycher, N. and Pruess, K. 2005. CO2-H2O mixtures in the geological sequestration of CO2. II. Partitioning in chloride brines at 12–100 C and up to 600 bar. *Geochimica et cosmochimica acta* **69** (13): 3309-3320.

Spycher, N., Pruess, K., and Ennis-King, J. 2003. CO2-H2O mixtures in the geological sequestration of CO2. I. Assessment and calculation of mutual solubilities from 12 to 100 C and up to 600 bar. *Geochimica et cosmochimica acta* **67** (16): 3015-3031.

Steffensen, I. and Karstadt, P.I. 1996. Norne field development-fast track from discovery to production. *Journal of Petroleum Technology* **48** (04): 296-339.

Stenerud, V.R., Kippe, V., Lie, K.-A. et al. 2008. Adaptive multiscale streamline simulation and inversion for high-resolution geomodels. *SPE Journal* **13** (01): 99-111.

Strang, G. 1999. The discrete cosine transform. *SIAM review* **41** (1): 135-147.

Sweby, P.K. 1984. High resolution schemes using flux limiters for hyperbolic conservation laws. *SIAM journal on numerical analysis* **21** (5): 995-1011.

Szulczewski, M., Hesse, M., and Juanes, R. 2013. Carbon dioxide dissolution in structural and stratigraphic traps. *Journal of Fluid Mechanics* **736**: 287-315.

Taber, J., Martin, F., and Seright, R. 1997a. EOR screening criteria revisited—part 2: applications and impact of oil prices. *SPE Reservoir Engineering* **12** (03): 199-206.

Taber, J.J., Martin, F., and Seright, R. 1997b. EOR screening criteria revisited-Part 1: Introduction to screening criteria and enhanced recovery field projects. *SPE Reservoir Engineering* **12** (03): 189-198.

Tanaka, S. 2014. Effective Reservoir Management Using Streamline-Based Reservoir Simulation, History Matching and Rate Allocation Optimization.

Tanaka, S., Datta-Gupta, A., and King, M.J. 2014. Compositional Streamline Simulation of CO2 Injection Accounting for Gravity and Capillary Effects Using Orthogonal Projection. In *Proc.*, SPE Improved Oil Recovery Symposium Society of Petroleum Engineers.

Tanaka, S., Kam, D., Xie, J. et al. 2017. A Generalized Derivative-Free Rate Allocation Optimization for Water and Gas Flooding Using Streamline-Based Method. In *Proc.*, SPE Annual Technical Conference and Exhibition Society of Petroleum Engineers.

Tarantola, A. 2005. Inverse problem theory. Methods for model parameter estimation, SIAM, Philadelphia. *Inverse problem theory and methods for model parameter estimation. SIAM, Philadelphia, PA.*

Taware, S., Sharma, M., and Datta-Gupta, A. 2010. Optimal water flood management under geological uncertainty using accelerated production strategy. *SPE* **133882**: 19-22.

Taware, S.V., Park, H.-y., Datta-Gupta, A. et al. 2012. Well placement optimization in a mature carbonate waterflood using streamline-based quality maps. In *Proc.*, SPE Oil and Gas India Conference and Exhibition Society of Petroleum Engineers.

Tchelepi, H. and Orr Jr, F. 1993. The interaction of viscous fingering, permeability heterogeneity and gravity segregation in 3D. In *Proc.*, SPE Symposium on Reservoir Simulation Society of Petroleum Engineers.

Thiele, M.R. and Batycky, R. 2003. Water injection optimization using a streamline-based workflow. In *Proc.*, SPE Annual Technical Conference and Exhibition Society of Petroleum Engineers.

Thiele, M.R. and Batycky, R.P. 2006. Using streamline-derived injection efficiencies for improved waterflood management. *SPE Reservoir Evaluation & Engineering* **9** (02): 187-196.

Todd, M. and Longstaff, W. 1972. The development, testing, and application of a numerical simulator for predicting miscible flood performance. *Journal of Petroleum Technology* **24** (07): 874-882.

Trefethen, L.N. and Bau III, D. 1997. *Numerical linear algebra*. Siam.

USDOE. Carbon Storage Atlas. https://www.netl.doe.gov/research/coal/carbon-storage/atlasv.

Van Genuchten, M.T. 1980. A closed-form equation for predicting the hydraulic conductivity of unsaturated soils. *Soil science society of America journal* **44** (5): 892-898.

Vasco, D., Seongsik, Y., and Datta-Gupta, A. 1999. Integrating Dynamic Data Into High-Resolution Reservoir Models Using Streamline-Based Analytic Sensitivity Coefficients. *SPE Journal* **4** (04): 389-399.

Verma, A. and Pruess, K. 1988. Thermohydrological conditions and silica redistribution near high-level nuclear wastes emplaced in saturated geological formations. *Journal of Geophysical Research: Solid Earth* **93** (B2): 1159-1173.

Vilarrasa, V., Bolster, D., Dentz, M. et al. 2010. Effects of CO2 compressibility on CO2 storage in deep saline aquifers. *Transport in porous media* **85** (2): 619-639.

Vilarrasa, V., Carrera, J., Bolster, D. et al. 2013. Semianalytical Solution for CO2 Plume Shape and Pressure Evolution During CO2 Injection in Deep Saline Formations. *Transport in porous media* **97** (1): 43-65.

Vitoonkijvanich, S., AlSofi, A.M., and Blunt, M.J. 2015. Design of foam-assisted carbon dioxide storage in a North Sea aquifer using streamline-based simulation. *International Journal of Greenhouse Gas Control* **33**: 113-121.

Wallace, M. and Kuuskraa, V. 2014. Near-Term Projections of CO2 Utilization for Enhanced Oil Recovery. National Energy Technology Laboratory.

Wallace, M., Kuuskraa, V.A., and DiPietro, J. 2013. An In-Depth Look at "Next Generation" CO2 EOR Technology. *Oral presentation given at the National Energy Technology Laboratory, Morgantown, West Virginia*.

Wang, C., Li, G., and Reynolds, A.C. 2009. Production optimization in closed-loop reservoir management. *SPE journal* **14** (03): 506-523.

Watanabe, S. and Datta-Gupta, A. 2012. Use of phase streamlines for covariance localization in ensemble Kalman filter for three-phase history matching. *SPE Reservoir Evaluation & Engineering* **15** (03): 273-289.

Watanabe, S., Han, J., Hetz, G. et al. 2017. Streamline-Based Time-Lapse-Seismic-Data Integration Incorporating Pressure and Saturation Effects. *SPE Journal*.

Willhite, G. 1986. Waterflooding, volume 3 of SPE Textbook Series. *Society of Petroleum Engineers, Richardson, TX*.

Wilson, M. and Monea, M. 2004. IEA GHG Weyburn CO2 monitoring & storage project. Summary report 2000-2004.

Xie, J., Efendiev, Y., and Datta-Gupta, A. 2011. Uncertainty quantification in history matching of channelized reservoirs using Markov chain level set approaches. In *Proc.*, SPE Reservoir Simulation Symposium Society of Petroleum Engineers.

Yanosik, J. and McCracken, T. 1979. A nine-point, finite-difference reservoir simulator for realistic prediction of adverse mobility ratio displacements. *Society of Petroleum Engineers Journal* **19** (04): 253-262.

Zandvliet, M., Handels, M., van Essen, G. et al. 2008. Adjoint-based well-placement optimization under production constraints. *SPE Journal* **13** (04): 392-399.

Zhou, D., Yan, M., and Calvin, W.M. 2012. Optimization of a mature CO2 flood-from continuous injection to WAG. In *Proc.*, SPE Improved Oil Recovery Symposium Society of Petroleum Engineers.